Hologram tomography for surface topometry

Inaugural - Dissertation

zur

Erlangung des Doktorgrades der

Mathematisch-Naturwissenschaftlichen Fakultät
der Heinrich-Heine-Universität Düsseldorf

vorgelegt von

Dominik M. Giel

aus Traben-Trarbach

Düsseldorf

2003

Gedruckt mit der Genehmigung der Mathematisch-Naturwissenschaftlichen Fakultät der Heinrich-Heine-Universität Düsseldorf

Referent:	Prof. P. Hering
Koreferent:	Prof. G. Pretzler
Tag der mündlichen Prüfung:	30.07.2003

Zusammenfassung

Die vorliegende Arbeit untersucht Methoden zur Erfassung der Form von Oberflächen mit Hilfe kurzgepulster Holographie unter besonderer Berücksichtigung der Anforderungen eines Einsatzes in der medizinische Anwendung. Zur holographischen Oberflächenformerfassung wird zunächst das Interferenzmuster eines von der zu untersuchenden Oberfläche gestreuten, gepulsten Lichtfeldes mit einer kohärenten Referenzwelle in einer hochauflösenden photographischen Emulsion aufgezeichnet. Dieses sogenannte Hologramm projiziert im zweiten Schritt das dreidimensionale Lichtfeld des Objektes an den Ort des reellen Bildes, dessen räumliche Intensitätsverteilung mit Hilfe eines Streuschirmes und einer Kamera digitalisiert wird (Hologramm-Tomographie). Im Gegensatz zur direkten Messung steht so das Lichtfeld des Objektes für beliebig lange Zeiträume zur Verfügung. Aus den digitalisierten Projektionen des rekonstruierten Feldes wird die Oberflächenform des Objektes bestimmt (Topometrie). Verschiedene Methoden zur Bestimmung der Oberflächenform wurden entwickelt und verglichen. Die experimentelle Überprüfung der einzelnen Methoden führten zu ersten Anwendungen des Verfahrens in der Medizin und der Archäologie.

In der Einführung (Kapitel 1) werden bisher eingesetzte Verfahren für die Ortsmessung im Bereich der Medizin vorgestellt, wo eine präzise, dreidimensionale Dokumentation im speziellen der Gesichtsoberfläche von Vorteil für die Planung komplexer Eingriffe ist und die Patientenbewegung eine schnelle und unschädliche Aufnahmetechnik wie die gepulste Holographie erfordert. In Kapitel 2 werden die grundlegenden Begriffe der Holographie eingeführt und das zentrale Konzept der Hologramm-Perspektive entwickelt. Zur Nutzung derselben wurden zwei Methoden eingesetzt: die Mehrperspektiven-Aufzeichung durch Planspiegel und die Generierung von Perspektive durch partielle Hologramm-Abdeckung. Letztere erlaubte die Oberflächenlokalisierung durch Vielperspektiven-Gradientenmitteln (engl. multi-perspective gradient averaging, MUPEGA), einer meines Wissens neuartigen Technik. Außerdem wurden zwei rein numerische Methoden aus dem Bereich der Mikroskopie erstmals auf Hologramme angewendet: Das inverse Filtern schwächt die Unschärfe unfokussierter Bildpunkte durch die numerische Umkehrung der Abbildung ab. Das iterative Entfalten erreicht den gleichen Zweck mittels mehrfacher Simulation des Abbildungsvorganges mit anschließender Korrektur des durch Vergleich mit den Messdaten ermittelten Fehlers. Da beide Methoden die Kenntnis der (inkohärenten) optischen Transferfunktion voraussetzen, wurde eine analytische Form derselben hergeleitet. Weiterhin wurde ein neuartiges, gewichtetes Schärfemaß entwickelt, das die bereits bekannte Methode der Oberflächenbestimmung durch das Auffinden der Punkte maximaler Bildschärfe verbessert. Kapitel 3 beschreibt die zur Aufzeichnung und Auswertung der Hologramme verwendeten Geräte, insbesondere die neuartigen Anordnungen zur strukturierten Objektbeleuchtung durch Laserspeckle-Projektion und einen Aufbau zur Mehrperspektiven-Aufzeichnung. Kapitel 4 fasst die Ergebnisse der Arbeit zusammen: Experimentell bestimmt wurde die maximale Geschwindigkeit, mit der sich Oberflächen während der Aufnahme bewegen dürfen (15.4 ± 0.4 m/s), die Punktabbildungsfunktion des holographischen Aufbaus und die minimale erreichbare Specklegröße auf menschlicher Haut (etwa 0.5 mm bei einem Kontrast von 0.5). Erstmals wurde die Intensitätsverteilung des reellen Bildes sowohl durch inverses Filtern als auch durch iterative Entfaltung auf oberflächennahe Punkte reduziert. Mehrere Objektansichten wurden synchron mit Hilfe eines Planspiegels aufgezeichet, was eine Rekonstruktion des Objektlichtfeldes in einem größeren Raumwinkel ermöglicht. Mit Hilfe der die MUPEGA-Auswertung wurde die Formerfassung mit der geringsten Abweichung von der tatsächlichen Oberfläche (Standardabweichung 0.89 ± 4 mm) aller vorgestellten Methoden erreicht. Ein mit für das geöffnete menschliche Auge unschädlicher Pulsenergie aufgezeichnetes Portraithologramm konnte mit der MUPEGA-Methode ausgewertet werden. Eine ersten Fallstudie, die holographische Dokumentation einer operativen Korrektur einer Unterkiefer-Fehlstellung, zeigt die aus dem Verfahren der Hologramm-Tomographie erwachsenden Möglichkeiten. Des weiteren wurden zur Demonstration der Mehrperspektiven-Spiegelaufzeichnung Ansichten eines 2000 Jahre alten archäologischen Fundes, der Husbäke Moorleiche, aufgenommen. Abschließend wird die Aufzeichnung eines Hologrammes auf ein digitales Medium vorgestellt, die eine virtuelle Hologramm-Tomographie mit einer Tiefenauflösung von ca. 8 mm ermöglichte. Diese Echtzeitfähigkeit der volldigitalen Holographie ist eine der Zukunftsperspektiven, die im abschließenden Kapitel 5 diskutiert werden. Ergänzend wird im Anhang A die Erzeugung von Computermodellen mit voller Farbinformation behandelt.

Abstract

Hologram tomography is a technique for precise, ultra-fast surface shape measurement (topometry) of extended objects. The scattered light from the surface is holographically recorded with a pulsed laser beam. A copy of the original light field, the holographic real image, can be recreated optically for infinite periods of time, allowing digitalisation without any temporal constraints. This thesis presents novel methods for surface shape measurement by hologram tomography, gives examples of their application in medicine and archeology and describes a holographic camera system and a real image digitalisation set-up.

Two purely numerical image deblurring techniques from microscopy were used in conjunction with holographic real images: inverse filtering and iterative deconvolution. Inverse filtering lowers the intensity from out-of-focus object points by numerical inversion of the imaging process. Iterative deconvolution simulates the imaging process and subsequently corrects an object estimate by comparison with the actual real image. Both methods require the knowledge of the optical transfer function for which an analytical expression was derived. Another semi-heuristic method for surface finding relies on the sharpness evaluation of the real image. To improve the surface localization, a novel, weighted figure-of-merit algorithm was derived and the improved precision of the surface localization was experimentally verified. Two methods which rely on the perspective information of holograms were developed: Mirror recording captures multiple perspective views of an object synchronously with a planar mirror. Multi-perspective gradient averaging (MUPEGA) uses partially illuminated planar holograms for surface shape measurements. Mirror recordings of objects can also be combined for alternating iterative deconvolution, an algorithm which combines deblurring methods from microscopy with simultaneous algebraic reconstruction (SART) from computer tomography. In an experimental comparison of the different methods for hologram tomography, the MUPEGA reconstruction of a test object achieved the lowest standard deviation between the reconstructed and the actual surface (0.89 ± 4 mm). To enhance the surface localization, a laser speckle projection set-up was build and characterized. The maximum achievable speckle size on human skin was determined experimentally to be approximately 0.5 mm at a contrast of 0.5. The temporal resolution of the pulsed hologram recording was estimated by measurements of the maximum tolerable velocity for object surface movements $v_{max} = 15.4 \pm 0.4$ m/s with a pulse duration of 35 ns.

The holographic camera system presented in this thesis was build for facial surface shape measurements in the medical application. A first medical case study, an orthognatic correction of the protrusion of the lower jaw was documented by pre- and post-operative hologram tomographies. As an application from the field of cultural heritage, holograms of the Husbäke bog body were made with mirror recording of side and front views. Copies of these holograms can be exhibited instead of the fragile bog body and allow non-contact measurement of the soft tissue thickness which is essential in facial reconstruction problems in forensic sciences. Examples for a virtual hologram tomography from a digitally recorded hologram, an outlook on possible future developments and a description of a true-colour texture recording system conclude the thesis.

Summary

This thesis develops and compares methods for three-dimensional surface shape measurement with short-pulsed holography by the technique of hologram tomography and presents examples for their applications in medicine and archeology. Hologram tomography is a two-step process: In the first step, the scattered light from the object surface is superimposed with a coherent reference beam, and the resulting interference pattern is recorded a high-resolution photographic emulsion. The exposure takes place within the pulse duration (in the present work, 35 ns). The developed emulsion, the so-called hologram, can be illuminated to recreate a copy of the original light field at the location of the object, the holographic real image. Projections of the real image are digitized with a camera at different distances from the hologram to yield a slice-by-slice representation of the intensity distribution of the wave field of the object. In contrast to direct surface measurements, the real image is stable for an unlimited time. The surface shape can thus be determined precisely without any temporal constraints. With the set-up described in this thesis, objects can theoretically be as large as the coherence length of the laser (5 m), defining a spherical nominal volume of appr. 65 m^3 which is recorded within the pulse duration of 35 ns. The comparison of novel and existing algorithms for hologram tomography is the main topic of the present work. It is complemented by an experimental comparison of the methods, a description of the holographic recording and reconstruction set-up and examples for the application of holography in medicine and in the conservation of cultural heritage.

The introductory chapter 1 compares different surface shape measurement principles. An emphasis is placed on medical applications where in maxillo-facial surgery a precise, three-dimensional documentation is needed. With conventional optical surface shape measurement methods, a facial scan takes several seconds and the obtainable resolution is thus lowered by motion artifacts due to heartbeat, breathing and involuntary movements. Additionally, the patient has to keep his eyes closed with many scanning devices to avoid damage from the collimated laser beam. Particularly with non-cooperating patients as for example young children, a harmless and fast recording technique like pulsed portrait holography is thus essential. The introduction closes with a brief overview on adjacent areas of research, medical imaging, computer vision and numerical microscopy.

Chapter 2 introduces the basic terms of holography and the concept of hologram perspective. Two purely numerical image deblurring techniques from microscopy were used in conjunction with holographic real images for the first time: inverse filtering and iterative deconvolution. Inverse filtering lowers the intensity from out-of-focus object points by reversing the imaging process. Iterative deconvolution achieves the same by simulation of the imaging process and subsequent correction of an object estimate by comparison with the actual real image. Both methods require the knowledge of the (incoherent) optical transfer function for which an analytical expression is derived. In semi-heuristic surface finding, the object surface is constituted by the points with maximum sharpness. A novel algorithm to estimate the image sharpness was developed which uses a weighted figure-of-merit to enhance the precision of the surface localization. Two methods for generation of perspective holograms are described: By mirror recording, multiple views of an object are recorded synchronously with a planar mirror. Alternatively, perspective surface shape measurements can be made with the, to my knowledge, novel technique of multi-perspective gradient averaging (MUPEGA) which makes use of the perspective of the holographic real image reconstructed from a partially illuminated planar hologram.

Chapter 3 describes the experimental set-up used for hologram recording and real image digitalisation. An emphasis is placed on the improvements, namely a speckle-projection device for structured object illumination and the mirror recording. The diaphragm to mask planar holograms for MUPEGA and the implementation of the deblurring algorithms are also described in this context.

Chapter 4 contains the experimental results: The maximum allowable velocity for an object surface ($v_{max} = 15.4 \pm 0.4$ m/s) and the holographic point spread function were determined. The extended field-of-view by mirror recording was demonstrated. The smallest projectable speckle pattern on human skin (0.5 mm at a contrast of 0.5) and the maximum pulse intensity for a holographic portrait with opened eyes (eye-safe exposure) were experimentally determined. The improved spatial resolution from weighted figure-of-merit sharpness calculation was determined by surface measurements of a well-defined test object. For the first time, numerical deblurring was applied to the holographic real image by inverse filtering and iterative deconvolution. The latter allowed to comprise several discrete object perspectives

into the same model which was illustrated by a recording with two orthogonal views. The high memory requirements limited the size of the models and their resolution with these two numerical techniques. In contrast, MUPEGA gave the highest spatial resolution (standard deviation reconstructed/actual surface of 0.89 ± 0.4 mm) with comparatively few computations. A surface shape measurement from a portrait hologram recorded with eye-safe illumination was obtained with MUPEGA, which thus meets the two main requirements in the medical context, sub-mm resolution and harmless recording.

As a first case study, the orthognatic correction of an overjet of the lower jaw in a patient suffering from the Marfan syndrome was documented with pre- and post-operative holograms. A data set from hologram tomography visualized the surgical procedure and was used by the surgeon for documentation and operational planning. As a second application of pulsed holography, a 2000 year old archeological exhibit, the Husbäke bog body, was made. With a 45°-mirror, both three-dimensional front and side view were recorded synchronously into the hologram. In addition to surface shape measurements by hologram tomography, volume holograms of the bog body can be displayed to replace the fragile original in exhibitions. To demonstrate the possibility of digital holography, a virtual hologram tomography with a depth resolution of approximately 8 mm was made from a small test object.

This real-time recording capability is one of the possible future developments for hologram tomography discussed in chapter 5. Appendix A contains an additional description of a texture recording set-up which allows to create photo-realistic surface models of human faces.

Contents

Chapter 1

Introduction

This thesis reports on ultra-fast surface shape measurements (topometry) by pulsed hologram recording for medical applications. Novel methods for topometry from pulsed holograms were developed and experimentally verified with a holographic camera set-up which was characterized and used for a first medical case study. All experiments have been conducted in the group for holography and laser technology of the research foundation `caesar` (center of advanced European studies and research) in Bonn which is associated to the Institute of Laser Medicine (ILM) at the University of Düsseldorf. A previous thesis on ultra-fast holographic topometry from J. Bongartz [Bon02] has been dedicated to a predecessor of the holographic camera. It covered the hologram recording process, medical and biological aspects like the scattering properties of the skin whereas this work emphasises the surface reconstruction with a technique called hologram tomography.

After an introduction into the medical context, an overview on existing topometric systems in general and optical systems in particular is given which is followed by a section on holography in medicine. An outline on the structure and the aims of the thesis conclude this first chapter.

1.1 Motivation

Three-dimensional images of living human subjects are of interest in a number of fields. Apart from the depiction of the human body in the arts - a topic with a long tradition in itself - 3D maps of the human body are well established for medical diagnosis. The majority of medical imaging systems uses either x-ray absorption (computer tomography, CT) , ultrasound (US) echo or radio-frequency magnetic resonance (MR) to gather information from inside the body. The development of digital computers made three-dimensional body models from CT, US and MR data sets possible. Optical systems are infrequently used in medicine despite their high potential in surgery [CAP$^+$02]: Maxillo-facial and cranio-facial defective positions are commonly documented with conventional photographs and the surgeon plans the treatment of congenital deformations and reconstructive surgery of tumor or accident patients with two-dimensional images.

The main applications of 3D surface data in medicine are diagnostics, preoperative planning, intraoperative navigation, surgical robotics, postoperative validation, training, telesurgery and epithesis design. An epithesis is a prosthetic replacement which is used when a part of the body or of the face is missing and no other surgical technique of reshaping is available. To achieve an optimum fit of the epithesis, the body surface shape has to be known. With current impression techniques, the missing part (the resection cavity in the case of tumor patients) is moulded by a plaster model which is subsequently transferred into a wax prototype and finally into a silicone resin epithesis with appropriate colour. A recent study indicates that facial protheses designed

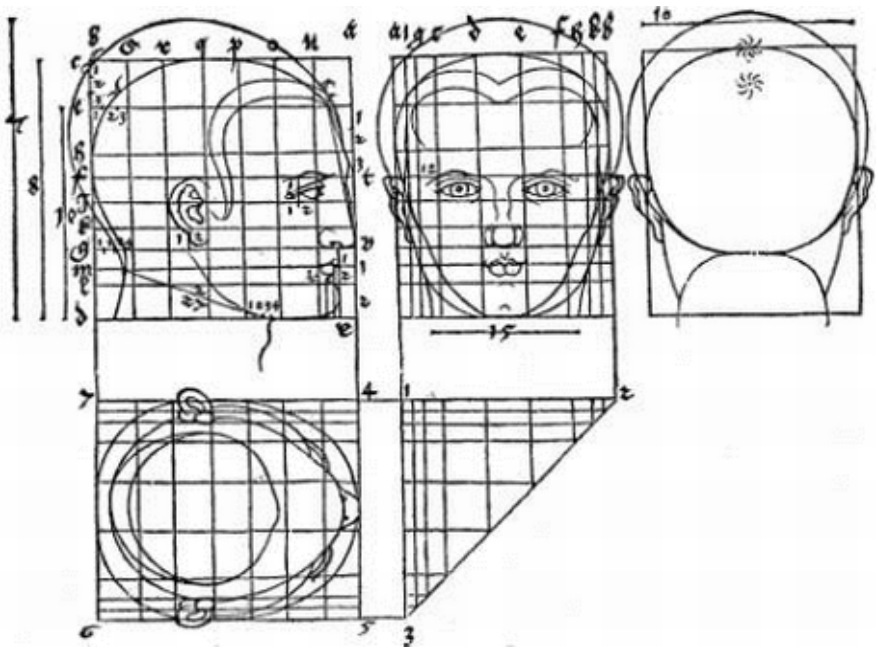

Figure 1.1: Orthographic projections of a human head from 1528. Source: [Dür]

with data sets from non-contact 3D data acquisition could yield protheses in a shorter time with a better fit, less discomfort and no contamination of the resection cavity with impression material [De02] if the data acquisition time of current laser scanning systems was reduced.

Simulations of surgical procedures can be made either virtually (on-screen with a numerical model) or on a physical representation of the data set of the patient, for example a rapid prototyping model of the skull. Virtual surgery simulations are currently based on CT data and can predict the effect of the treatment. They estimate the movement of the soft facial tissue due to the relocation of the skull bones, for example in surgery of the human mandible [EKL+01]. It is obvious that the results of any simulation cannot be more accurate than the initial data. For the current models which are based on the soft tissue information of CT data, this means that the poor contrast of soft tissue in conjunction with the dosage restrictions for ionizing radiation limit the spatial resolution of CT data sets. A typical CT scan has a slice thickness from 2 mm to 4 mm, even though for non-living subjects slice spacings of below one millimeter can be achieved at higher dosage rates. An additional uncertainty arises due to the complex problem of surface segmentation (i.e. the identification of different tissue types) from the CT and MR data [RTG98].

This thesis presents a first medical case study of a surgical procedure which was planned and documented with pulsed hologram tomography. An orthognatic correction of a long-face syndrome was recorded with post- and preoperative portrait holograms and a physical (rapid-prototyping) resin model of the pre-operation facial surface was provided for the surgeons' operation planning (Sec. 4.3.1).

In the forensic science, a common problem is the reconstruction of the faces of a deceased person from the dry skull to allow post-mortem identification. A study of Stephan and Henneberg [SH01] indicates that only one out of sixteen facial reconstructions with four commonly used methods leads to post-mortem identification at a statistically significant level. A data base of the correlations between facial surface and bone structure for persons of different age and gender could improve forensic reconstructions. An ancestor of such a database is described in 1528 by A. Dürer who advises to draw projections of many individual human heads of persons of different gender and age to define the characteristic proportions of old/young and male/female

portraits (Fig. 1.1). This training should give the artist the expertise to depict any given person realistically. Again, the predictions derived from any such data base strongly depend on the initial topometric measurements, in the case of Dürer the accuracy of the painter. Today the limited resolution and the slow acquisition speed of laser scanners still constitute an obstacle for automated determination of the proportions of a human head. Common scanning devices have exposure times of several seconds, which deteriorates the nominal accuracy due to motion artifacts. In forensic science, an artist's expertise is thus even today the only way of facial reconstruction if only a skull is available.

Facial measurements for automated identification of living people have recently become a major topic for research even though the tradition of using portraits for identification and authentication has a long tradition. G. J. Caesar was the first Roman emperor who issued coins showing the portrait of a living person (himself) [Saf98] - at the time, rather a political symbol than a security feature. More recently, the parliament of the federal republic of Germany passed a law which legitimizes that the passport includes "*additional biometric characteristics of the fingers, hands or face of the holder*"[Bun86] , indicating the increasing interest in three-dimensional facial measurements for identification. Current approaches in face recognition rely on conventional camera pictures and are prone to errors from different poses of the subject. They can also be easily conceived by masking and have considerable difficulties with beards and moustaches. The 3D information from two camera perspectives gives a typical measurement error of 28 mm (2% at a working distance of 1.4 m [BA00]). A precise 3D measurement system would therefore allow a drastically improved automated face recognition. With current hardware, even the simplified problem of automated face detection (i.e. the decision whether or not a certain camera image contains a face) can only be solved with error rates in the percent range [HL01].

These examples show that a fast, three-dimensional surface measurement system for human faces is needed in many disciplines. Existing solutions (Sec. 1.2) are too slow to allow high-resolution measurement on living people. Pulsed holography avoids this problem by an extremely short exposure time (sub-μs). The hologram holds the complete information of the light scattered from the surface of the object. It can be used at a later time to reconstruct the surface shape by hologram tomography.

1.2 Overview on 3D measurement systems

This section gives a brief overview on systems for spatial measurements. Due to their large number, a complete description is not intended, but only an outline on the different principles is given. The scheme arranges the topometry systems centered on those for optical measurements.

Current topometry systems cover approximately 30 orders of magnitude from force microscopes which operate within the radius of single atoms (appr. 10^{-10}m) up to stellar interferometers which measure the angular diameter of stars and - with spectral Doppler shift determination - reveal the distance of *Cepheid* stars (hundreds of parsec, 1 parsec $\approx 3 \cdot 10^{16}$ m) [LKB+00]. Three groups of 3D systems are shown in Fig. 1.2 : Contact-based measurements rely on the force between an object and a probe placed in the vicinity of it, whereas non-contact systems rely on the observation of fields interacting with the object[1]. Microscopic (atomic force microscopy) and macroscopic (coordinate measurement machines) implementations of contact measurements exist. A few systems can be classified in both groups. They appear in the semi-contact group, as, for example, aperture-less near-field microscopy where the tip of an atomic force microscope causes the high local field strength for infra-red spectroscopy. One can divide the non-contact systems further into passive and active systems. Passive systems are mostly used where the objects under consideration are too large for illumination, for example

[1] In the strict quantum mechanical sense, forces are also attributed to an exchange of field quanta.

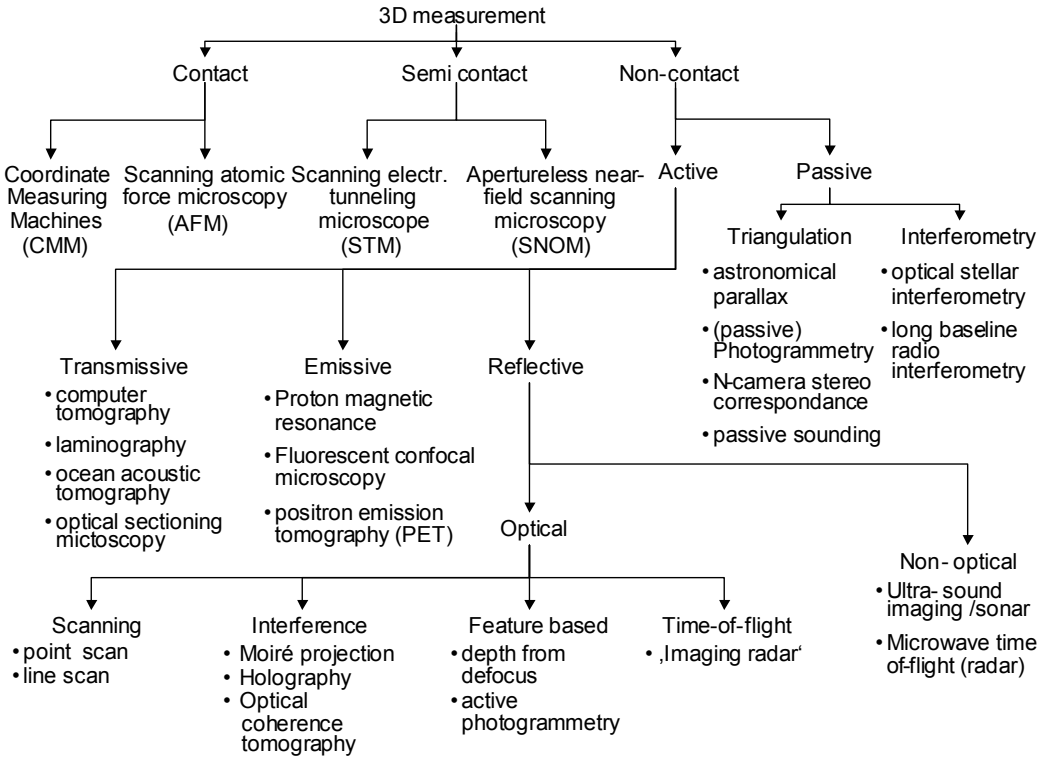

Figure 1.2: Taxonomy of three-dimensional measurement systems

in astronomy or geography. In these applications, the intrinsic fields emitted by the objects are used for topometry. Photogrammetry, for example, is an important tool for the extraction of geomorphology elevation models from aerial photographs. In Fig. 1.2, it is called passive photogrammetry to distinct it from photogrammetry with (active) pattern projection. Passive photogrammetry is also known under the name of n-camera correspondence or, for n=2, stereo correspondence in computer sciences [BSK01].

Active non-contact systems image objects which are small and close enough to allow a wave to travel from the object to a detector and vice versa. According to the signal path, three families exist: If a wave field passes through the sample, the signal path is transmissive whereas it is reflective if the surface of the object or an internal feature scatters the radiation. A third family with emissive signal path includes systems where the object itself is stimulated to emit radiation. All magnetic resonance imaging systems belong to this family, including 3D proton magnetic resonance imaging (MRI) and a number of less prominent applications with atomic spin [GHNW00]. The spatial resolution of MRI images depends on the exposure and the field strength used. State-of-the-art systems comprise magnetic field strengths up to 7 T, allowing imaging with an in-slice spatial resolution of 0.5 mm$\times$0.5 mm with slice acquisition times of 200 ms. At complete head can thus be acquired at a slice thickness of 5 mm within several seconds [DEG$^+$].

Fluorescent confocal microscopy also belongs to the emissive systems as well as positron emission tomography (PET) which detects the co-linearly emitted pair of 511 keV γ-rays from positron-electron annihilation. PET allows to locate pathogenic tissue inside the body volume. Due to the short wave-length of the radiation, its resolution is not limited by diffraction effects, but by the shot-noise from the photon counting statistic. In order to minimize the irradiation, imaging with as few photons as possible is sought. If the dosage rate is of less concern, for example in animal PET scanners, they can achieve a spatial resolution determined by the physical resolving capability of the detector in the range of 1 mm [GB02]. An important medical applications with transmissive signal path is computer tomography where different absorption

cross-sections of an object or a patient are acquired with x-rays. The different angular projections are numerically combined to a three-dimensional model using the inverse Radon transform or - for more complex geometries - simultaneous algebraic reconstruction (SART, [AK84]). The latter depends on an iterative approximation of the object under consideration, a technique also used with the PET scanner. In contrast to the inverse Radon transform, the SART algorithm can also reconstruct 3D objects measured under a restricted view angle (i.e. views from less than 180°). In this thesis, an approach of SART has been applied to hologram tomography where a restricted angle of view on the object prohibits the Radon transform.

A similar approach is well known in optical sectioning microscopy where a number of ordinary light microscope images acquired at different focal planes are combined to a three-dimensional image volume. The light from out-of-focal object points contributes to a blur-like image degradation in optical microscopy which can be removed iteratively by a so-called deconvolution, a numerical technique which is also used for holography in this thesis. A distinct feature of data sets from optical sectioning microscopy is a difference between axial (i.e. parallel to the main direction of light propagation) and lateral spatial resolution. This phenomenon is also a common feature in hologram tomography where the lateral resolution is usually higher than the axial resolution.

Some transmissive techniques with non-electromagnetic waves exist, for example ocean acoustic tomography where the propagation of a sound field reveals the state (speed, temperature, etc.) of the ocean, but common acoustical systems use reflective signal paths. Ultrasound imaging (US) is a popular topometry system in medical application despite the limited resolution (several mm) which is often lowered by artifacts similar to the laser speckle in optical hologram reconstruction. For three-dimensional imaging, US combines multiple scans and is thus prone to motion artifacts [KHJS02]. In engineering, sound waves are used for example in sound navigation and ranging (SONAR).

In the field of optical shape measurement, a number of reflective systems comprises a scanning projection together with a conventional camera. The scanning can either be done with a single light ray (point scan) or a light line (line scan) or several lines (fringe projection). With point scan, the intersection of the light ray with the surface is triangulated. A single 3D-point is thus acquired with each camera frame, making the process slow for extended objects or high resolution. 3D point scanners can achieve a spatial resolution down to 20 μm [Har02a] but tend to acquire data slowly at rates of several thousand points per second. The faster line scan can lead to ambiguous 3D models with particular surface shapes. The highest speed is achieved with fringe projection at the price that the surface reconstruction is numerically complicated (involving the so-called phase unwrapping problem [JB94]). A similar approach is active photogrammetry where a high-contrast (random) pattern is projected on a surface to allow the identification of individual surface points in camera images taken from different perspectives. To build a 3D model from the camera images, the problem of point-to-point correspondence has to be solved: A given surface point has to be identified in all camera images. Obstructed and ambiguous surface points make this concept impractical: Despite of their fast and synchronous object acquisition with multiple cameras, commercially available active photogrammetry systems can only identify less than ten thousand object surface points on a human face and are thus limited to spatial resolutions in the order of 3 mm [Bon02].

A different range-finding principle is time-of-flight measurement, better known as radio detecting and ranging (RADAR) with microwaves. A spatial resolution of 1 mm requires detection of the time-of-flight with an accuracy of 3 ps, making direct time of flight measurement impractical for high-resolution medical topometry. The time-of-flight principle is indirectly also used with interferometric measurements: This group includes optical coherence tomography which uses the coherence properties of scattered visible or infra-red light to detect structures beneath the skin. Moiré systems comprise a mixture of projection and interferometric techniques: The Moiré fringes are not generated by wave interference, but a double intensity modulation in both

the illumination and the detection light path. A similar approach was introduced by Bongartz with the structured object illumination [Bon02], a technique which was enhanced by structured speckle projection in the present work. Holographic recordings have the advantage of high resolution and can be recorded with pulsed radiation within fractions of a microsecond [Har97]. They do not require active tracking of objects or post-exposure calibration and can store huge amounts of data within an inexpensive photo-emulsion, making them particularly useful for the topometry of short-lived phenomena which occur within a large recording area.

1.2.1 Holography

The concept of optical holography was introduced by D. Gabor [Gab48] to overcome limitations in electron microscopy. Gabor wanted to use a lensless imaging system due to the poor quality of electron lenses. He intended to record an electron (particle) wave field on a medium and to reconstruct it optically at a later time. The reconstruction with visible light yielded a superior resolution as optical components had (and still have) a higher quality compared to electron lenses. Although this application of holography has never actually been used in electron microscopy, the development of laser light sources led to optical holograms. The high coherence length of the laser allowed E.N. Leith and J. Upatnieks to record extended objects in off-axis geometries [LU63]. Pulsed lasers [JM70] made the holography of living subjects and human portrait holograms [Sie68] [Ans70] possible. Ruby lasers (wavelength $\lambda = 694$ nm) were used for the first portrait holograms. The high penetration depth of red light (appr. 3 mm, [Lip93]) is apparent in these portraits in a translucent appearance of the skin. For ruby portrait holograms, Bjelkhagen [Bje92] recommends the use of cosmetic face powder and green lipstick to avoid this waxlike (death mask) effect. Those first portrait holograms were used mainly for artistic or advertisement purposes, although already in 1971, E. Ingelstam had predicted in his presentation speech for the nobel prize in physics which was awarded to Gabor for *"his invention and development of the holographic method"* that holography [of acoustic wave fields] *"should be of value for medical diagnosis"* [Ing71].

Pulsed holography is used for topometry in engineering applications under the name of hologrammetry (from holography and photogrammetry) [Wat93]. In aerosol and flow analysis (holographic particle imaging velocimetry, HPIV), the position of small test particles is measured twice by double-exposure [PM00] [May97]. Velocity vectors can then be calculated by identification of the shift of the test particles. With a single, pulsed exposure, Harigel [Har97] measured the position and the thickness of bubble chamber tracks which indicated the trajectories and the mass of charged particles . The advantage of holography in these applications lies in the extremely short recording time (determined by the pulse duration of the laser) in conjunction with the extraordinarily large volume and high precision of the recording. Despite the good results obtained with particle track holography, novel solid state (silicon stripe and pixel detectors) and gas wire detectors made the bubble chamber obsolete for particle track measurements. Single-pulse topometry has also been applied to marine zoological studies [KWH$^+$96] where the hologram allows one to identify the incidence of different plankton species within a large volume of water.

Holographic surface topometry systems are commonly used with a double exposure technique to measure spatial shifts, for example to determine acoustic vibrations of musical instruments, car tires and mechanical components [Ost89]. The two hologram reconstructions can either interfere constructively (indicating a $2\pi \times n$ phase shift) or destructively. The superposition of the two holograms thus yields images with a characteristic fringe pattern. By appropriate choice of the double exposure delay, the acoustical node lines for a given frequency can be identified with this stroboscopic approach.

1.2.2 Hologram tomography for topometry in medical applications

For medical application, i.e. the topometry of living human subjects, the movements of the patient have to be negligible within the duration of the measurement process. The patient movements are partly involuntary due to heartbeat or breathing, but even voluntary movements cannot be avoided with all patients, for example with children. This means that in general the measurements have to be conducted within a fraction of a second- as a photographic rule-of-thumb, portraits recorded with an exposure time of less than 20 ms show no visible motion artifacts (with the exception of athletes in fast sport events). Current scanning techniques generally have acquisition times of several seconds and can achieve short measurement times only at the cost of reduced spatial resolution which should be below one millimeter for medical application.

Apart from the requirement of high-speed data acquisition, another concern in this context is the eye-safeness. The use of visible light is an advantage over CT-based topometry, where due to the ionizing effects, a trade-off between resolution and radiation has to be made for each exposure. The dosage of multiple CT accumulates- multiple accumulates and multiple exposures thus pose an even higher risk. Topometry with visible laser light requires that the maximum intensity for non-ionizing radiation is not exceeded [oNIRP00]. As the intensity values for the human eye are different from those for the skin, a system exceeding the former can still be used if the patient wears protective goggles, but since even small laser goggles inevitably deform the skin surface and occlude the face partially, a topometry system allowing open-eye measurement is preferable.

In his PhD thesis, J. Bongartz described a camera for fast pulsed portrait holography of living human subjects [Bon02]. The system uses structured illumination for surface topometry. The projected stripe pattern results in high-contrast regions in the real image and allows the localization of the surface (semi-heuristic surface finding). A three-dimensional computer model is built from measurements of projections of the optically reconstructed real image (hologram tomography). One disadvantage of this stripe projection method that a high contrast is only achieved at certain distances. This can be explained by the Talbot effect: the *"diffraction of coherent light on a planar, periodic structure of periodicity d causes images of the structure at distances of* $z_n = 2d^2/\lambda$*"*.[Pau99]. This diffraction self-reproduction effect can be described with the ABCD matrix formalism for general optical systems [KK01] and causes the projected high-contrast fringes to vanish in between these distances z_n. Another limitation of the set-up described by Bongartz is the restriction of the geometry to a single, frontal perspective, and the high intensity which exceeds the safety threshold for eye-safe recordings.

1.3 Aims and outline

The aim of the present work is the development and the evaluation of novel methods for holographic surface shape measurements and their experimental realization and evaluation. Methods from different areas of research (Fig.1.3) are examined on their suitability for hologram tomography in the medical context. They include microscopy techniques like numerical image deblurring (i.e. the removal of blurred image components) as well as 3D reconstruction algorithms from computed tomography and the field of computer vision and pattern recognition where numerous solutions to topometric problems have been proposed. I present a - to my knowledge - novel algorithm for multiple perspective based 3D measurement by gradient averaging (MUPEGA) which allows for the first time a surface shape measurement from a portrait hologram recorded with eye-safe patient illumination. The experiments lead to a topometry system comprising a holographic camera, an optical reconstruction set-up and a software to construct 3D computer models which allow to plan ahead complex maxillo-facial surgery.

This first introductory chapter is followed by a description of the methods used for hologram tomography (Chapter 2). The formalisms of hologram recording, laser speckle formation

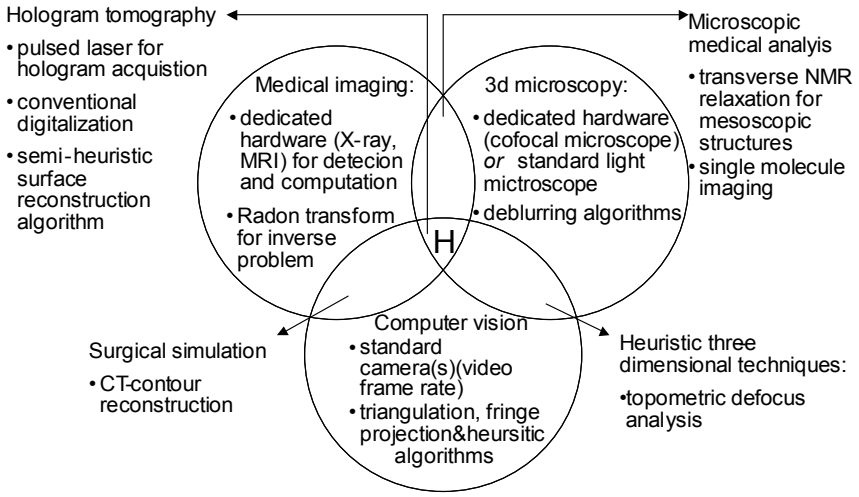

Figure 1.3: Hologram tomography and adjacent areas of research

and the holographic point-spread-function (Sec. 2.1) are essential to understand the concepts of topometry by image deblurring (Sec. 2.2) and semi-heuristic surface finding (Sec. 2.3). Hologram perspective (Sec. 2.4) is the key concept for the mirror recording of holograms and multi-perspective gradient averaging.

The next chapter introduces the experimental system for hologram recording (Sec. 3.1), the recording medium (Sec. 3.2) and the optical reconstruction set-up (Sec. 3.3) as well as implementations of the previously described methods (Sec. 3.4). I present the results and the discussion of the experiments in chapter 4 which contains four main parts. It starts with a characterization of the holographic camera with a determination of its the point-spread-function, its temporal resolution and considerations on laser speckle projection onto human skin (Sec.4.1). The comparison of the different approaches to surface topometry (Sec. 4.2) constitutes the second part of chapter 4 whereas the last two sections describe applications of hologram tomography: The first medical case study and an example for the application of holography in cultural heritage are described in section 4.3. As an outlook, a digitally recorded hologram as the basis for a digital hologram tomography is also presented (Sec. 4.4).

Conclusions on the results are described in chapter 5, followed by the appendix on a texturing algorithm for photo-realistic true-colour computer models.

Chapter 2

Methods

In this chapter, the methods for holographic surface shape measurements (topometry) on holographic recordings are presented. Pulsed holography allows the recording of a three-dimensional image of a large object, for example the face of a living human, within a short exposure time at a high resolution. With the experimental set-up described in Sec. 3, the exposure takes only 35 ns and contains object features down to single hairs. The holographically recorded wave field can be reconstructed for precise 3D measurements for an infinite time span. This principle, sometimes referred to as hologrammetry, relies on the huge storage capacity (3000 line pairs per mm) of holographic recording materials in combination with the large imagable volume which is determined by the coherence length of the recording laser. Modern solid-state laser achieve coherence lengths of several meters with visible light (wave length around half a micrometer).

The hologrammetry of homogeneous contiguous surfaces requires special treatment as opposed to the reconstruction of point-like objects which can be located by automated peak-fitting [GL80]. The hologram of a point-like object thus allows a straight-forward determination of the axial object distance, in contrast to the hologram of a contiguous surface which cannot simply be used to determine the distance from the hologram to the surface. A similar problem is well-known in photography and microscopy: The correct focal distance (the equivalent to the distance of the surface) cannot be precisely determined if the surface is too homogeneous. Accurate focusing is only possible at the edges of a surface or object features. Similarly, the axial coordinate in holographic recordings cannot simply be measured with the techniques developed for point-like objects: The points of maximum intensity do not necessarily belong to the surface with contiguous surfaces.

For holographic surface shape measurement, one thus needs to determine the surface location based on the intensity of the real image volume. Bongartz [Bon02] presented the approach of structured object illumination: high-contrast patterns are projected onto homogeneous areas of the object - for example the forehead of a human face. A scan of projections of the real image volume (hologram tomography) allows one to identify the points of maximum image sharpness which constitute the surface of the object (semi-heuristic surface finding).

The problems encountered in maximum sharpness hologram tomography can be formulated as an image blur problem: Each hologram tomography slice contains intensity from focused object points as well as defocused or blurred image intensity from out-of-focus points. The latter contribute to a background intensity and can hinder the semi-heuristic surface finding. The purpose of this chapter is to present novel methods for improved, eye-safe surface reconstruction from pulsed portrait holograms. These methods are inspired by diverse problems in microscopy, computer sciences, and radiology. In this chapter, five enhanced or novel methods for 3D hologram tomography are described:

- real image deconvolution by *inverse filtering*

- *iterative* real image deconvolution
- semi-heuristic surface reconstruction by weighted neighbourhoods
- multiple-perspective gradient averaging (MUPEGA)
- mirror recording of multiple perspectives of an object into one hologram

The first two methods stem from microscopy with incoherent light where they are used to reduce out-of-focal light. They aim to remove the unsharp (i.e. blurred) contributions to the image and are thus known as deblurring algorithms. They rely on the knowledge of the point-spread-function of the imaging system which either has to be calculated *ab initio* or measured. In section 2.2, the point-spread function of the holographic imaging system is, an experimental measurement of the PSF is presented in section 4.1.1. The two deblurring methods, iterative deconvolution and inverse filtering, were adapted for holography. An improved algorithm for surface detection with weighted neighbourhoods is presented. The semi-heuristic surface detection scheme can be applied to the intensity of the real image directly or after deblurring as described in section 2.3.

As experiments indicated that the actual resolution achieved with semi-heuristic surface detection (appr. 2.75 mm) is far from the diffraction limit of a few micrometers (Sec. 4.2.1) , the MUPEGA algorithm has been developed. It combines the information from multiple views obtained from a single, large hologram by masking of the hologram with a diaphragm. The resulting hologram reconstructions have a lower (diffraction-limited) resolution, but constitute views with a distinct hologram perspective onto the object. Section 2.4 introduces the concept of perspective from holograms and how perspective reconstructions can be obtained from a single, planar hologram. Alternatively, hologram perspective can be achieved by mirror recording: The light field scattered by the object is recorded from multiple views by placing a plane mirror next to it. These different views can also be described by the concept of perspective. Mirror recording and MUPEGA are therefore presented in the context of hologram perspective.

For holography, the iterative deconvolution algorithm was extended to combine several mirror perspective holograms of an object as opposed to the single-perspective approach from microscopy. A similar multi-view technique, simultaneous algebraic reconstruction (SART), is known in radiology where it is used to reconstruct 3D objects which can not be x-rayed from all angles [AK84]. In contrast to microscopy, the blur removal is of less concern in SART as the PSF of conventional x-ray imaging systems can be approximated by a line.

The chapter starts with a brief introduction on the object representation and the basic holographic terms, including the concept of hologram tomography. The following section introduces the holographic point spread function and the two image deconvolution algorithms, including iterative deconvolution with multiple perspectives. The last section contains a description of hologram perspective both from mirror recording and from aperture masking for the MUPEGA algorithm. Prior to the main part of the chapter, some definitions are given.

Object representation, coordinate frame and Gaussian beams

Topometry systems with reflective light path measure the intensity scattered by the object surface. The surface is represented by the object function $O(x, y, z)$ which describes the (positive and real) reflectivity of the object surface. With hologram tomography, the intensity of projections of the holographic real image $I(x, y, z)$ can be measured. The problem of holographic surface topometry is to determine the location of a contiguous object surface, i.e. all points where $O(x, y, z) \neq 0$ if the reflectivity of the surface is non-zero for all surface points[1]. In general, this problem is non-trivial even when further assumptions on the reflectivity of the surface

[1] Surfaces with zero reflectivity cannot be imaged at all with optical means

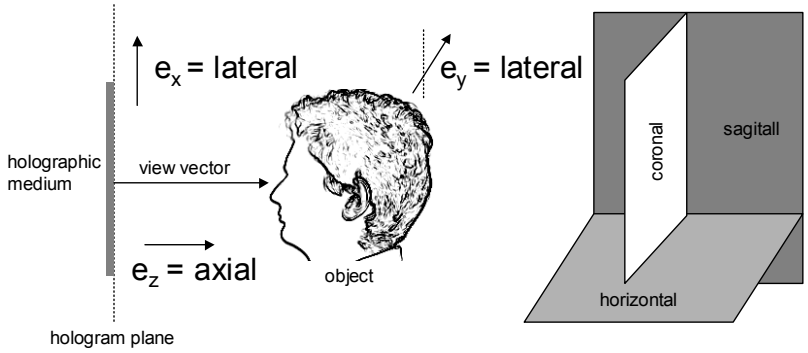

Figure 2.1: Coordinate frame with hologram plane, lateral and axial coordinate vectors

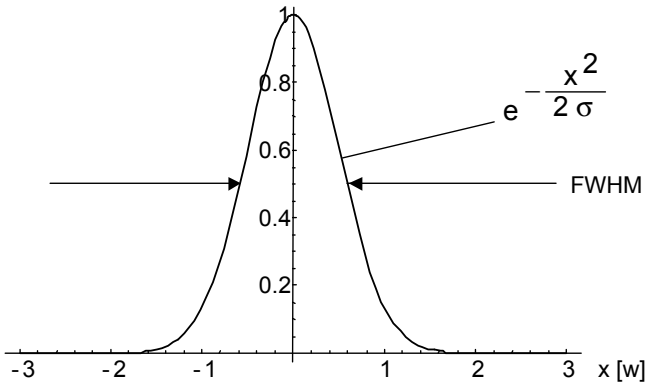

Figure 2.2: Gaussian intensity distribution with width w, standard deviation $\sigma = 1/4$ and full-width at half maximum $FWHM = 1.177$.

are made [KO96]. For example, a superposition of the intensities from laterally separated object points might cause a maximum sum intensities at locations separated from the actual surface.

In holography, the object wave field is commonly reconstructed from a planar hologram. One distinguishes thus lateral and axial coordinates. The axial coordinate axis is parallel to the propagation direction of the object wave field (i.e from the hologram towards the object) and is denoted by $\vec{e}_z$. The lateral coordinate vectors are orthogonal to the axial coordinate vector and thus parallel to the holographic recording medium which defines the hologram plane (Fig. 2.1). Unless otherwise stated, the plane defined by $\vec{e}_z$ and $\vec{e}_x$ corresponds to the sagittal plane, the lateral coordinates $\vec{e}_x$ and $\vec{e}_y$ to the coronal plane (respectively the hologram plane) and $\vec{e}_y, \vec{e}_z$ to the horizontal plane of the patient. The vector pointing from the central point of the hologram towards the object is called the view vector. For the analysis of holographic light fields, a spatial intensity distribution which is often used as a convenient basis for analysis is the Gaussian beam (Fig. 2.2):

$$g(x,y,z) = \left(\frac{w_0}{w(z)}\right)^2 e^{-2\frac{x^2+y^2}{w(z)^2}} \tag{2.1}$$

$$w(z) = w_0\sqrt{1+\frac{z^2}{z_R^2}} \tag{2.2}$$

where z_R is called the Rayleigh length of the beam and w_0 the waist of the Gaussian beam. Projections of the Gaussian beam onto a plane parallel to the direction of propagation, the z

axis, yield an intensity of

$$g(x,y) = I_0 e^{-2\frac{x^2+y^2}{w^2}} \tag{2.3}$$

which is characterized by its width w. The one-dimensional Gaussian curve

$$g(x) = I_0 e^{-2\frac{x^2}{w^2}} \tag{2.4}$$

often occurs in statistical phenomena and can be used for the determination of the position of peaks in experimental data. The Gaussian peak has a full-width at half maximum (FWHM) of

$$FWHM = 2w\sqrt{\frac{\ln(2)}{2}} \tag{2.5}$$

$$\approx 1.177w \tag{2.6}$$

A statistical distribution following a Gaussian intensity distribution (also called normal distribution) has a standard deviation of

$$\sigma = w/4 \tag{2.7}$$

2.1 Holographic imaging

Holography is defined as the storage and reconstruction of wave fields by the recording of their interference pattern. The holographic imaging formalism has been described in many publications in detail [Ost89] [EA93]. This section summarizes the basic aspects of holography and explains how an object wave field is reconstructed and measured (hologram tomography). The requirements for the holographic recording material are illustrated by the hologram formed by two plane waves. The spatial resolution obtainable by finite holograms is deduced from another basic example, the hologram of a point source. This section is concluded by a brief review on laser speckle formation. Laser speckle is present in hologram tomography both as a source of noise as well as a tool for artificial contrast enhancement by speckle projection.

2.1.1 Hologram recording

Maxwell's equations describe the propagation of electromagnetic fields. In the absence of volume charges and currents they are

$$\nabla \times \mathbf{B}(\mathbf{x},t) - \frac{1}{c^2}\frac{\partial \mathbf{E}(\mathbf{x},t)}{\partial t} = 0 \tag{2.8}$$

$$\nabla \times \mathbf{E}(\mathbf{x},t) + \frac{\partial \mathbf{B}(\mathbf{x},t)}{\partial t} = 0 \tag{2.9}$$

$$\nabla \cdot \mathbf{E}(\mathbf{x},t) = 0 \tag{2.10}$$

$$\nabla \cdot \mathbf{B}(\mathbf{x},t) = 0 \tag{2.11}$$

The electric field vector **E** and the magnetic flux vector **B** describe the electromagnetic field. Any solution **V** for either **B** or **E** can be written as a sum of harmonic waves

$$\mathbf{V}(\mathbf{x},t) = \sum_{\omega} \Re\left[\mathbf{U}(\mathbf{x})\exp(i\omega t)\right] \tag{2.12}$$

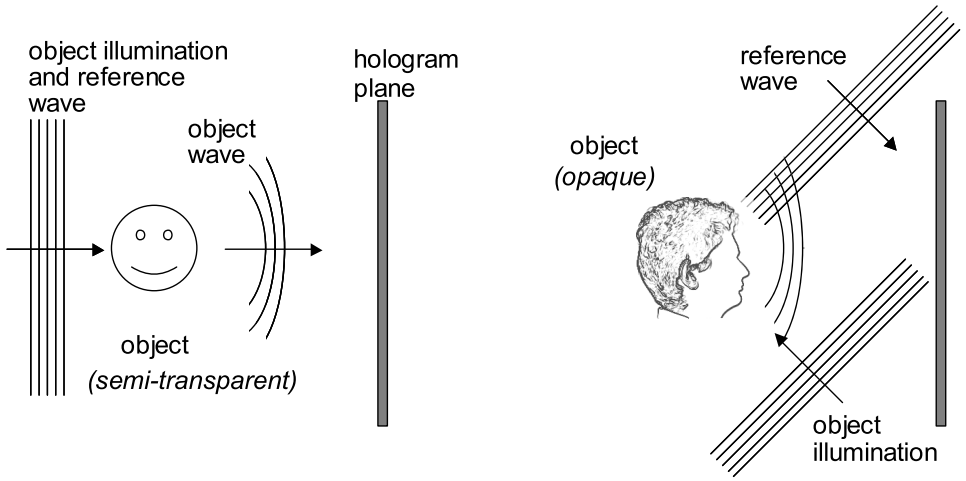

Figure 2.3: Inline (Gabor) set-up (left) and off-axis (Leith-Upatnieks) recording geometry

where the complex vector function $\mathbf{U}(\mathbf{x})$ satisfies the Helmholtz equation:

$$\nabla^2\mathbf{U}(\mathbf{x}) + k^2\mathbf{U}(\mathbf{x}) \;=\; 0 \tag{2.13}$$

The wavenumber vector **k** and the frequency $\omega/2\pi$ are connected via the dispersion relation

$$k^2 \;=\; \frac{\omega^2}{c^2} \tag{2.14}$$

where c denotes the speed of light and k^2 is the square of the magnitude of the wavenumber vector. When only radiation with one polarization is present, the vector Helmholtz equation simplifies to a scalar equation:

$$\nabla^2 U(\mathbf{x}) + k^2 U(\mathbf{x}) \;=\; 0 \tag{2.15}$$

Any solution of 2.15 is uniquely defined by appropriate boundary conditions. For example U is determined within a volume by the value of U on a closed surface of this volume (Dirichlet boundary conditions). In the following, only static solutions of the Helmholtz equation are considered. With pulsed laser light sources, this implies that in the time scale of the pulse duration, the object under consideration must not move considerably. This assumption is verified experimentally in section 4.1.2. Furthermore, only solutions with a single frequency ω and a single polarization are considered. These requirements are met with single mode laser radiation and appropriate polarizers.

If both amplitude and phase of such a static, monochromatic, linearly polarized electromagnetic field are known on a surface enclosing a homogeneous volume, the complete wave field inside the volume is uniquely determined[2]: This is the basic principle of holographic wave field recording. In hologram tomography, one is interested in the wave field scattered by an object, the object wave field. With holography, the object wave field can be reconstructed to yield information on the object surface at a later time. This hologram reconstruction can either be a physical process in which an identical copy of the object wave field is created (optical hologram reconstruction) or a numerical reconstruction where the hologram is recorded digitally.

Reference wave

On the hologram surface, both amplitude and phase of the object wave have to be measured. As physical detectors are sensitive to the intensity $I \propto |U|^2$ only, the phase must be measured

[2] In the absence of electric charges in the inside of the volume

indirectly : A coherent reference wave R is superimposed and interferes to an intensity of

$$I = |U+R|^2 \tag{2.16}$$
$$= U^*U + U^*R + R^*U + R^*R \tag{2.17}$$

For practical reasons, the hologram surface is usually not closed in holographic settings but often a finite area on a plane, the hologram plane. The identity of the object wave field and its reconstruction is hence not exact in a mathematically rigid way. Fig. 2.3 shows the two basic types of hologram geometries, the in-line or Gabor-type set-up, where scattered radiation from a semi-transparent object interferes with the unscattered radiation and the off-axis or Leith-Upatnieks set-up, where scattered radiation from the object interferes with an off-axis reference wave.

The intensity I in equation (2.17) contains terms which are independent from the relative phase of U and R as well as phase-dependent terms. By the choice of an appropriate reference wave (for example a plane wave), the term R^*R can be made constant over the whole hologram. The term U^*U is phase-independent. In the case of an object wave field with spatially constant amplitude $|U|$, this term is also constant. U^*R and R^*U encode the relative phase ϕ of U and R into the intensity.

Optical reconstruction

In an analog holographic medium, the intensity distribution of the interference pattern is linearly transferred into a distribution of the absorption coefficient (amplitude hologram) or a distribution of the refractive index (phase hologram). The transmittance $T(\xi,\eta)$ (amplitude hologram) or the refractive index $n(\xi,\eta)$ (phase hologram) in the hologram plane is a function of the relative phase of object and reference wave. In the following, coordinates in the hologram plane are written in Greek letters (ξ,η) to distinguish them from object-space coordinates (x,y,z). The transfer curve of the recording medium (for example, Fig. 3.6) describes the relation between intensity and transmittance or reflective index. An ideal holographic medium has a linear transfer curve. In amplitude holograms, the transmittance decreases approximately linearly with the illumination intensity with slope $\tau < 0$. The intensity of the interference pattern thus causes a space-dependent variation the transmittance of the hologram plane. For optical hologram reconstruction, the hologram is illuminated by the complex conjugate wave field R^* of the reference wave field. If the reference wave is a plane wave, the reconstruction wave R^* is also a plane wave with an opposite wavenumber vector **k**. Similarly, the complex conjugate of a divergent spherical wave is a convergent spherical wave. In general, the complex conjugate of any wave field can be interpreted as the wave field with inverse propagation direction. After passing through the developed hologram, the reconstruction wave has acquired a modulation (spatial indices are omitted):

$$\tilde{R}^* = T(\xi,\eta)R^* \tag{2.18}$$
$$= T_0R^* + \tau\left(R^*R^*R + R^*U^*R + R^*U^*U + R^*R^*U\right)) \tag{2.19}$$
$$= (T_0+\tau R^*R)R^* \;+\; \tau U^*UR^* \;+\; \tau R^*RU^* \;+\; \tau R^*R^*U \tag{2.20}$$

These terms can be identified with four separate wave fields [Mes99]:

$(T_0+\tau R^*R)R^*$ The complex conjugate wave-front is attenuated by the hologram, the phase is unchanged. This term is called the *zeroth order* in reference to the diffraction of a grating.

τU^*UR^* When U^*U is only approximately spatially constant, this term is a distorted reconstruction wave R^*. It is sometimes called the *halo*. If U^*U is constant, this contribution has the same geometry as the zeroth order

$\tau R^* R U^*$ This is the complex conjugate of the object wave U times a constant factor: A reconstruction of the object wave field with inverse propagation direction. This wave field is called *real image* or *+1th order* of the hologram.

$\tau R^* R^* U$ In reference to the diffraction at a grating, this term is called the *-1th order*, as in some holographic set-ups it has similar geometric properties as the 1st order.

By illumination of the hologram with the reference wave instead of its complex conjugate, the fourth term turns into $\tau R^* R U$, the so-called *virtual image* . The virtual image is a copy of the object wave field (multiplied by a constant) and has the same propagation direction as the original wave field. The reconstruction of the object wave field can be seen as a diffraction of the reconstruction wave on a particular grating. In an amplitude hologram, a fraction of the reconstruction wave is absorbed and another fraction is diffracted into the reconstructed object wave field. In a phase hologram, the modulation of the refractive index retards the reconstruction wave locally. This also causes a diffraction into the reconstructed object wave field. The main advantage of the phase hologram is the higher diffraction efficiency (defined as the ratio between the intensity diffracted into the first order and the intensity of the reconstruction wave), as the reconstruction wave field is not attenuated.

Up to now the hologram medium was regarded as a surface. Any physical holographic recording medium has a finite thickness. If the recording medium is thin compared to the interference fringe spacing, the hologram is called a surface hologram . If, on the other hand, the medium is thick enough to comprise many ($N \gg 1$) fringe layers, it is called a volume hologram. One should note that whether a holographic medium can be used for surface or volume holograms at a certain wavelength depends on the thickness of the medium as well as the geometry of the set-up (Sec. 2.32).

In this thesis, all optically reconstructed holograms were recorded on a 30 μm thick silver-halide emulsion. The recorded holograms are neither pure volume nor pure surface types. With the recording geometry described in chapter 3, they comprise only a small number of fringes ($N \approx 27$) and have the characteristics of surface type holograms.

Numerical reconstruction

Instead of optical reconstruction, the object wave field can also be reconstructed numerically from the intensity distribution of the hologram. The reconstruction of the object wave field is based on the measurement of $I(\xi,\eta) = |R+U|^2$ on the hologram plane. Numerical reconstruction assumes that the phase of the reference wave R is known, for example, that R is a normally impinging plane wave.

If the object wave field originates from a finite region in space at, for example negative axial coordinates and the hologram plane is at $z = 0$, the Rayleigh-Sommerfeld integral gives the wave field U for axial coordinates $z \gg \lambda$ larger than the wavelength [Har02b]:

$$U(x,y,z) = \frac{1}{\imath\lambda} \iint U(\xi,\eta) \frac{\exp(\imath k\rho)}{\rho} \cos(\theta) d\xi d\eta \tag{2.21}$$

$$\rho = \sqrt{z^2 + (\xi - x)^2 + (\eta - y)^2} \tag{2.22}$$

θ is the angle between the normal vector of the hologram and the observation position (x,y,z). For small θ, the obliquity factor $\cos(\theta)$ can be approximated by one. The reconstruction of U is based on the numerical calculation of equation (2.22). Two simplifications can be used to approximate the kernel of (2.22). Expansion of $\frac{\rho}{z} = \sqrt{1+\epsilon}$ in $\epsilon = (\frac{\eta-y}{z})^2 + (\frac{\xi-x}{z})^2$ yields

$$\frac{\rho}{z} = \left(1 + \frac{1}{2}\left(\frac{\xi - x}{z}\right)^2 + \frac{1}{2}\left(\frac{\eta - y}{z}\right)^2 + \dots\right) \tag{2.23}$$

The zeroth and the first order of the expansion are known as the Fresnel approximation. In the far-field, the first order (the quadratic terms in 2.23) can also be omi tted for the Fraunhofer approximation. Both can be used in numerical holography reconstruction for efficient object wave field calculation [Sko01].

2.1.2 Hologram tomography

To obtain a representation of the optically reconstructed real image volume, Bongartz, Giel and Hering introduced the digitalisation via the so-called hologram tomography [BGH00]. The real image is projected onto a screen at distance ζ: The complete real image is thus presented as a series $I^{\zeta}(\xi, \eta)$ of two-dimensional intensity projections of the real image. Due to the 1:1 correspondence of reconstructed and original light field, they are canonically identified with the light field of the object:

$$I^{\zeta}(\chi, \eta) \quad = \quad I(x, y, z) \tag{2.24}$$

In the following, no explicit distinction between object coordinates (x, y, z) and real image coordinates (χ, η, ζ) is made.

2.1.3 Physical limitations

The holographic reconstruction of a wave field is ideally done with the exact complex conjugate of the wave field of the object on an infinitely large holographic medium with unlimited spatial resolution and a linear relation between interference pattern intensity and absorption (or index of refraction). In any physical realization, this can only be achieved approximately: The recording medium has a limited spatial resolution due to its finite grain size (silver halide material) or the discrete pixel spacing (digital CCD sensor). The recording medium is marginally non-linear and the actual reconstructed wave field differs slightly from the complex conjugate of the reference wave, in wave length or geometry. These deviations are due to imperfections of the reconstruction set-up and can be minimized by careful control of the experimental set-up. The limited hologram size does, however, restrict the resolution of the reconstructed wave field due to the diffraction limit. The following section discusses this effect.

In addition to this fundamental limit on the resolution, one must keep in mind that even with an ideal reconstruction wave field and hologram, the absence of the object in the real image volume causes the reconstructed wave field to differ from the exact complex conjugate of the wave field as the object causes no absorption or scattering. The missing absorption mainly[3] has the effect that the reconstructed light field does not stop in the surface points but protrudes into the volume of the object. A surface object point thus causes a real image intensity in front as well as behind its lateral position in the real image (Fig. 2.4).

Recording medium

To record an optical interference pattern, in general a medium with high spatial resolution is needed. Let us consider a simple hologram formed by the interference of two plane waves with amplitudes U_1 and U_2. The two wavenumber vectors $\mathbf{k}_1$,$\mathbf{k}_2$ have equal length. The interference intensity is

$$I \quad = \quad |E_1 + E_2|^2 \propto |e^{i(\mathbf{k}_1 \cdot \mathbf{x})} + e^{i(\mathbf{k}_2 \cdot \mathbf{x})}|^2. \tag{2.25}$$

[3]On a microscopic scale, the missing absorption furthermore causes minute deviations as the reconstructed wave field can not interact with the charges on the object surface. This is -per definition- a near-field effect and can be neglected for macroscopic surface topometry

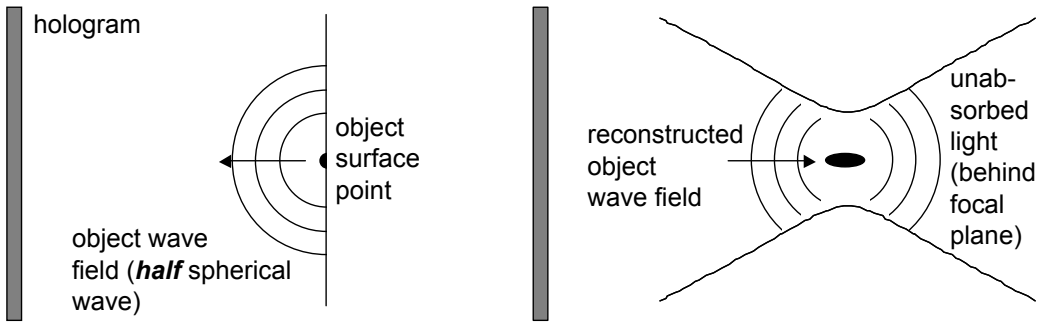

Figure 2.4: The reconstructed wave field (right) is the complex conjugate of the object wave field (left). The absence of absorption in the real image can cause deviations from the object wave field.

Without loss of generality, one can assume that $k_{1y} = k_{2y} = 0$ (for example by suitable rotation of the coordinate frame) and that the hologram plane has a normal vector $\vec{e}_z$ parallel to $\mathbf{k}_1 + \mathbf{k}_2$. In this case (Fig. 2.31), the x-components of the wavenumber vectors sum up to zero : $k_{1x} = -k_{2x}$. In the hologram plane $z = 0$ perpendicular to $n \perp e_z$, the interference pattern is then

$$I(x,y) = |e^{i(\mathbf{k}_1 \cdot \mathbf{x})} + e^{i(\mathbf{k}_2 \cdot \mathbf{x})}|^2 \tag{2.26}$$

$$= |e^{i(k_x \cdot x)} + e^{i(-k_x \cdot x)}|^2 \tag{2.27}$$

$$= 4\sin(k_x \cdot x)^2 \tag{2.28}$$

The interference pattern is then a sinusoidal fringe pattern with spacing Γ:

$$|\sin(k_x \cdot x)|^2 = 1 + \cos(\frac{\pi}{\Gamma} \cdot x) \tag{2.29}$$

$$\Gamma = \frac{\pi}{k_x} \tag{2.30}$$

$$= \frac{\pi}{|\vec{k}| \cdot \sin(\theta/2)} \tag{2.31}$$

when θ denotes the angle between $\mathbf{k}_1$ and $\mathbf{k}_2$. Thus, a hologram of a plane wave recorded with a plane reference wave is a sinusoidal grating. It is well-known that an incident plane wave is diffracted by a sinusoidal grating into a $+1$th and a -1th order plane wave which both satisfy the grating equation. In the terms of holography, those secondary waves are interpreted as virtual and real image of the object wave reconstructed by the reference wave respectively its complex conjugate. As the plane wave is self-conjugate, no distinction between real and virtual image can be made and they are reconstructed simultaneously.

To record a sinusoidal grating, the medium must be able to resolve the interference pattern. Photographic recording material is available with extraordinarily high spatial resolution. A CCD-chip, however, has a discrete pixel spacing Δ (the inverse of its spatial sampling rate) in the range of several micrometers: Commercially available CCD sensors, for example, have pixel sizes down to 2.5 μm. The pixel spacing must not exceed half of the period of the fringe spacing (Nyquist theorem [Nyq28]). If the interference pattern is recorded with a given pixel spacing and wave length, this means that the angle θ between reference and object wave must not exceed θ_{max} with

$$\theta_{max} = 2\arcsin\left(\frac{\Delta}{\lambda}\right) \tag{2.32}$$

In a set-up where the reference wave is a plane wave and the object wave is the scattered light from an object, only object waves with wavenumber vectors within a cone of opening angle θ_{max}

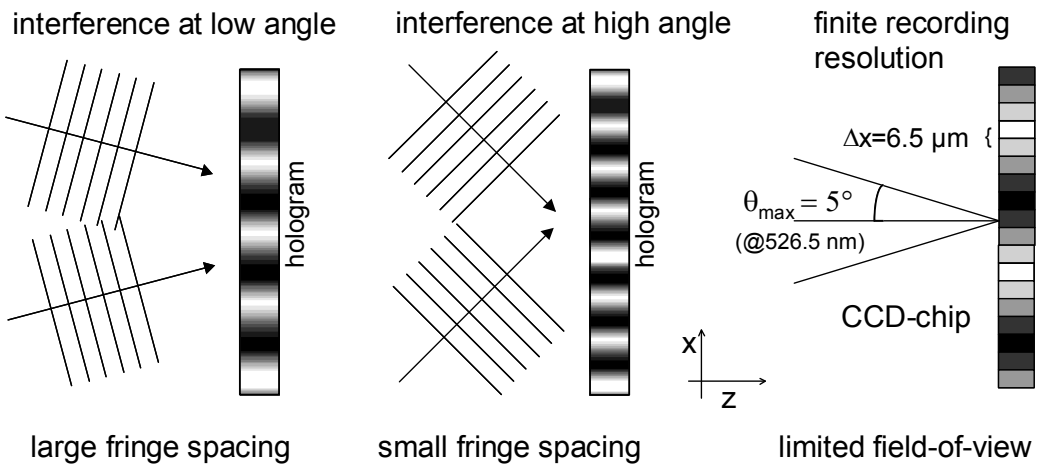

Figure 2.5: Interference fringe formation with two plane waves. With a finite detector resolution (right), only holograms formed by plane waves impinging under an angle of less than θ_{max} are recorded resolution

around the reference wavenumber vector contributes to the hologram. Other wave vectors cause aliasing on the CCD, i.e. a noise-like contribution to lower spatial frequencies. A reconstruction of the aliased components is not possible. Only objects which appear under an angle of less than θ_{max} (as seen from the hologram) can therefore be recorded. A finite resolution of the recording medium thus causes a limited field of view of the hologram (Fig. 2.5).

Historically, the low resolution of the recording material lead to the in-line geometry of the first hologram recordings. In the in-line geometry, the transmitted wave interferes with the scattered wave under a small angle, resulting in a large fringe spacing. Additionally, the path length difference for object and reference wave is small, allowing interference even with light sources of low temporal coherence. The main disadvantage of the in-line set up is that upon reconstruction, the real image, the virtual image and the 0th order overlap in the same volume. With the Leith-Upatnieks set-up, the reference beam impinges at an angle relatively to the view vector. Both 0th and the -1th order are thus separated spatially from the reconstructed object wave. The real image can therefore be measured in the absence of the other secondary waves.

Finite hologram size

The finite size of holograms limits the resolution of the reconstruction. Consider the hologram of a point source with a plane reference wave on an infinite hologram plane: The field of a point source at (x_0, y_0, z_0) is a spherical wave

$$U(x,y,z) = u_0 \frac{\exp(ik\rho)}{\rho} \tag{2.33}$$

$$\rho(x,y,z) = \sqrt{(x-x_0)^2 + (y-y_0)^2 + (z-z_0)^2} \tag{2.34}$$

where u_0 is a complex constant proportional to the amplitude of the point source. If the plane reference wave impinges with a k-vector parallel to the normal of the (ξ, η)-hologram plane, the intensity distribution of the interference pattern is

$$I(\xi,\eta) = |U+R|^2 \tag{2.35}$$

$$= |r_0 + u_0 \frac{\exp(ik\rho)}{\rho}|^2 \tag{2.36}$$

$$\rho(\xi,\eta) = \sqrt{z_0^2 + (\xi - x_0)^2 + (\eta - y_0)^2} \tag{2.37}$$

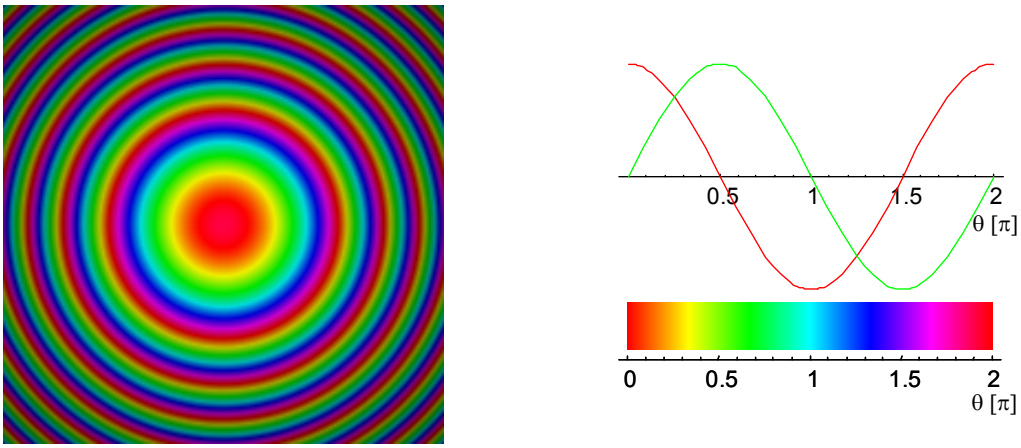

Figure 2.6: Complex amplitude of a Fresnel zone plate. The colour represents the phase, the brightness the magnitude of the amplitude.

The intensity constitutes a so-called Fresnel zone plate. It consists of concentric circles around (x_0, y_0) with decreasing radii (Fig. 2.6) and magnitude. Illumination of the hologram with the complex conjugate of the reference wave results in several secondary waves (2.1.1), including a halo as the magnitude of the object wave U^*U is not constant on the image plane. An identical reconstruction of the spherical wave is impossible as the reconstructions even from an infinite plane only contain plane waves traveling from the hologram plane towards the point source location. A decomposition of a spherical wave contains plane waves propagating towards or away from the holographic plane, and only the latter can be reconstructed. The real image thus resembles the spherical wave field only partially.

Furthermore, if the hologram size is finite, the resemblance of reconstructed and original wave field depends on the size of the hologram: This can be illustrated by placing a finite-sized diaphragm at the (infinite) hologram plane: One can obtain the reconstructed wave field of a finite hologram by calculation of the infinite holographic image diffraction due to he diaphragm. The finite-sized zone plate is interpreted as a thin lens with focus at the point source origin: Diffraction theory [BW01] predicts that the diffraction-limited size d of the focus of a (spherical) lens with aperture D is larger than

$$d \geq 1.22\frac{\lambda z_0}{D} \tag{2.38}$$

For example, an ideal point object at large (infinite) distance (i.e. quasi parallel rays) is imaged by a thin lens (f =50 mm) with an aperture of D =25 mm at a wavelength of 500 nm and at the focal distance into an Airy disc with a width (of the first intensity maximum) of

$$d \geq 1.22\frac{500\,\text{nm} \quad 50\,\text{nm}}{25\,\text{nm}} \tag{2.39}$$

$$\geq 1.22\,\mu\text{m} \tag{2.40}$$

due to the finite aperture size [BW01]. Similarly, the real image of the hologram of a point source, the Fresnel zone plate, causes a focus with a finite size inversely proportional to its aperture stop $f\# = z_0/D$ (Sec. 2.4.1) when z_0 is the distance between the object and D the lateral dimension of the hologram. Point sources at the same axial distance cannot be resolved in the real image if they are closer than their respective Airy discs: The lateral resolution of the real image is thus limited by the finite size of the hologram.

For the axial resolution, consider the wave field of a spherical wave. Bongartz [Bon02] showed that its real image is approximately a Gaussian beam. The width of the hologram D,

the Rayleigh length and waist of the reconstructed wave field z_R and w_0 are related to the wavelength λ and the distance of the point source z_0 via [Sie86]:

$$w_0 = \frac{2z_0\lambda}{\pi D} \tag{2.41}$$

$$z_R = \frac{4\lambda \cdot z_0^2}{\pi D^2} \tag{2.42}$$

The axial resolution of the real image is thus also limited by the size of the hologram: It is inversely proportional to the square of the aperture stop of the hologram.

Deviations of the reconstruction beam

For optical reconstruction, the complex conjugate of the object wave field illuminates the hologram. In an actual set-up, this means that a tailor-made optical system produces a wave field which matches the complex conjugate of the reference wave as close as possible. Although techniques exist for exact phase conjugation (for example stimulated Brillouin scattering), a good approximation of the complex conjugate reference wave is commonly produced with conventional optical elements (i.e. lenses and mirrors). Small deviations of the reconstruction beam from the actual complex conjugate of the reference beam result from differences from the actual complex conjugate of the reference wave. This applies to geometrical deviations and wavelength changes, characterized by the ratio μ of recording and reconstruction wave field.

$$\mu = \frac{\lambda_{replay}}{\lambda_{record}} \tag{2.43}$$

The influence of wavelength shift and geometrical deviations of the reconstruction beam is described in detail in many publications [Cha66] [Lat71]. In this thesis, deviations of μ from unity are neglected even though in the experimental realization, an actual value of $\mu = 1.0104$ is used (Sec. 3). As Bongartz argued [Bon02], for paraxial points this results in a linear lateral scaling which can easily be measured with holograms of gauge objects and compensated after hologram tomography. Fang and Hobson [FH98] conclude that for a wavelength shift ranging from $0.98 < \mu < 1.02$ the shift in the in focal plane (16 μm in a distance of 50 mm) is indeed in good agreement with the paraxial approximation.

2.1.4 Laser speckle

This section introduces the terminology of laser speckle which are used for high-contrast object illumination (Sec. 3.1) in hologram recording and form a source of noise in optical hologram reconstruction. By definition, a laser speckle light field is caused by superposition of many elementary waves with a random phase. The scattering on diffusor screens and on the objects surface itself can be modeled as a superposition of elementary wavelets with random phase. Laser speckle formation thus resembles optical hologram reconstruction: In both cases, a (reference) wave field undergoes a phase modulation in the diffusor screen or the holographic medium, respectively. Whereas the phase modulation is well-defined in holography, the diffusor screen ideally introduces a random phase relation. Whereas in holography, the object wave field is optically reproduced by appropriate manipulation of the phase of the reconstruction wave, in speckle projection the resulting speckle field has a statistical intensity distribution. This statistical intensity distribution has a high contrast at all distances and is hence favourable for structured object illumination (Sec. 2.3.2).

The random phase relation is described by an ensemble of wavelet superpositions. An individual ensemble member U is a particular superposition of N wavelets U_n, each with a

fixed phase factor θ_n:

$$U = \frac{1}{\sqrt{N}} \sum_{k=1}^{N} |U_k| \cdot \exp(i\theta_k) \tag{2.44}$$

The statistical properties of the speckle pattern can then be concluded from the ensemble average. For example, the ensemble average of the intensity $I = U^*U$ is in the ensembles average:

$$< I > = < U^*U > \tag{2.45}$$

$$= \frac{1}{N} \sum_{k=1}^{N} |U_k|^2 \tag{2.46}$$

This average intensity is -for example- the result of a measurement with an incoherent light source. Any measurement of a particular speckle field gives an intensity distribution $I_k = \langle U_k^* U_k \rangle$ containing a characteristic speckle pattern. Assuming that the relative phases θ_k are evenly distributed and the amplitudes of the wavelets are equal, Goodman [Goo75] calculates the probability density of the intensity to be

$$p(I) = \frac{1}{\pi \langle I \rangle} \exp\left(-\frac{I}{\langle I \rangle}\right) \tag{2.47}$$

This is the intensity distribution for an idealized system with contributions of many mutually independent superimposed sub-fields. Statistic properties of the speckle intensity distribution can be measured experimentally. To what degree the assumption of evenly distributed phases holds is determined by the contrast of a speckle pattern. For a completely random phase relation (i.e. an even distribution of phases), it equals unity:

$$C = \frac{\sigma_I}{\langle I \rangle} = 1 \tag{2.48}$$

A common set-up for speckle generation is a laser beam which is collimated into a diffusor screen. The rough surface of a diffusor screen causes the sub-fields to have a more or less statistically distributed relative phase. The larger the size of the illumination spot, the better the condition of the independence of the phases of the sub-fields is fulfilled, but any physical diffusor screen cannot produce phases with completely random phases. This means that the contrast of any physical speckle pattern is less than unity. To characterize speckle fields, one often measures the contrast and the coarseness of the speckle pattern. The coarseness is characterized by the average speckle size defined as the first minimum of the intensity autocorrelation function:

$$AC(\delta x, \delta y) = < (I(x,y) - < I >)(I(x+\delta x, y+\delta y) - < I >) \tag{2.49}$$

Here the ensemble average is interpreted as a spatial average over the area of a projection screen onto which the speckle field is projected, i.e. on the relative distance $(\delta x, \delta y)$ on the screen. To calculate the spatial structure of the laser speckle field, one can use the Rayleigh-Sommerfeld diffraction integral formalism over the focus spot size on the diffusor screen. Fomin [Fom98] deduces an autocorrelation function of

$$AC(\Delta x, \Delta y) = < I >^2 \left(1 + \mathrm{sinc}^2\left(\frac{2a_1}{\lambda z}\Delta x\right)\mathrm{sinc}^2\left(\frac{2a_2}{\lambda z}\Delta y\right)\right) \tag{2.50}$$

of a speckle field from an ideal, rectangular diffusor with dimensions $a_1 \times a_2$ at a distance z from the projection screen. The first minima of this autocorrelation are at

$$\delta_{1/2} = \pi \frac{\lambda z}{2a_{1/2}} \tag{2.51}$$

Even if the phases of the wavelets are not distributed evenly and independently, the first minima of the autocorrelation from a measured intensity distribution characterize the (average) speckle size (Sec. 4.1.3).

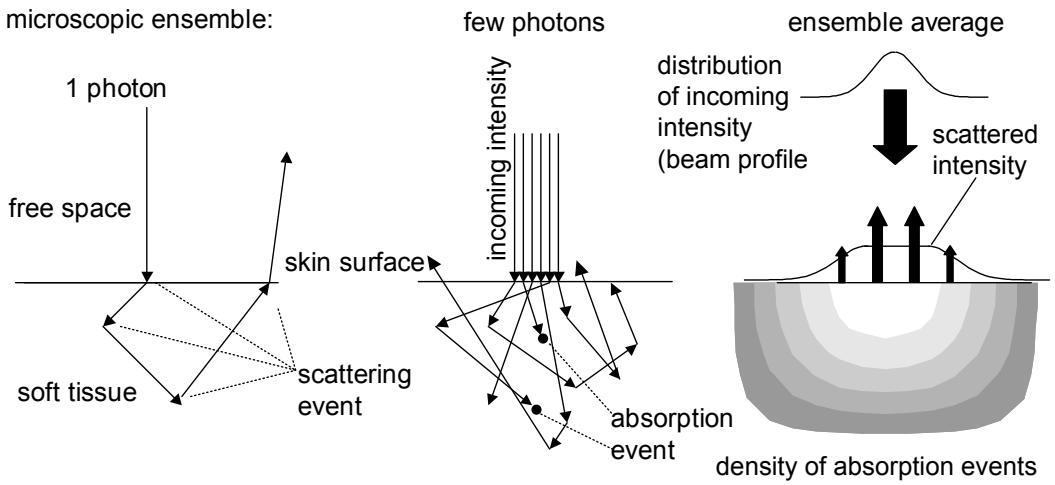

Figure 2.7: Random walk of photons models light propagation in scattering tissue. Left: individual microscopic ensemble, middle: superposition of few ensembles, right: ensemble average

2.1.5 Scattering properties of the human skin

With laser speckle projection, a high-contrast pattern can be projected onto an arbitrary surface. In medical applications, the surface considered is the human skin. The properties of human skin (absorption and propagation of light) are discussed in this section.

Recent advances in non-invasive tissue property measurement led to a quantitative description of the scattering parameters of the human skin and the tissue next to the skin surface. Optical absorption and scattering factors vary with the wavelength and the body part under consideration [LNS03]. The basic model used for those descriptions of the propagation of light is the random walk (Fig. 2.7): An ensemble of photons is modeled by an (angle-dependent) scattering probability function. Each ensemble member is a sequence of interactions of a photon with skin (absorption, scattering). The ensemble average describes the intensity distribution which results from irradiation with a large number of photons. The scattering probability function has two parameters for the strength of absorption (μ_a and μ_S) and an anisotropy factor g. As different skin regions have different optical properties, calculation of the ensemble average requires in general a numerical solution, for example by a Monte-Carlo-simulation, and a knowledge of the boundary conditions. The intensity distribution within a semi-infinite scattering and absorbing medium follows approximately a Lambert-Beer law, i.e. the intensity drops exponentially with distance from the surface. It is reduced to $1/e$-th of the surface value after a penetration depth δ. According to [Rog97], δ depends on μ_a, μ_s and g via

$$\delta = \frac{1}{\sqrt{3\mu_a(\mu_a + \mu_s(1-g))}} \qquad [\delta] = \text{m} \tag{2.52}$$

For 526.5 nm, Bongartz calculates a penetration depth of

$$\delta = 1.3\text{mm} \tag{2.53}$$

If one assumes isotropic scattering ($g = 0$) and surface effects are neglected, the intensity distribution in the tissue is also isotropic. In this case, the penetration depth δ describes the axial as well as the lateral intensity distribution if the skin surface is inhomogeneously lit. If, for example, the skin is illuminated with a beam with well-defined edge, the scattering causes the intensity distribution of the diffuse reflected light to smear out (Fig. 2.8). As the anisotropy factor is usually larger than zero (i.e. forward scattering is more probable), the lateral size of the projected intensity is lower than the axial penetration depth. This means that the blur of

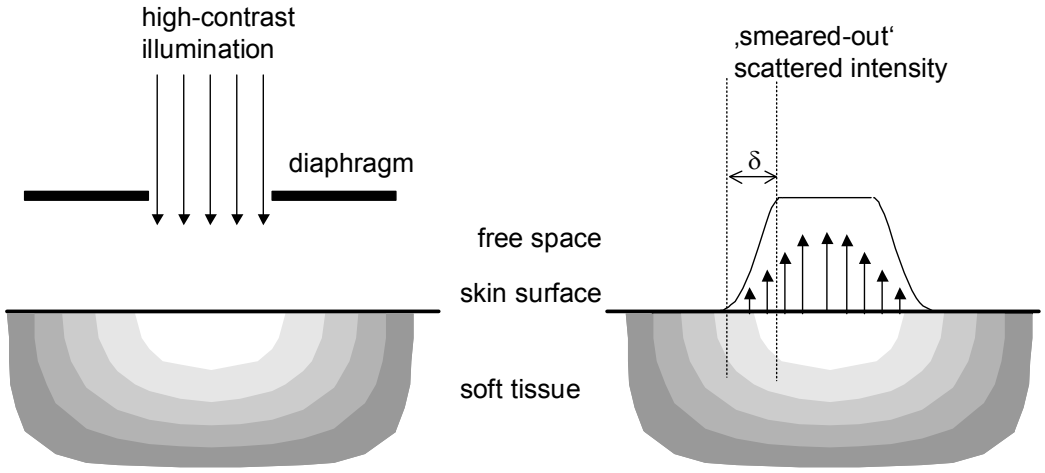

Figure 2.8: High-contrast illumination of human skin (left) is reflected smeared-out due to the diffusion of the light into the underlying tissue (right)

lateral projected patterns is actually smaller than the axial penetration depth. In this thesis, the smallest projectable speckle pattern is experimentally determined (Sec. 4.1.3).

2.2 Hologram deconvolution

In this section, the methods for numerical image deblurring are presented. First, the concept of the holographic point-spread-function (PSF) is introduced: The PSF is defined as the intensity distribution of a single, point-like object. The PSF is a function of two (for 2D images, for example in photography) or three (for 3D images like the holographic real image) spatial coordinates. The description of an imaging system by its PSF [Mah01] is commonly simplified by two additional assumptions: First, that the shape of the PSF is the same for all object points, i.e. that the PSF is invariant over the complete imaging range (translational invariance). Second, that the real image can be approximated as an incoherent superposition of intensities of the images of all object points. The 3D image is then related to the object function [GW93] by convolution with the point spread function $h(\delta x, \delta y, \delta z)$ of the imaging system:

$$I = h \otimes O \tag{2.54}$$

$$I(x,y,z) = \iiint h(\xi - x, y - \eta, z - \zeta) \cdot O(\xi, \eta, \zeta) d\xi d\eta d\zeta \tag{2.55}$$

Both assumptions are only partly met in holography: The scattered radiation of the object surface is a coherent superposition of the intensities from the individual object. In the case of a human face, however, the object surface scatters with a fixed, but quasi random phase (Sec. 4.1.3). The translational invariance is a good approximation for many imaging systems. For holography (and conventional microscopy), the PSF depends on the axial and lateral distance of the object. Off-axis points have slightly rotated cones, far object points have lower opening half-angles. To derive the holographic point spread function, the hologram of a point source is calculated in the following section.

2.2.1 Gaussian point-spread-function

Illumination of such a point-like object with a coherent wave results in a spherical wave originating at the position of the object. Let us consider a point on the optical axis $(x_0 = 0, y_0 = 0, z_0)$ at distance z_0 from the hologram plane. A hologram of this spherical object wave field with a planar reference wave is a Fresnel zone plate [BW01]. If one reconstructs the zone plate with a Gaussian beam, the object wave field is also a Gaussian beam [Bon02] with the waist at $(0, 0, z_0)$ and Rayleigh length and waist determined by the hologram size and the wave length. This intensity distribution is thus the incoherent point spread function of the holographic imaging system (Fig. 2.10):

$$h(x,y,z) = \left(\frac{w_0}{w(z - z_0)}\right)^2 \exp\left(-2\left(\frac{\rho}{w(z - z_0)}\right)^2\right) \tag{2.56}$$

$$w(z) = w_0 \sqrt{\left(1 + \left(\frac{z}{z_R}\right)^2\right)} \tag{2.57}$$

$$\rho^2 = x^2 + y^2 \tag{2.58}$$

Its far-field divergence

$$\tan(\Theta_{div}) = \lim_{z \to \infty} w(z)/z \tag{2.59}$$

equals the ratio of object distance and hologram radius $D/(2z_0)$. An arbitrary object function can be expanded into a superposition of point sources with individual phases (coherent superposition). With randomly scattering surfaces, however, the phase relation is arbitrary, i.e. the

real image intensity of an object does not depend significantly on the relative wavelet phases, and the real image can also be written as a incoherent superposition of point sources. This can be illustrated by the following gedankenexperiment: Two holograms of an object are recorded with homogeneous object illumination by two object beam diffusor screens. The exposures are made with identical parameters (pulse intensity, object distance, etc.) expect that both diffusor screens are interchanged for the second hologram. As the phase of the object illumination wave field determines the actual relative wavelet phases of the object wave field, both holograms are recorded with different sets of wavelet phases. This situation has its analogy in a photography of an object with coherent light. High coherence of the object illumination results in laser speckle noise. Two photographs of an object show different laser speckle patterns if the relative wavelet phases changed in between exposures. However, they can still be attributed to the same object. Similarly, both hologram reconstructions of the gedankenexperiment are approximately identical. The incoherent sum can thus be seen as a good approximation if the relative wavelet phases of the object wave field are pseudo-random and the formalism of the incoherent PSF can be used.

2.2.2 Numerical image deblurring

In hologram tomography, one is interested in finding the object function $O(x, y, z)$ based on the knowledge of the real image $I(x, y, z)$. A similar problem occurs in microscopy where only the image intensity from points of a certain plane, the focal plane, are imaged sharply. Other out-of-focus parts of the object contribute to the total intensity in the image plane, but appear blurred. In photography, the limited depth of field causes partially unsharp images. A well-known method to reduce out-of-focus is numerical image deblurring which is described in the this section. To illustrate the general idea of deblurring, one can write the convolution integral 2.55 as a multiplication in Fourier space:

$$I(x, y, z) = h(\xi - x, y - \eta, z - \zeta) \otimes O(\xi, \eta, \zeta) \tag{2.60}$$

$$\mathsf{FT}[I] = \mathsf{FT}[h] \cdot \mathsf{FT}[O] \tag{2.61}$$

This leads to a representation of the object function by:

$$O = \mathsf{FT}^{-1}\left[\frac{\mathsf{FT}[I]}{\mathsf{FT}[h]}\right] \tag{2.62}$$

For the one-dimensional case, an example of the convolution is depicted in Fig. 2.9: The object function O is a step-function, the point-spread-function h a Gaussian curve. The Fourier transform of the object function is a 'sinc' (i.e. $\frac{\sin(x)}{x}$) function. The Fourier transform of the PSF is a Gaussian. In Fourier space, multiplication of a Gaussian and a 'sinc' yields a curve with a single peak and an infinite number of additional local maxima and zero crossings. By inverse Fourier transformation, one gets the convolution in object space which, in this example, resembles a rectangular pulse with smoothed edges.

In practical applications, the calculation of the convolution integral as a multiplication in Fourier space can lead to a faster computation (Sec. 3.4.2).

Properties of the holographic point-spread-function

Equation 2.62 allows a straight-forward calculation of $O(x, y, z)$ if the right-hand side of the last line was well defined, i.e. if $\mathsf{FT}[h]$ was non-zero for all spatial frequencies. However, the Fourier transform of the point-spread-function $\mathsf{FT}[h]$ (also known as the optical transfer function OTF) of most imaging system has zero crossings. The OTF describes how strong a

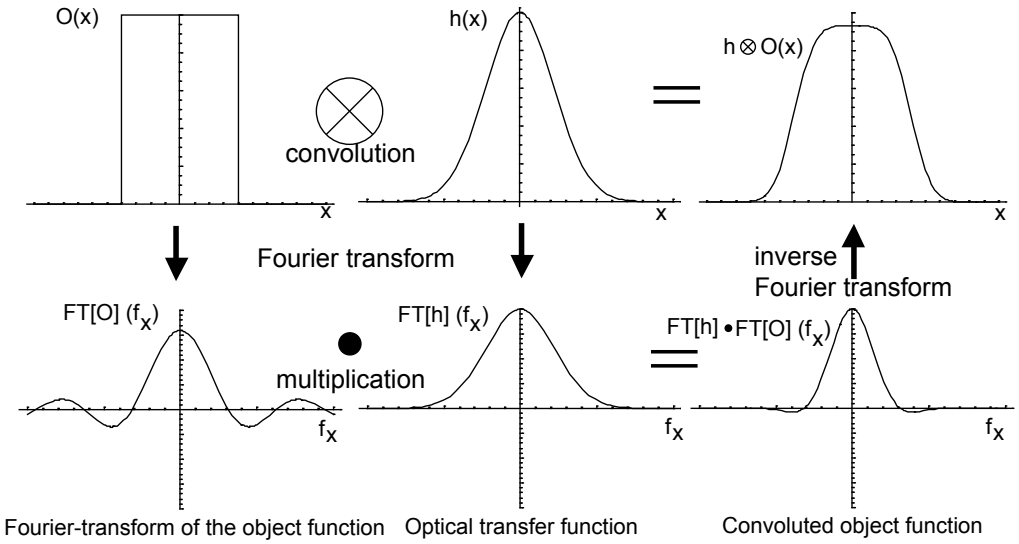

Figure 2.9: Convolution of a Gaussian peak (middle) with a rectangular point-spread function (left) in object space (above) and in Fourier space (below)

certain spatial frequency of the object function is transmitted by an imaging system. In the one-dimensional example, the OTF of the rectangular PSF has zeros and thus the inversion formula of equation 2.62 is ill-defined. The OTF of the holographic point-spread function (Eqn. 2.56) is defined through the triple Fourier integral

$$\mathsf{FT}[h(x,y,z)] \;=\; \frac{1}{(2\pi)^{3/2}} \iiint_{-\infty}^{+\infty} \frac{w_0^2}{w(z)^2} e^{-2\frac{x^2+y^2}{w(z)^2}} e^{\imath(f_x\cdot x + f_y\cdot y + f_z\cdot z)} dx dy dz \qquad (2.63)$$

The dx and dy integrations can be performed directly: With the substitution (see [BS91], p.622)

$$\mathsf{FT}[e^{-ax^2}] \;=\; \frac{1}{(2\pi)^{1/2}} \int_{-\infty}^{+\infty} e^{-ax^2} e^{\imath f_x x} \qquad (2.64)$$

$$\;=\; \frac{1}{(2a)^{1/2}} e^{-\frac{f_x^2}{4a}} \qquad (2.65)$$

one gets

$$\mathsf{FT}[h(x,y,z)] \;=\; c \int_{-\infty}^{+\infty} e^{-\frac{1}{2}\left(f_x^2+f_y^2\right)\cdot(1+z^2)} e^{\imath f_z\cdot z} dz \qquad (2.66)$$

with a constant factor c. The remaining dz integration can be carried out after separation of e^{-z^2} by the same formula. Defining the lateral spatial frequency f_ρ

$$f_\rho^2 \;:=\; f_x^2 + f_y^2 \qquad (2.67)$$

the complete OTF now reads

$$\mathsf{FT}\,[h]\,(f_\rho, f_z) \;=\; \frac{z_R}{2f_\rho^2} e^{-\left(\left(w_0^2 f_r^2\right)+2\frac{f_z^2 z_R^2}{w_0^2 f_r^2}\right)} \qquad (2.68)$$

The magnitude of $\mathsf{FT}\,[h]\,(f_\rho, f_z)$ is depicted in Fig. 2.10. It is never actually zero. It approaches, however, zero rapidly for certain frequencies. A contour plot of the magnitude of the

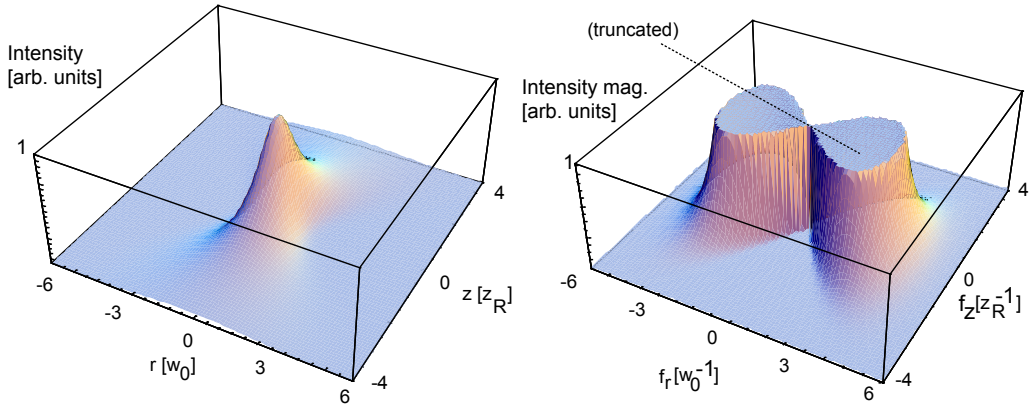

Figure 2.10: Incoherent holographic point-spread-function (left) and the magnitude of the corresponding optical transfer function (right)

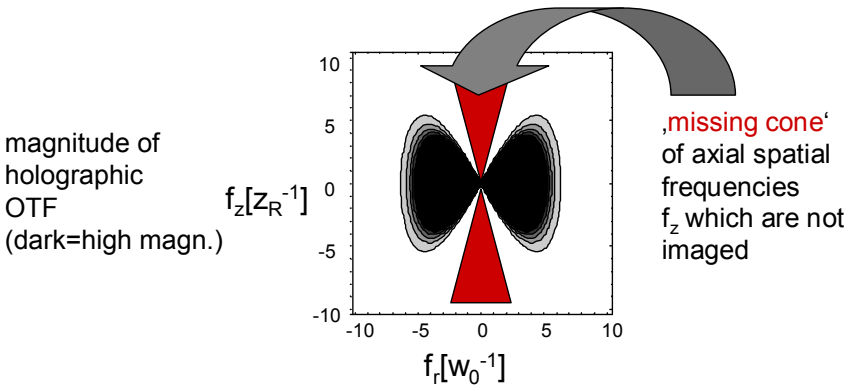

Figure 2.11: Contour plot of the holographic OTF: Light regions represent small values. Frequencies within the missing cone (red) are strongly attenuated

OTF (Fig. 2.11) reveals that spatial frequencies within a so-called *missing cone* are strongly attenuated by the holographic imaging system. This is critical as the cone extends down to the origin since no lower bound exists for the transmitted axial frequencies. At $f_r = 0$, no axial object features are transmitted. High uncertainties in axial object reconstructions can arise if object features with a low axial frequencies are lost.

The missing cone of spatial frequencies is inherent to a number of imaging systems, for example a conventional camera: Consider setting the focus of a camera on an object with no lateral features, for example a plain white sheet of paper. It is impossible to determine the proper distance and set the correct focal distance on such an object. In photography where the image blur is the only concern, this is not a problem: if there are no object features, one cannot image them blurred. For topometric measurements on the 3D image, however, the axial position of a homogeneous plane cannot be determined from its real holographic image as a direct consequence of the missing cone of non-imaged axial spatial frequencies. The axial spatial frequencies of the object function are lost in the image formation: There is no way of retrieving them from the image. One can show that $O(x, y, z)$ is, however, uniquely determined by $I(x, y, z)$ if the point-spread-function is non-negative (which is trivial) and I has compact support [Con95]. A function has compact support if it is zero outside some finite interval. The assumption of compact support thus means that one can only deconvolute objects surrounded by regions with $O = 0$. In this case, one can iteratively approximate the object function by subsequent simulations of the imaging process. An algorithm described by Conchello [Con95] converges on a suitable $O(x, y, z)$ for any given $I(x, y, z)$. The iteration starts with an initial guess $O^{i=0}$. One can, for example chose $O^0 = const.$

A different technique from three-dimensional microscopy is inverse filtering. Unlike iterative deconvolution, it cannot restore spatial frequencies lost in the imaging process [GW93]. It can, however, reduce the intensities from out-of-focus regions and contribute to a sharper image if the lateral image has enough features with high spatial frequencies. In conjunction with structured illumination, inverse filtering can significantly reduce the out-of-focus intensities. As for iterative deconvolution, the point-spread-function of the imaging system has to be known for inverse filtering. The algorithms used for inverse filtering and iterative deconvolution are described in detail in the experimental chapter (Sec. 3.4) together with their implementations.

For an object which comprises reflecting surfaces, the scattered intensity cannot be written as an incoherent superposition similarly to diffuse scattering: The wave field reflected by a plane mirror, for example, can not be approximated by the sum of the intensities at the mirror surface. The mirror constructs a virtual image of its environment. All objects in front of the mirror surface appear twice in the reconstructed holographic image, whereas the mirror surface is not imaged according to the PSF formalism. This allows one to use mirrors in the set-up to record multiple copies of the object wave field: The mirror surface is not represented in the hologram, but the virtual image of the object is recorded. The mirror recording technique is described in section 2.4.3.

2.3 Semi-heuristic surface reconstruction

In this section, an improved algorithm for surface localization based on a real image hologram tomography is presented. The algorithm uses semi-heuristic surface finding, a technique with roots in the field of pattern recognition. The term semi-heuristic implies that one cannot prove the mathematically rigid reconstruction of an arbitrary surface. From a practical point of view, however, the maximum sharpness concept operates well in numerous applications like active auto-focus cameras and automated microscopy [LC82] on surfaces. This section discusses the anisotropy of the previously introduced sharpness algorithm [Bon02] and improves it by the weighted neighbourhood concept.

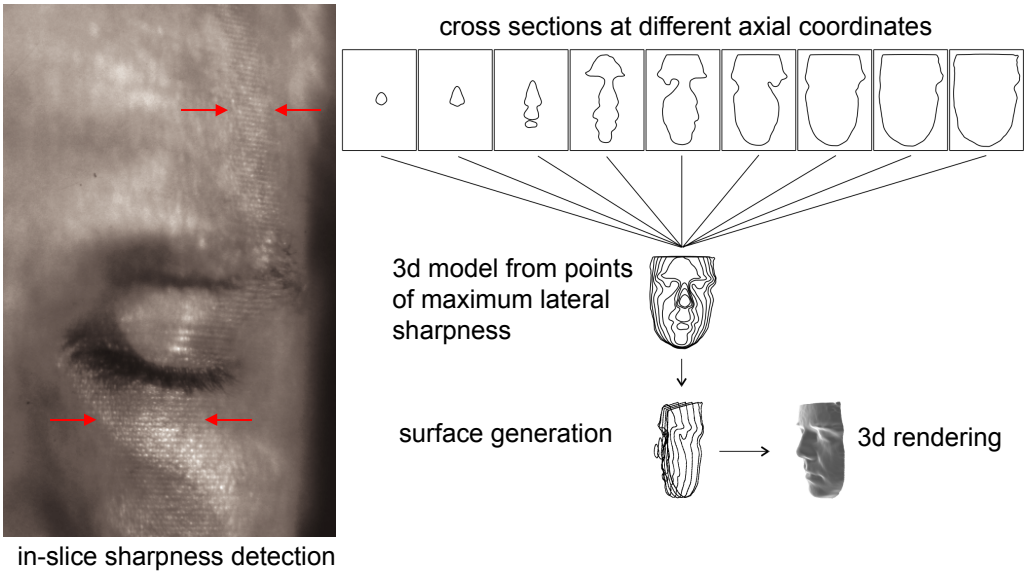

Figure 2.12: Detection of regions of high lateral contrast (left) allows semi-heuristic assignment of axial coordinates and yields to a closed surface model (right). Source: [Bon02]

2.3.1 Maximum sharpness

This semi-heuristic algorithm for surface reconstruction (Fig. 2.12) by hologram tomography has been introduced by Giel, Bongartz and Hering [GBH02] and is described in detail in the PhD thesis of Bongartz [Bon02]. The real image intensity distribution $I(\xi, \eta, \zeta)$ is determined by hologram tomography: The real image is projected onto a diffusor screen and the intensity distribution $I^{\zeta}(\xi, \eta)$ on the screen is digitized where I^{ζ} denotes the projection of the three-dimensional real image at distance ζ. These projections are called slices of the real image (3.3).

Any particular slice I^{ζ} can be thought of as a superposition from the real image of object points with axial distance z equal to the distance $z = \zeta$ of the slice and intensity from the real image of points in front or behind the distance $\zeta > z, \zeta < z$ of the slice. The latter object points appear blurred or defocused in this particular slice. To distinguish between focused and defocused features in the slices, one assumes that the object under consideration has sufficiently high contrast. This can be ensured by a suitable object beam (Sec. 2.3.2), for example with laser speckle projection. Consider the real image of a single object point $P = (x, y, z)$. The slice I^{ζ} of the real image with $\zeta = z$ is a sharply focused projection of the object field. Slices with $\zeta \neq z$ contain a blurred image of this slice. The sharpness at lateral position (ξ, η) of all slices reaches its maximum at $z = \zeta$. The axial distance this object point equals the distance of the slice with maximum sharpness at $(\xi = x, \eta = y)$. In this context, the term sharpness has no generic definition. For a quantitative analysis, different measures $f_{(\xi,\eta)}(\zeta)$ are described in literature [LC82]. They assign a positive number, a so-called figure-of-merit, to any lateral position (ξ, η) on all slices ζ to quantify the sharpness. The peak value of $f_{\xi,\eta}(\zeta)$ is then interpreted as the location of the surface in the real image. It is obvious that in this way, one can describe only simple surfaces $z = z(x, y)$ called relief surfaces. For many medical applications, this representation gives sufficient information. Otherwise, several reliefs from different perspectives have to be recorded (Sec. 3.1.2)

As a single image point has no sharpness by itself, all measures interpret the intensity distribution around (ξ, η) to quantify the sharpness (Fig. 2.14). If the intensity of the real image is given in a discrete pixel representation, this means that one calculates the sharpness of a pixel (ξ_0, η_0) from the intensity of a number of adjacent pixels of this slice. This pixel subset is referred to as the neighbourhood of pixel (ξ_0, η_0). Bongartz calculated the variance of the

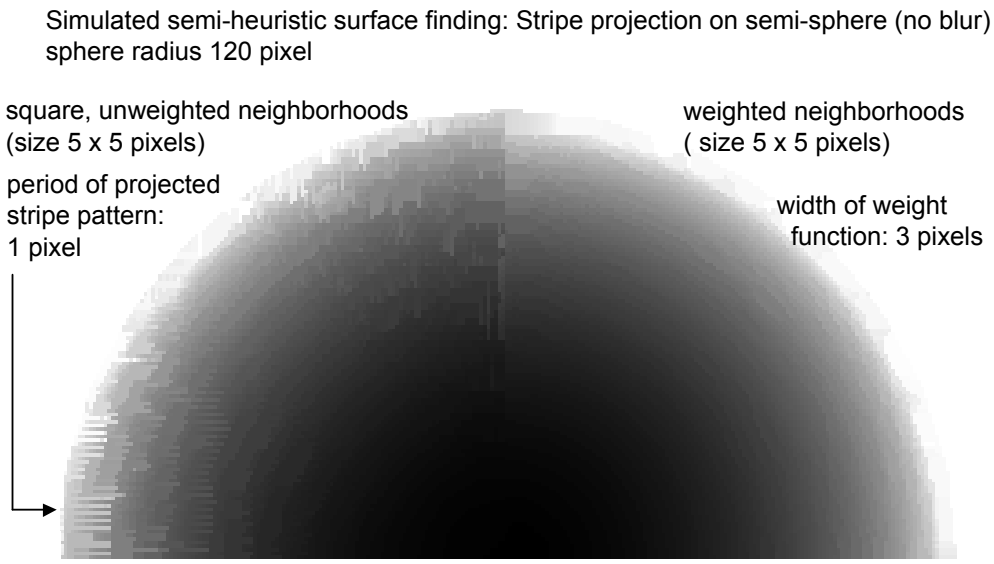

Figure 2.13: Grey-coded relief map from a simulated hologram tomography of a semi-sphere (Fig. A.3) of radius 120 pixel with a stripe projection with a period of 1 pixel. The reconstruction was made with (right) and without (left) weighted neighbourhoods.

intensity on square neighbourhoods of size 3×3, 5×5 or 7×7 as a measure of sharpness of the central pixels. As all pixels in a square neighbourhood of side length a contribute equally to the sharpness measure of the central pixel, artifacts can arise (Fig. 2.13) in the reconstructed relief surface. They resemble the neighbourhood shape or the pattern projected onto the surface and are referred to as square artifacts. In a square neighbourhood, the most distant pixels are the diagonal pixels with a distance of $\sqrt{2}a/2$. The pixels at the edges parallel to the side of the square are at a distance of $a/2$ whereas the closest pixel have a distance of only one pixel period (at least $a/3$). To avoid this anisotropy, the concept of weighted neighbourhoods is used: Each pixel of the neighbourhood is assigned a relative weight according to its distance to the central pixel. The weight function $w(r)$ is a monotone function with $\lim_{r\to\pm\infty} w(r) = 0$ and $\sum_{(\xi,\eta)\in N} w(\sqrt{\xi^2+\eta^2}) = 1$. The sharpness measure is calculated with each pixel contributing according to its weight. For example the variance of the n pixels in the neighbourhood N

$$f_v = \frac{1}{n} \sum_{(\xi,\eta)\in N} (I_{(\xi,\eta)} - \mu)^2 \tag{2.69}$$

$$\mu = \frac{1}{n} \sum_{(\xi,\eta)\in N} I_{\xi,\eta} \tag{2.70}$$

is replaced by the weighted variance

$$f_{wv} = \frac{1}{n} \sum_{\xi,\eta\in N} w(\sqrt{\xi^2+\eta^2})(I_{(\xi,\eta)} - \mu)^2 \tag{2.71}$$

Similar functions are used in the Fourier-analysis of non-periodic signals where a faltung with a window function is applied to the signal prior to transformation. The literature on suitable window functions for particular applications is abundant. In this thesis, normal distributions were used as weight functions. They are parameterized only by one parameter, their standard deviation, and allow an efficient summation.

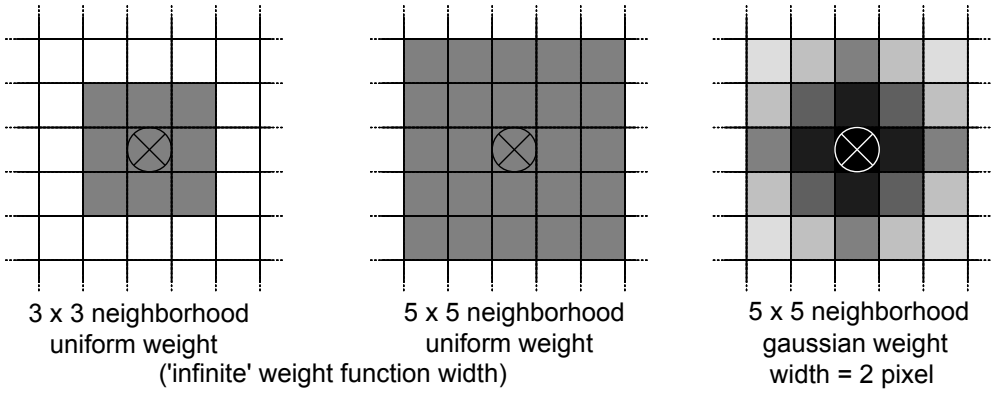

Figure 2.14: Weighted neighbourhoods (right) augment the influence of the nearest neighbors. Constant weights (middle, left) cause square artifacts

2.3.2 Structured light

The idea of increasing the axial resolution of imaging systems by structured illumination is well established: In active photogrammetry and fringe projection, additional depth information is gained by modulation of the illumination. By structured object illumination in holography, a high-contrast pattern is projected onto the object surface which allows an improved surface detection with the figure-of-merit sharpness determination. As a drawback, the lateral resolution is lowered by the structured illumination: Two objects at a lateral distance below the period of the structured illumination might appear as one as higher axial spatial frequencies are cut off by the imaging system. Bongartz [Bon02] showed that with the Talbot effect, high-contrast projections of a stripe pattern can be achieved for a certain interval of distances. To overcome the problem of low-contrast projections at the other distances, a statistical laser speckle pattern has been used for contrast enhancement in the present work.

In terms of the spatial frequencies of the object function, structured illumination modulates the low lateral frequencies: In Fig. 2.11, this means that the lateral spatial frequencies of the object have a lower bound. The extension of the missing cone down to the origin is thus no longer a problem since no object information is transmitted in this region. As a draw-back, the image contains no information on the object at lateral spatial frequencies higher than the modulation frequency of the illumination. This constitutes a trade-of between unambiguous determination of the axial distance and the lateral resolution.

2.4 Hologram perspective

In this section, the perspective of holograms is discussed and a technique for perspective-based topometry is presented.

The term perspective describes a mathematical concept which *"models how images change with the position, the distance and other parameters of the imaging device"* [Pau99]. The term is commonly used for two-dimensional images of three-dimensional objects. For three-dimensional images of three-dimensional objects (holographic real images), it can be used in a generalized way. By definition, the perspective of an image contains information on the location of an object. With two-dimensional imaging, the projection of a three-dimensional object into the image plane can be modeled by the camera matrix formalism (Appendix A). It determines the position of the image of a certain object point depending on the cameras focal length, position and orientation. The use of perspective for topometric measurements is, however, hindered by the ambiguousness of a single 2D image for range measurements. In this sense, holograms are an ideal imaging system for the use of perspective : The holographic

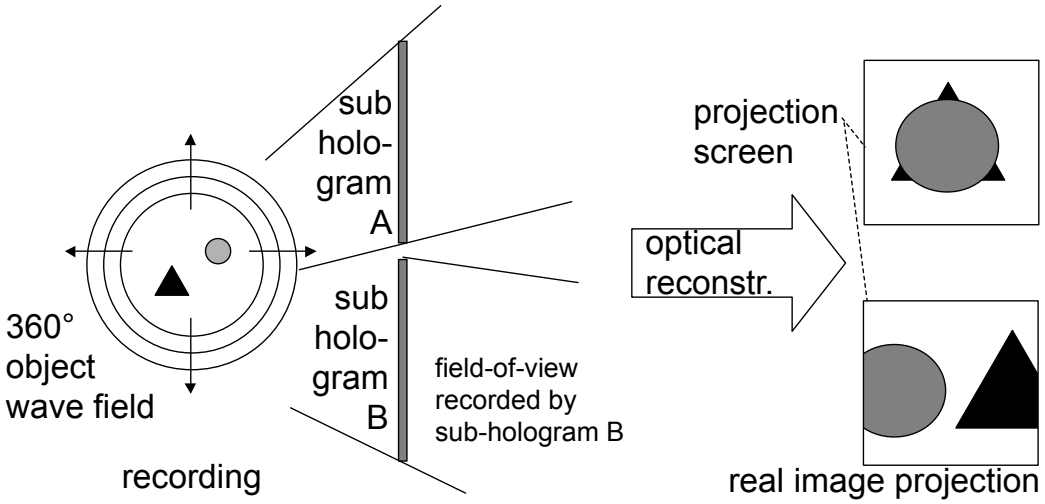

Figure 2.15: Real image hologram reconstruction of a scene with two objects. The perspective of hologram A (B) reconstructs the circular object in front (next to) the triangular object

real image contains the complete wave field information, it can be reconstructed statically for infinite periods of time and there is a 1:1 correspondence between image and object. In contrast, conventional photogrammetry cameras need extensive calibration for topometry [FLM92].

The reconstructed wave field of the object is identical to the original wave field if the hologram is ideal in the sense that it is reconstructed from a finite, closed surface around the object (apart from absorption of radiation which is not present in the reconstructed image if the object is removed). The real image has no perspective in this case- it is an exact copy of the object wave field and does not depend on any parameter of the imaging system. If, however, the hologram has a finite size, the object wave field can only be reconstructed approximately. Fig. 2.15 shows a simple scene with two objects (circle and triangle) recorded on two planar holograms. The reconstructions have a limited lateral and axial resolution according to equation 2.42. Additionally, in the real image projections obtained from hologram A, the circle appears in front of the the triangle and partly occludes it. In contrast, the real image projections from hologram B shows both objects next to each other. If one combines both holograms to a single hologram, the real image would be a superposition of the individual real images- the different lateral positions of circle and triangle would result in a blur of the joint image: For the axial distances corresponding the distance of the circle, the triangle would appear blurred.

A wave field reconstruction from a finite hologram has projections with a finite depth of field. The projection of intensity from points near or at the screen position appears sharp, the real image intensity from object points at a distance (out-of-focus points) blurred. From the evaluation of the sharpness, the real image thus can be assigned a certain axial resolution: Projections with a high depth of field correspond to a real image with low axial resolution whereas a low depth-of-field means that sharp and unsharp real image points can be distinguished with a high axial resolution. In contrast, to the determination of the resolution in terms of sharpness, the following sections deduce the axial distance from hologram perspective. Perspective from hologram reconstructions can either be achieved from planar holograms by masking the hologram partly (aperture masking, sec. 2.4.1) or with a mirror recording set-up (Sec. 2.4.3). Surface reconstruction based on the combination of several perspective holograms obtained with aperture masking is described in section 2.4.2.

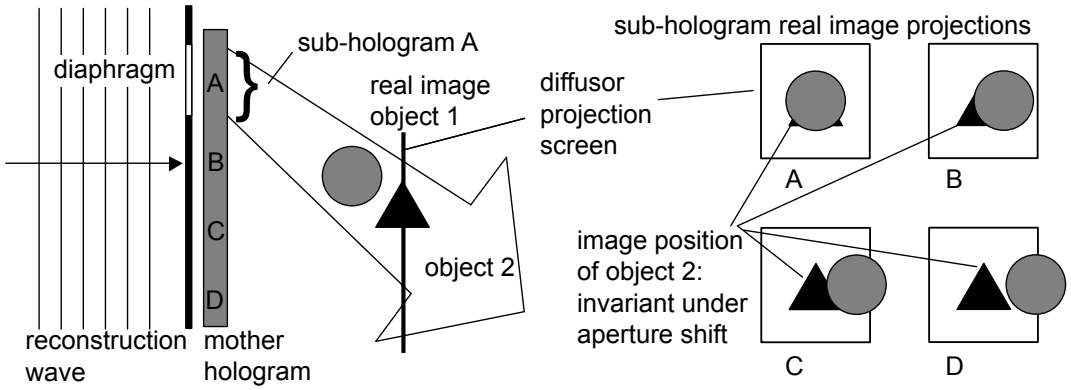

Figure 2.16: Masking a planar mother hologram to generate real images from sub-hologram A,B,C,D with different perspective. The lateral position of object 2 is aperture-shift invariant

2.4.1 Perspective by hologram masking

In this section, a technique to extract real images with a certain perspective from conventional planar holograms is presented. The main purpose of generating several real images from a planar hologram is the different perspective of the resulting real image projections. As a draw-back, the resolution of the individual real images is reduced. In comparison to existing topometry techniques, multi-perspective from planar holograms can be compared to a triangulation of an object from several different camera views from different locations. In holography, a virtually infinite number of perspectives can be deduced from a single holographic exposure by simply shifting the aperture which masks the hologram plane- with conventional imaging systems, this would require multiple cameras or a completely static object.

Aperture stop of holograms

By placing an aperture directly at the hologram plane, the hologram can be reconstructed partially. This can be realized by placing the aperture in the reconstruction beam before it reaches the hologram plane (in front of the hologram) or behind the hologram. In the first case, the reconstruction beam is diffracted by the aperture, whereas in the second case, the real image is superimposed by secondary diffracted waves from the aperture. If the aperture size is large compared to the wavelength, the effects of those secondary waves can be neglected. In this thesis, only the changes in waist and Rayleigh length of the real image are considered whereas the wave field of the secondary waves caused by the aperture are neglected. By variation of the diaphragm size, the effective hologram diameter is changed. The real image perspective and the depth of field of the real image projections (i.e. the slices) are defined by the illuminated part of the hologram. In photographic imaging, this area corresponds to the lens aperture. By analogy, the f# (the aperture stop) of a hologram is the quotient of object distance over aperture diameter for holograms (Fig. 2.16). It determines the opening angle of the point spread function, i.e. how wide the image of a point source spreads when it is projected onto a screen at a certain out-of-focus plane. As in photographic cameras, the aperture stop of the hologram can be varied by an appropriate diaphragm. Masking different parts of the hologram provides real images corresponding views from different positions (real images with perspective) onto the image. The real image resembles the object as photographed by a conventional camera at the central point of the masking aperture. The depth of field corresponds to a conventional camera with the same lens aperture. From a single, planar hologram, multiple perspectives at lower axial (and lateral) resolution are obtained. The maximum obtainable angle between the view vectors of the perspectives is limited by the extension of the hologram. The different perspective holo-

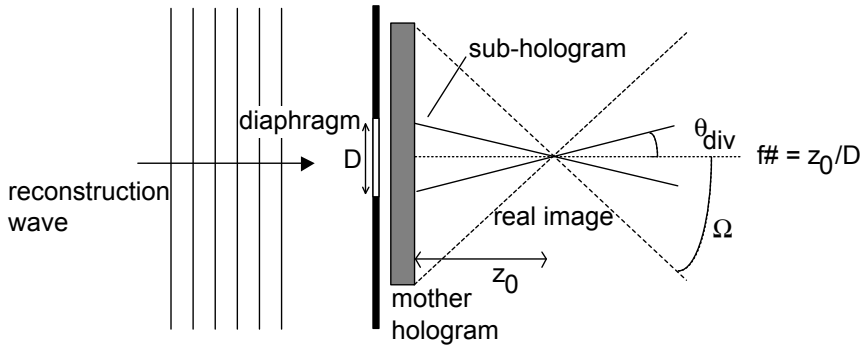

Figure 2.17: The aperture stop f# of a hologram is defined by the solid angle the hologram area covers as seen from the object

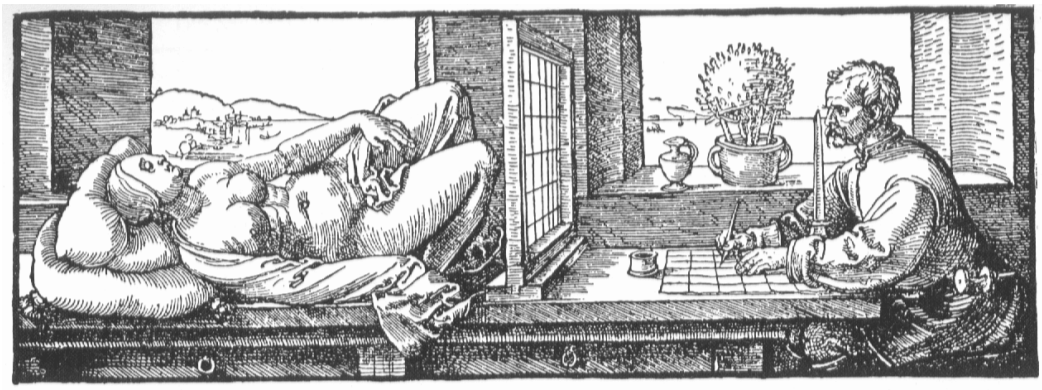

Figure 2.18: Using perspective for surface topometry in the arts. Source:[Dür00]

grams are referred to as sub-holograms of the planar mother hologram used for their generation (Fig. 2.17). The centre of the sub-hologram defines the view vector on the object. The distance between two sub-holograms on the hologram plane, the aperture shift, corresponds to a certain angle of the view vector.

2.4.2 MUPEGA (Multi perspective gradient averaging)

In the arts, the use of perspective has a long history which can be traced back at least to the sixteenth century: In his works on measurements [Dür00], A. Dürer describes a technique to achieve a certain perspective in drawings (Fig. 2.18): The artist aims at his model from a fixed point (by placing his eye behind the tip of a pyramidal rod) and sees the features of the object in the discrete raster coordinates of a semi-transparent screen. He then can depict each feature in the correct corresponding grid on his painting. For hologram tomography, the model is replaced by a portrait hologram, the raster screen by the projection screen, the artist by the CCD camera, and different perspectives are generated by the technique of aperture shifting. A property of the real image is used for multiple-perspective gradient averaging (MUPEGA): The invariance of the projections of in-focal real image projections on the placement of an aperture at the hologram plane. The aperture partly occludes the mother hologram, thus generating different sub-holograms. As in semi-heuristic surface detection, the real image of each sub-hologram is projected on a diffusor screen at a fixed distance to capture a slice of the real image. For each slice, the lateral position of the projection of in-focal points does not depend on the particular position of the aperture (Fig. 2.19). Contrary, the out-of-focal projections of real image points

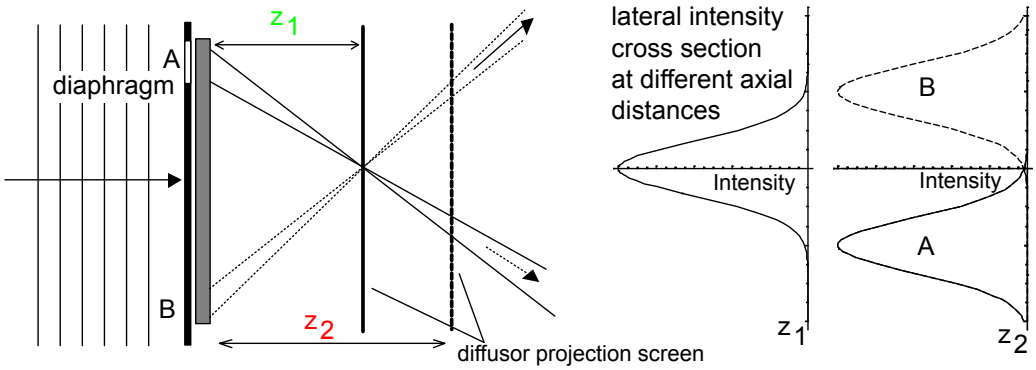

Figure 2.19: The lateral position of real image projection from in-focus points (green) are invariant over aperture shift, out-of focus points (red) move under aperture shift

move under shift of the aperture. Neglecting coherence effects, the real image intensity of the mother hologram can be written as a sum of the real images of a set of sub-holograms when the sub-holograms represent a decomposition of the mother hologram. Instead of adding the real image intensities - the numerical equivalent of illumination of the complete mother hologram - the average lateral image gradient vector $\langle (d/dx, d/dy) \rangle$ is calculated numerically after digitalization of the real image projection for each perspective. In this context, the brackets indicate averaging over all sub-holograms. The gradient derived from in-focus object points is constant for all sub-holograms, whereas out-of-focus features are projected onto a number of different lateral coordinates on the screen. The average lateral image gradient from out-of-focus components is thus reduced. This is illustrated for a one-dimensional Gaussian intensity distribution, the cross-section of the real image of a point source. The lateral gradient of the one-dimensional Gaussian intensity distribution with peak at ξ and minimum width at $z = \zeta$ is proportional to

$$\frac{d}{dx} I \quad \propto \quad -(x-\xi) \exp\left(-2 \left(\frac{(x-\xi)}{w(z-\zeta)} \right)^2 \right) \qquad [dI/dx] = [I]/\mathrm{m} \tag{2.72}$$

and has positive and negative maxima at $x = \xi \pm w/2$. For projections of the real image at out-of-focus distances, the actual value of ξ depends on the perspective- the lateral position of the real image varies under aperture shift for out-of-focus projections whereas for in-focus projections, the lateral shift of the real image due to aperture shift is zero. To illustrate this, the sum and the individual intensities of the real image of two and five overlapping peaks as been plotted for an out-of-focus projection in Fig. 2.21 and for the in-focus projection ($\xi = 0$) in Fig. 2.20 for two overlapping peaks. For $\xi = 0$, the average intensity simply equals twice the individual peak (Fig. 2.20). Now consider calculating the average lateral gradient instead of the intensity sum as depicted in Fig. 2.21 for an out-of-focus distance. Each of the sub-hologram real image intensity projections has a different lateral location on the diffusor screen. The lateral gradient, i.e. the spatial derivative of the projected intensity within the projection screen plane, has a maximum and a minimum. The positive and the negative maxima of two adjacent curves overlap: Except for the first and last maximum (the boundary peaks), the sum of the gradient magnitude is thus averaged out by the addition of positive and negative gradients. With a projection onto an in-focus screen, the average gradient is the same as each of the sub-gradients. The magnitude of the average gradient is reduced further by adding more curves with a smaller shift. The gradient sum has two boundary peaks which stem from the absence of neighbors for the first and last intensity peak. If those boundary peaks are eliminated, for example by arrangement of the one-dimensional intensity peaks on a closed, two-dimensional

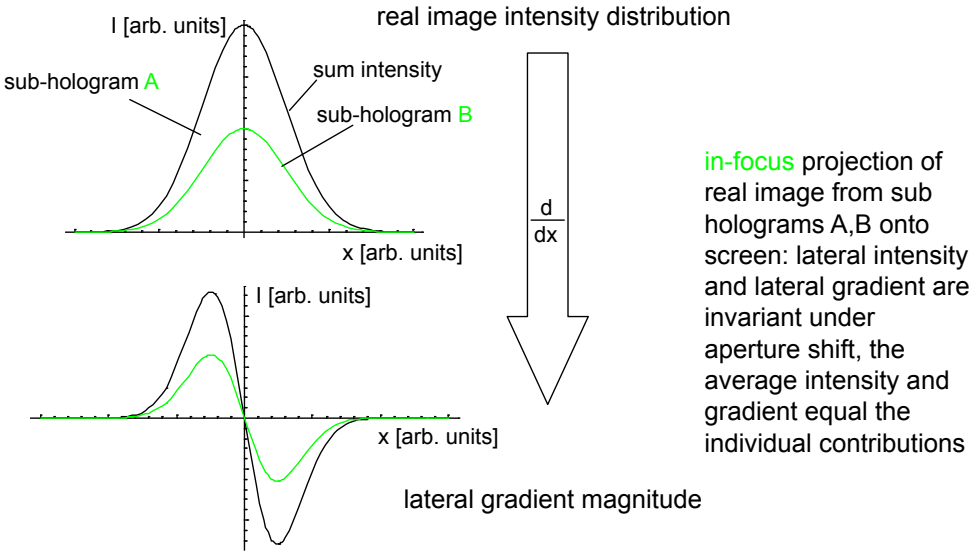

Figure 2.20: Real image intensities and lateral gradients from sub-holograms A and B projected onto a diffusor screen at in-focus axial distance. (z_1 in Fig.2.19).

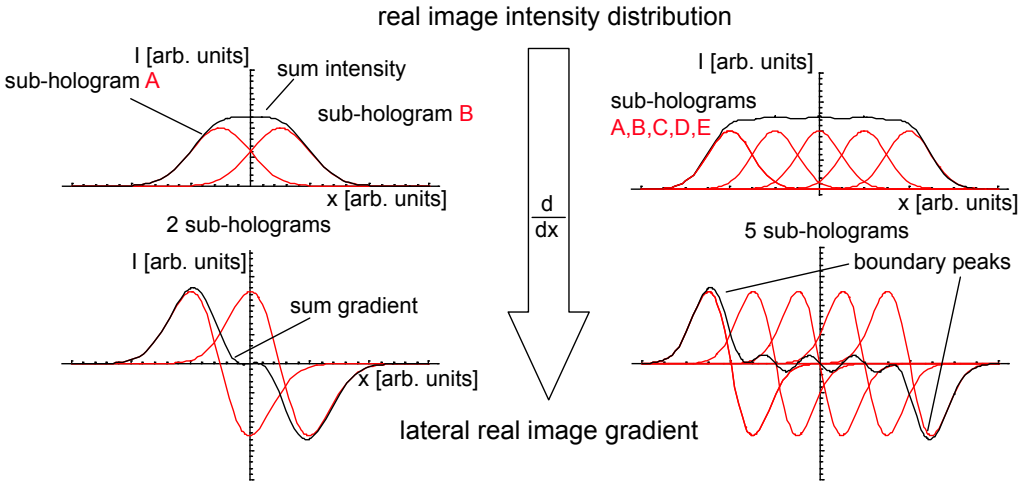

Figure 2.21: Real image intensity and lateral gradient from two (left) and five (right) sub-holograms projected onto out-of-focus diffusor screen (z_2 in Fig.2.19).

path, the derivative parallel to the path completely averages out. This averaging effect only occurs for out-of-focus points: If the real image projection is invariant under aperture shift, the gradient magnitude is not diminished.

For a MUPEGA-based hologram tomography the lateral gradient of each real image slices is calculated for each perspective. The intensity of the real image projection $I^{z,n}(x,y)$ at axial distance z from sub-hologram n defines the average lateral gradient $\langle d/dx, d/dy\rangle$:

$$\langle dI/dx\rangle \;:=\; \frac{1}{N}\sum_{n=1}^{n=N}\frac{I^{z,n}(x,y)-I^{z,n}(x+\Delta X)}{\Delta X} \tag{2.73}$$

where the brackets denote averaging over the real images of the N sub-holograms and ΔX is the (fixed) sampling spacing of the real image digitalisation: For simplicity, one can assume $\Delta X = 1$ since its actual value is of no importance. With similarly defined $\langle dI/dy\rangle$, one gets the average gradient magnitude

$$|\,\langle dI/dx, dI/dy\rangle\,| \;=\; \sqrt{\langle dI/dx\rangle^2+\langle dI/dy\rangle^2} \tag{2.74}$$

for each set of real image projections $I^{z,n}(x,y)$ at axial distance z from sub-holograms $n = 1\ldots N$.

With gradient averaging over multiple perspectives, the in-focus points defined by the axial distance of the diffusor screen are augmented whereas intensity from out-of-focus planes is strongly attenuated. A hologram tomography with different axial distances gives thus a surface representation of the object: The points with high gradient magnitude can be assigned to the surface. As with heuristic surface reconstruction, a relief of the surface can be generated by connecting the points of maximum lateral (i.e. the highest value for a certain lateral coordinate position) gradient magnitude.

MUPEGA resolution

In this section, an estimate for the resolution obtainable from multiple-perspective imaging is derived. For the analysis, the real image projections of the sub-holograms are assumed to have an infinite depth of field, i.e. they appear equally sharp at all projection screen distances. This simplification implies that the axial coordinate of an object feature cannot be determined by sharpness analysis, but that the axial distance of the surface has to be determined by triangulation of surface features. To estimate the uncertainty in axial coordinates, it is assumed that the lateral position can only be determined with a certain error. An example for such an uncertainty arises from the discrete digitalisation of the camera: the real image intensity is sampled in discrete lateral pixel bins with an effective size. The lateral position cannot be determined more precisely than this distance. Although other sources of uncertainty (for example from coherent laser speckle noise) also contribute to the lateral uncertainty, for simplicity the lateral uncertainty is identified with the effective lateral pixel size Δx.

The finite lateral resolution determines a finite axial resolution Δz_P which is referred to as geometrical resolution in the following. The dependence of this axial uncertainty on the reconstruction geometry is illustrated in Fig. 2.22). With the infinite depth-of-field, the sub-hologram real images are depicted as straight lines going from the hologram through the location of the object surface and beyond. Instead of point sources emitting spherical waves, one might think of these lines as the projections of object features (the grey/black bar in Fig.2.22) towards $(x_P = 0, z_P)$. For 3D-localization, the axial coordinate z_P of this object feature has to be deduced from lateral real image projections reconstructed from at least two sub-holograms, A and B. The projection screen is placed at an arbitrary distance z_0 and the object feature is projected on the screens at the lateral coordinates x_A and x_B. As the hologram tomography

digitizes the real image with a discrete lateral pixel spacing, the distance (i.e. the shift of the feature in between the two sub-hologram projections) can only be measured with an error equal to the effective lateral pixel spacing Δx. The axial coordinate z_P of the object feature is related to the distance D of the central points of the sub-holograms via the intercept theorem:

$$\frac{z_P}{D} = \frac{z_P - z_0}{x_A - x_B} \tag{2.75}$$

$$z_P = \frac{z_0}{1 - \frac{x_A - x_B}{D}}. \tag{2.76}$$

Due to the uncertainty in $x_A - x_B$, the axial distance has an uncertainty of

$$\Delta z_P = \Delta x \frac{dz_P}{d(x_A - x_B)} \tag{2.77}$$

$$= \frac{\Delta x z_P}{D - (x_A - x_B)} \tag{2.78}$$

For in-focus points, there is no shift $x_A = x_B$, giving

$$\Delta z_P = \Delta x \frac{z_P}{D} \tag{2.79}$$

$$= \Delta x / 2 \sin(\Omega/2) \tag{2.80}$$

where Ω is the angle between the view vectors of the sub-holograms. This result indicates how an uncertainty in the axial coordinate arises from an uncertainty in the lateral position when two sub-holograms are involved. With more holograms, the influence of the lateral uncertainty is less pronounced as error propagation indicates that the uncertainty cancel out partly. The two-hologram reconstruction can thus be seen as a worst-case resolution estimate which can be improved by using more sub-holograms. Additionally, the limited depth of field - described by the Rayleigh length - improves the localization of object features by multi-perspective gradient averaging as the gradient strength drops for projections at out-of-focus distances. As a simplification, one might assume that an object feature only causes a gradient *within* the Rayleigh-length defined by the area of the individual sub-hologram. In this sense, the geometrical resolution with infinite Rayleigh length is also a worst-case estimate. In conclusion, the Rayleigh-length z_R of the individual sub-hologram the and the geometrical resolution Δz_P define an upper and a lower estimate for the axial resolution of the MUPEGA technique. The experimental set-up and the implementation of the MUPEGA are presented in detail in section 3.3.1.

2.4.3 Perspective from mirror imaging

With a single planar hologram, only a limited field-of-view (a solid angle less than $\frac{1}{2}4\pi$) can be recorded. Another draw-back is that the hologram only contains information on object features which were (at least partly) visible from the hologram area (Bongartz [Bon02], pp.25 gives an analysis of partial visibility). To overcome problems associated with the partial representation of objects in their holographic recordings, one could simultaneously record multiple holograms. An even simpler approach is placing a planar mirror next to the object to record multiple perspectives simultaneously on the same holographic material. The use of mirror images for topometry has previously been realized in many applications, even with digital pulsed holography for particle position detection [Kre00]. In this thesis, the mirror recording technique was - to my knowledge for the first time - used in conjunction with topometric portrait holography.

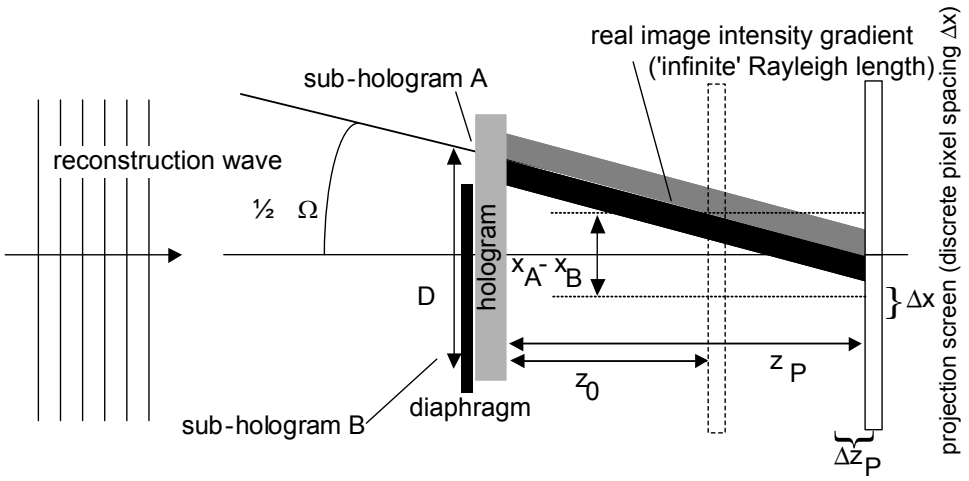

Figure 2.22: Resolution of MUPEGA: An uncertainty in the axial distance Δz_P arises from any lateral uncertainty Δx, for example the discrete effective pixel spacing of the digitalisation

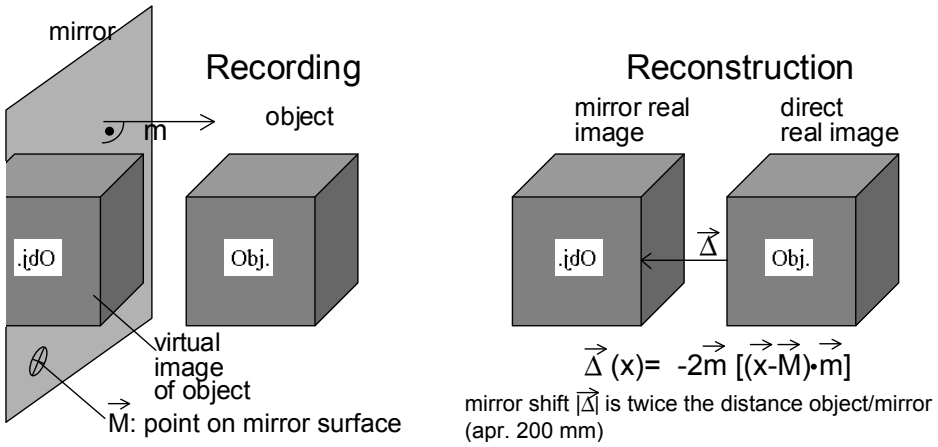

Figure 2.23: Hologram reconstruction of the virtual mirror image of an object results in a second, inverted and shifted real image

A plane mirror produces a virtual image of the object which is recorded with the wave field of the object itself. With virtual image reconstruction, the mirror image of the object appears as another virtual image. In real image reconstruction, the mirror image is reconstructed as a second real image of the object. The latter is referred to as the real image of the mirror object to distinguish it from the direct real image. Both reconstruct the same wave field, but with a different perspective. The location of the mirror object is shifted, the mirror object itself inverted relatively to the direct object (Fig. 2.23) . If the point $\vec{M}$ lies on the mirror surface which has a normal vector $\vec{m}$, $|\vec{m}| = 1$, object points $\vec{x}$ correspond to mirror object points $\vec{x}'$ via

$$\vec{x}' \quad = \quad \vec{x} - 2\vec{m}\left((\vec{x} - \vec{M}) \cdot \vec{m}\right) \tag{2.81}$$

45°-mirroring

For topometric applications, a hologram of a plane mirror can record multiple views of the same object. If the normal of the mirror encloses 45° with the hologram plane, the two real image volumes constitute two orthogonal views of the object.

If the real and the mirror image both are used for topometry, a so-called registration (i.e. the determination of the transformation between the two coordinate systems) of both images

is necessary: As the relative orientation of mirror and direct real image directly depends on the orientation and the distance of the mirror, these parameters have to be determined. For a hologram tomography, the mirror parameters must be known with an accuracy of less than the effective pixel spacing, respectively the slice thickness. If, for example, a pixel spacing of 0.5 mm was used and the average object-mirror distance was 300 mm with an object diameter of approximately 400 mm, the object points experience spatial shifts due to mirroring ranging from 200 mm (closest points) to 1000 mm. The latter applies to the object points with the largest distance to the mirror surface. With a mirror shift of $|\vec{\Delta}| = 1000$ mm and a tolerable error of 0.5 mm, the accuracy of the mirror angle should be below

$$\Delta\alpha \leq \frac{1}{2}\arcsin\left(\frac{0.5}{1000}\right) \tag{2.82}$$

$$\leq \frac{1}{4000}\text{rad} \tag{2.83}$$

This means that the angle of the mirror has to be known down to a quarter of a mrad which is difficult to achieve with conventional measurement devices: with a planar mirror of side length half a meter, a quarter of a mrad corresponds to an edge movement of only 125 μm. Although this stability could be provided by a solid mirror mounting and careful mechanical measurements, in this thesis the mirror parameter were deduced from the hologram recording itself. This was done by tracking the real image position of a well defined corner of a gauge object. This object (an aluminium bar) has been placed farther away from the mirror surface than any object point to achieve a large shift between direct and mirror gauge object. The mirror parameters were then determined from the digitized slices to give an absolute error of less than one pixel for all object points. The consistency of the mirror parameters was checked by subsequent tracking of different object points in the direct and mirror image.

Even without proper registration, mirror recording can be used for semi-heuristic surface reconstruction: For example, a hologram of an object recorded with a 45° mirror can give two relief surfaces corresponding to the direct and the mirror object. Each mirror perspective thus gives an additional relief and enlarges the recordable angle-of-view if both reliefs are properly registered. Even if the mirror parameters are unknown, an appropriate optimization of the relative orientation of the two relief surfaces can be calculated from the relief surfaces if the reliefs have a sufficiently high overlap. Suitable algorithms exist in computer vision, for example the search for iterative closest points (ICP) [BM92] which was implemented for relief data matching [Nüc02].

Apart from the straight-forward effect of enhanced holographic field-of-view, the orthogonal real images can also lead to an improved resolution from iterative deconvolution. In the frame of reference of the hologram, both direct and mirror real image of the object have the same PSF (Fig. 2.24, left). Relatively to the object and the mirror object, however, the orientation of the PSF is different relatively to the mirror object. More precisely, the mirror object has its own mirrored point-spread-function (MPSF) which is related to the PSF via the mirror transform (Eqn. 2.81). By numerical application of the inverse mirror transform to the mirror real image volume, the mirror real image can be superimposed onto the direct real image. In analogy, the transformed MPSF can be transformed into the frame of reference of the direct object. Whereas the back-transformed mirror object has the same location and appearance as the direct object, the back-transformed MPSF appears mirrored in comparison to the direct PSF.

The problem of finding an object function based on a discrete set of projections is known as discrete tomography [HK99] when the number of projections is small (as opposed to the problem of computer tomography where the reconstruction of the object is based on the quasi-continuous measurement of projection space). Contrary to three-dimensional x-ray imaging where the absorption of the object gives the individual cross-sectional projections, hologram tomography measures the sum of the light intensity scattered by the surface points. In x-ray

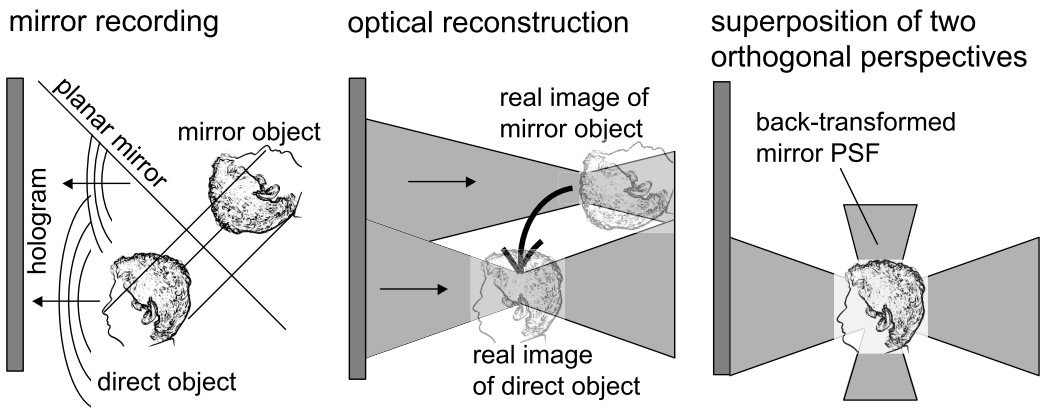

Figure 2.24: Two orthogonal perspectives of an object are recorded (left) and reconstructed (centre) by a planar mirror. By numerical back-mirroring, the reconstructed mirror object intensity is transferred onto the direct object intensity with orthogonal point-spread-functions.

imaging systems, detector and source are commonly treated as points whereas in hologram tomography, the integration is carried out over the support of the point-spread-function. Even more similarities to computer tomography exist in x-ray systems with extended detectors: They use the irradiation more efficiently with a technique known as cone beam tomography [NR02] where the absorption of the object is measured simultaneously along different paths. The SART algorithm has been developed for such complex reconstruction problems. In the experimental section (Sec. 3.4.2), an implementation of an iterative deconvolution algorithm is presented which is capable of combining several real images from mirror recording. The iterative deconvolution alternates between different measurement/MPSF pairs: In this way, an object can be reconstructed simultaneously from different perspectives to overcome the limited axial resolution from single-perspective holographic recordings. The following section illustrates the correspondences between SART and the formalism of iterative deconvolution.

Iterative deconvolution as simultaneous algebraic reconstruction

The assumption of a PSF which is invariant over the complete imaging volume is implicit to all deconvolution techniques in digital image processing. In the following, simultaneous algebraic reconstruction (SART) is reviewed and analogies to iterative deconvolution are discussed. SART replaces the concept of the convolution with the PSF by a matrix multiplication, but bears similarities with iterative deconvolution from alternating perspectives.

The algorithm of simultaneous algebraic reconstruction (SART) was developed for computed tomography by Slaney *et al* [KS88]. It iteratively constructs a (discrete) object function or object vector $\vec{O}$ from a set of different projections $\vec{I}_k$. These projections $\vec{I}_k$ are measured in the experiment. Note that although the object function is written as a vector, it represents a 2D object whereas the projections are one-dimensional: The elements of the k-th projection $\vec{I}_k$ represent the absorption of the object along parallel lines at angle θ_k (Fig. 2.25).

The object function thus satisfies a set $k = 1, \ldots, K$ of linear equations:

$$\vec{I}_k \quad = \quad \mathbf{A}_k \vec{O} \tag{2.84}$$

By analogy, the slices in hologram tomography are also projections (of the real image): By comparison with the PSF formulation, one can thus identify each slice of a hologram tomography with one projection of the SART algorithm (Tab. 2.1) The SART algorithm subsequently corrects the object vector $\vec{O}$ to satisfy the linear equations posed by each projection: The basic problem of SART is thus a matrix inversion. A direct matrix inversion is usually impossible.

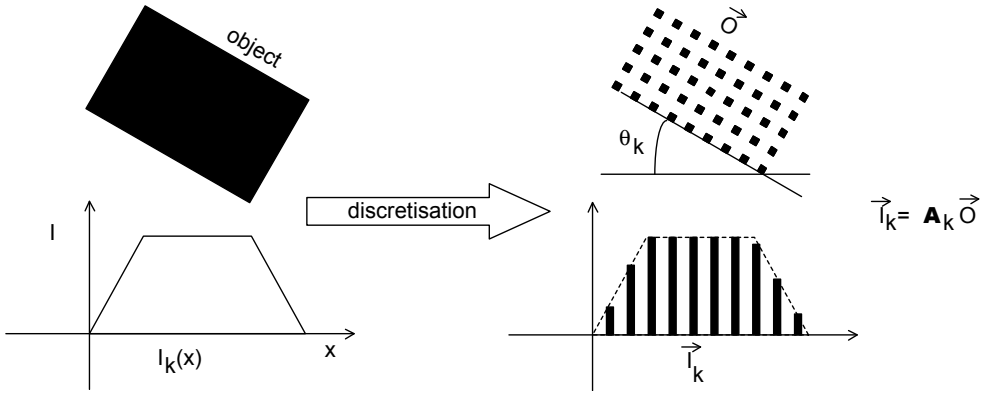

Figure 2.25: Discrete object and projection representation in computer tomography. $\vec{O}$ represents a 2D object I_k is a specific projection along a particular direction.

	quantity of interest	measured quantity	Fundamental equation	imaging system represented by
iterative deconvolution	3D object function O (3D object)	$I(x,y,z)$	$I = h \otimes O$	a single PSF $h(x,y,z)$
simult. algebraic reconst.	1D object vector $\vec{O}$ (2D object)	k projections $\vec{I}_k$ each a 1D line integral	$\vec{I}_k = \mathbf{A}_k \vec{O}$ $\forall k = 1 \ldots K$	imaging matrices $\mathbf{A}_k$ $\forall k = 1 \ldots K$

Table 2.1: Comparison of SART and iterative deconvolution

More than appr. 60,000 matrix elements are considered is too large for numerical (brute-force, i.e. without use of the sparseness) inversion [YdV00] and a matrix of this rank is easily reached in computer tomography and hologram tomography. Additionally, the projection matrix **A** is not necessarily square, i.e. the linear equation systems in computer tomography are commonly under-determined.

In the SART, the $i+1$-th object estimate $\vec{O}^{i+1}$ is constructed from its predecessor $\vec{O}^i$ by the k-th image vector $\vec{I}_k$ and the corresponding projection matrix $\mathbf{A}_k$ via [AK84]

$$\vec{O}^{i+1} = \vec{O}^i \mathbf{A}_k \frac{\vec{I}_k - \mathbf{A}_k^T \vec{O}^i}{\mathbf{A}_k^T \mathbf{A}_k} \tag{2.85}$$

If one would use SART for holography, the slice projection matrices $\mathbf{A}_k$ represent the point-spread-function for each object space point. Each element in the k-th projection matrix $\mathbf{A}_k$ describes how the real image intensity of a certain pixel in the k-th slice depends on a certain object point (i.e. an element of $\vec{O}$). Each of the K real image slices in hologram tomography can thus be interpreted as a projection vector $\vec{I}_k$. The matrix multiplication in equation 2.85 then replaces the convolution/deconvolution operation in iterativ real image deblurring. A spatially varying point-spread-function could be realized in SART through different projection matrices. In this thesis, no attempt was made to replace the (computationally economic) Fourier-transform calculation of the convolution integral with such a matrix-multiplication. The matrix multiplication would require the same amount of computation as the direct calculation of the convolution integral (as opposed to the multiplication in Fourier space). The direct calculation of the convolution integral has, however, been implemented- due to the extraordinarily long computation times (several days per convolution for a real image representation of $1024 \times 1024 \times 512$ volume elements) compared to the multiplication in Fourier space (90 sec for the same volume), this approach has not been carried forward.

Method	origin	type	set-up required	combines with
weighted neighbourhood	semi-heuristic surface detection	numerical	standard hologram tomography	deconvolution
iterative deconvolution	microscopy	numerical	standard hologram tomography	weighted neighbourhoods multi-perspective
inverse filtering	digital image processing	numerical	standard hologram tomography	weighted neighbourhoods
MUPEGA	-	numerical and physical	additional diaphragm	-
multiple perspective	computer vision computed tomography	physical	planar mirror	iterative deconvolution

Table 2.2: Comparison of different methods for hologram tomography

2.5 Summary

In this chapter, methods originally developed for microscopy (iterative deconvolution) and for general digital image processing (inverse filtering) were applied to hologram tomography for the first time. They allow the reduction of the defocus blur in hologram tomography. De-blurred real image tomographies can yield surface reconstructions either as the basis for semi-heuristic surface reconstruction or directly by the points of maximum intensity since the intensity in non-surface regions is considerably reduced. An extended semi-heuristic surface reconstruction algorithm with weighted neighbourhoods improves the lateral and axial resolution of the surface detection. The, to my knowledge, novel technique of multiple-perspective gradient averaging (MUPEGA) uses hologram perspective to detect the location of surfaces in the holographic real image. It can use the perspectives generated from a single planar mother hologram. Multiple perspectives of an object can also be recorded physically with a plane mirror. This method leads to multiple relief models covering an extended angle and also allows to improve the resolution of the reconstructions by iterative deconvolution with alternating object perspectives, a technique resembling simultaneous algebraic reconstruction. The five different approaches for hologram tomography are summarized in table 2.2.

Chapter 3

Experiments

In this chapter, the experiments and the implementations of algorithms developed for hologram tomography are described. The set-ups for object mirroring, for speckle projection, for structured illumination and for multiple-perspective gradient averaging are presented as well as a set-up for pulsed digital holography. An implementation of an iterative numerical deconvolution algorithm is introduced.

3.1 Hologram recording

Fig. 3.1 shows a photograph of the holographic recording set-up. Its main component, a pulsed Nd:YLF solid state laser and optical elements are enclosed within a metal housing, the holographic camera (Sec. 3.1.1). Within the camera, the laser beam is split into reference and object beam. The latter is divided into the right and the left object beam. The reference beam reaches the holographic plate at an angle of 66° over two external overhead mirrors (Leith-Upatnieks geometry, Fig. 3.2). The two object beams illuminate the object through two openings in the holographic camera, the object beam ports. To record holograms with a homogeneous illumination, two diffusor plates are inserted into the object beam ports. Homogeneous object illumination has the advantage that laser safety regulations allow a higher pulse intensity since the object is illuminated from an extended area of a diffusor screen (Sec. 4.1.3). For speckle projection, the object beams are focused into these diffusor screens. As a third option, the object beams are sent through projection slides instead of the diffusor screens to project high-contrast fringes. In this case, the divergence angle of the object beams is properly set by two additional lenses to control the appropriate distance of the high-contrast regions of the Talbot effect. For optimal placement of patients in medical application, an adjustable dentist's chair with three degrees of freedom (height, inclination of back, inclination of seat) is used. The optimum position for the patient is indicated by the point of intersection of the beams of two laser diodes (laser class 1, $P < 1$mW). The wavelength of those diodes (appr. 632 nm) is invisible for the green-sensitized analog holographic medium (3.2.1) and harmless to the human eye. The laser pointers are mounted next to the object beam ports together with two texture cameras. The texture cameras take digital colour photographs from two angles for surface colour information (Appendix A). Fig. 3.3 shows the complete signal flow during a single holographic recording. The manual master trigger starts the texture cameras: Two digital cameras (model Canon Powershot G2) take a photograph of the object simultaneously. To avoid saturation of the texture images, an electronic device delays the laser pulse for the holographic recording by approximately 1 ms. It discharges the flash lamp capacitor of the master oscillator and the amplifier in order to start the lasing activity. To obtain optimal gain in the amplifier, the delay between the pump discharge of master oscillator and the amplifier can be separately adjusted. The total pulse energy of the oscillator/amplifier is measured by a pyroelectrical pulse meter after the second

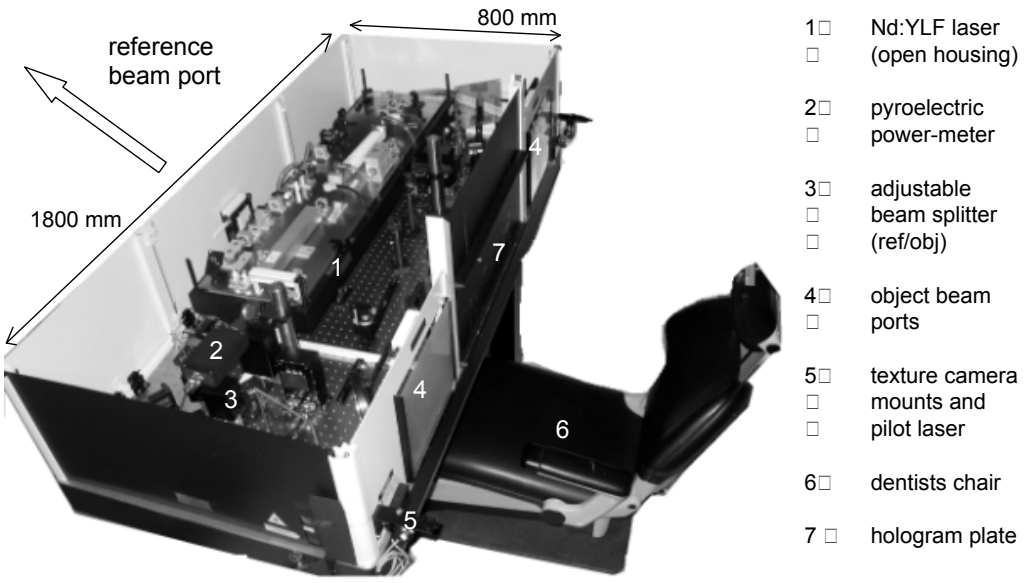

Figure 3.1: Photograph of the holographic camera (housing open)

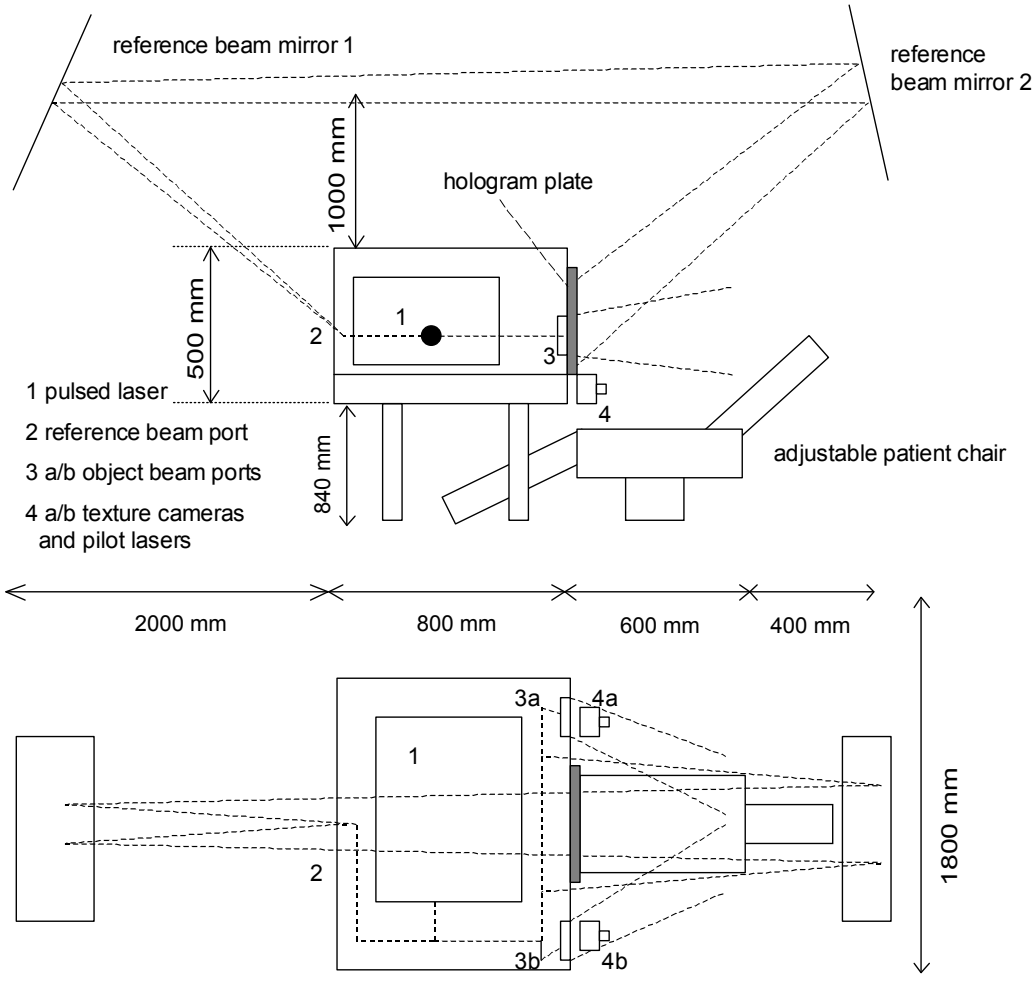

Figure 3.2: Side and top view of the holographic camera and the dentist's chair and the reference beam mirrors

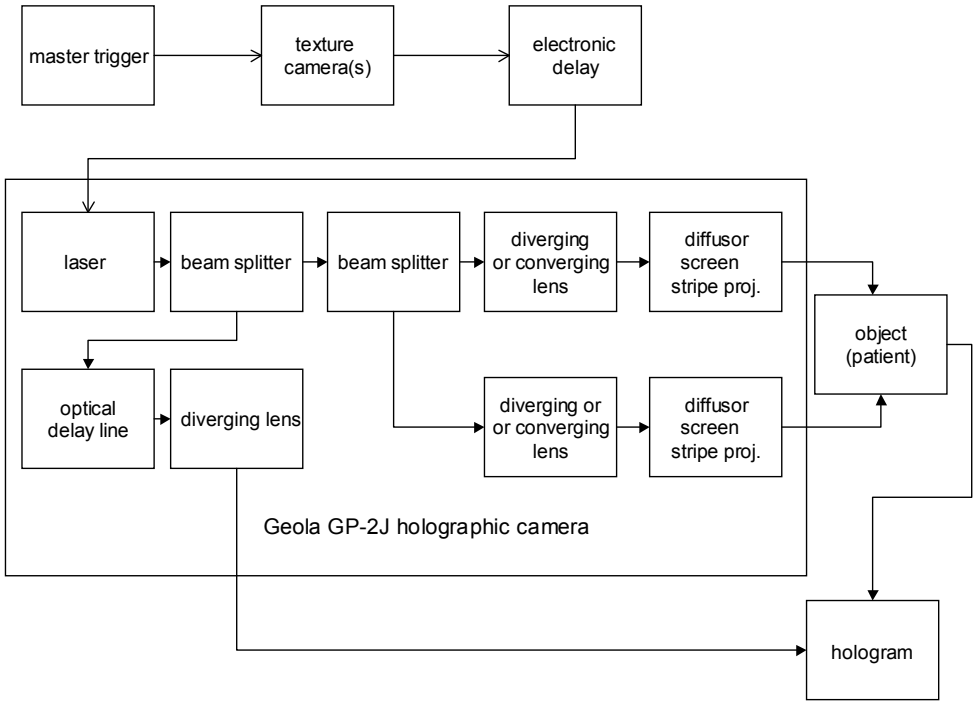

Figure 3.3: Scheme of a holographic exposure. Light arrow head: electronic, dark arrow head: optical signal

harmonic generation. The ratio of reference and object beam can be controlled by rotation of the polarization and a polarizing beam splitter. The reference beam and the scattered radiation from the object field reach the holographic plate simultaneously for maximum interference.

3.1.1 Geola GP-2J holographic camera

The pulsed laser used in the holographic camera is a master-amplifier combination designed to achieve a long coherence length at high pulse energies (Fig. 3.4). The master oscillator contains a flash-light pumped Nd:YLF crystal in a triangular ring cavity. For transversal single mode selection, the beam passes a spatial filter within the resonator. Single-frequency operation is achieved by two additional intra-cavity étalons. The Nd:YLF crystal of the master oscillator is Q-switched passively. The resonator includes a dove prism and an optical diode to suppress adversely propagating modes. It emits single-mode pulses of appr. 120mJ pulse energy at 1053 nm. The pulses are expanded by a telescope and can be amplified with a flash-light pumped Nd:glass amplifier. Two-pass amplification is achieved by inverting the propagation direction of the pulses with phase-conjugating Brillouin scattering after the first passage through the glass rod of the amplifier. This allows to maintain the high beam quality as the distortions of the amplifier are compensated in the second pass. The maximum pulse energy after frequency-doubling in a nonlinear crystal (DKDP) is 2 J at 526.5 nm. The pulse energy can be adjusted by the voltage of the flash-light pumping of the glass amplifier. The pulse duration of 35 ns (FWHM of the intensity envelope) was measured by Bongartz [Bon02]. The temporal coherence length is more than 5 m (manufacturer's specification). The beam is split subsequently into reference and object beam and left and right object beam. The reference beam leaves the holographic camera through a concave lens. It has a far-field divergence angle of

$$\Theta_{div} \quad = \quad 0.79(1)^{\circ} \tag{3.1}$$

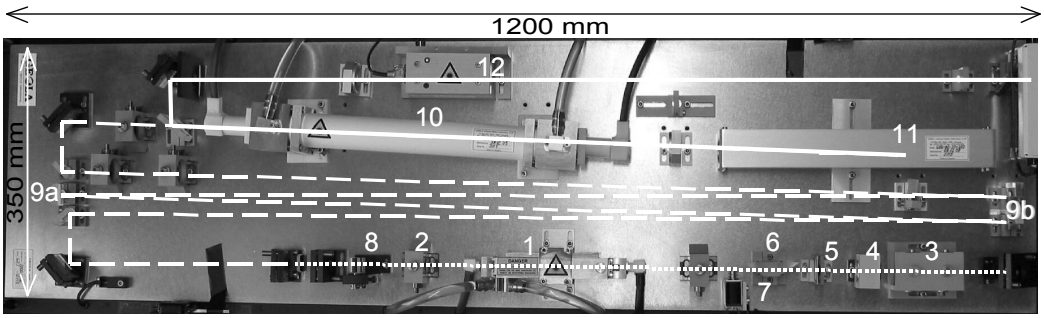

1	Nd:YLF laser crystal	7	mechanical shutter
2	transversal mode selection aperture	8	output mirror wedge
3	optical diode	9	expansion telescope
4	intra-cavity etalon	10	two-pass Nd:glass amplifier
5	saturable absorber	11	phase-conjugating mirror
6	dove prism	12	second harmonic generation

Figure 3.4: Photograph of the laser components. Dotted line: master oscillator cavity, dashed line: beam before amplification

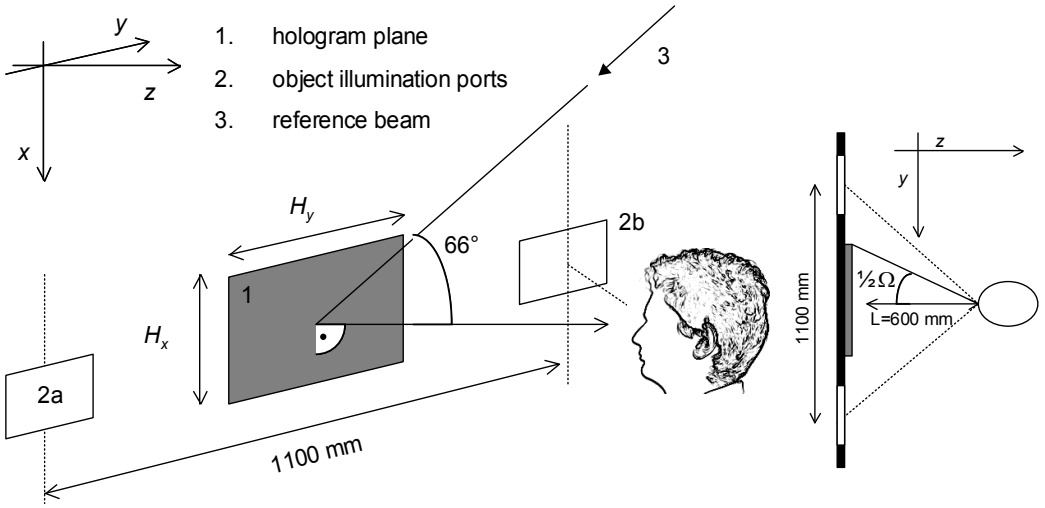

Figure 3.5: Left: Off-axis geometry for portrait holography recording. Right: Top-view

3.1.2 Object mirroring

For recordings on a holographic plate, the object or the patient is placed in front of the holographic camera in the centre between the object beam ports. The reference wave impinges at an angle of 66° from above onto the hologram plane. The object beams intersect appr. 600 mm in front of the hologram plane which is parallel to the camera housing. During recording, the object is located at the intersection of the object beams (Fig. 3.5). Depending on the lateral dimension of the hologram (max. 400 mm), it can record view vectors on the object with the view vectors covering an angle up to $\Omega = 39°$. (2.4.3). To record multiple perspectives on the same holographic material, a mirror is placed in the vicinity of the object (Sec. 2.4.3). The mirror plane is characterized by the mirror normal $\vec{m}$ and the coordinates of a point on the mirror surface $\vec{M}$. The mirrors used for multi-perspective recordings have dimensions of up to 1.700×1.500 mm^2 to record an entire human body (Sec. 4.3.2). As recording and illumination take place from approximately the same directions, the mirror can both illuminate the object and construct the mirror image without the need for additional object illumination.

3.1.3 Structured light illumination

Bongartz [Bon02] described structured object illumination by stripe projection: A semi-transparent slide is placed into the object beam which illuminates the object without the diffusor plates. This arrangement modulates the object beam spatially. At certain distances depending on the divergence of the object beam, a high-contrast stripe pattern similar to the pattern on the slide is projected onto the object, a phenomenon known as the Talbot effect. The stripe-projection method is problematic as the stripes are projected with a maximum contrast only at certain distances. Furthermore, at least two stripe patterns have to be projected from different angles to illuminate the whole surface of a human face. In their overlap region, a Moiré pattern develops which can make heuristic surface finding difficult. Finally, laser safety regulations could not be met with the coherent stripe projection [Bon02]. To overcome these problems, a statistical laser pattern was used for projection. It was generated by laser speckle projection: A laser speckle pattern is formed by focusing a coherent laser beam into a diffusor screen. The focus spot size of the object beam determines the speckle size of the object illumination- the larger the spot size, the finer the speckle pattern. Speckle patterns can be superimposed coherently without a Moiré effect. In comparison to the stripe pattern which has an optimum contrast only at certain distances, the speckle field has a high contrast at all distances. By using a large focal spot with speckle projection, an eye-safe projection could - in principle - be achieved. In practice, the minimum spot size for an eye-safe object illumination gives speckle sizes which are too small for high-contrast pattern projection on human skin (Sec. 4.1.3).

3.2 Holographic medium

The recording of optical interference fringes requires, in general, a photosensitive medium with high spatial resolution. This section describes recording on silver-halide (analog) photographic emulsion and electronic (digital) recording on a charged-coupled device (CCD). For medical portrait holography, the size and the resolution of the latter are too low for practical use. It is as well described in this thesis since its limitations stem from the large pixel size and the low pixel number, two technical problems which will be solved in the near-term future if the current pace in semiconductor development continues.

3.2.1 Analog recording material

Today, the commonly used holographic recording material is high-resolution photographic film. It consists of silver-halide salt crystals (the so-called grains) embedded in gelatine. The gelatine is coated onto a transparent substrate which may be a flexible film or a rigid glass plate. Silver halide salts are photosensitive: A photon with a certain photon energy according to Planck's law can raise an electron in the silver-halide crystal from the ground state into a higher energy level, eventually causing the reduction of a single silver atom (the actual processes are more complicated and involve several electrons [Bje95]). The energies needed to excite an electron in silver-halide crystals correspond to wavelengths from violet to ultra-violet. Chemical agents may be included in the photographic emulsion to increase the photosensitivity for light of a particular wavelength. Upon exposure to that wavelength, these agents act as electron donors. The single metallic silver atom acts as a catalyst during development: Silver-halide grains with at least one atom of reduced silver are reduced. After development, the remaining silver-halide crystals are washed out in a water bath. The metallic silver is not dissolvable. In a bleaching bath, the silver is bound into a stable, transparent salt. After bleaching, the gelatine contains transparent crystals and voids. The refractive index of the voids is lower than that of the silver salt. The probability that a particular site in the gelatine is filled with a transparent salt grain depends on the intensity of the interference field. For holographic recording, high-resolution

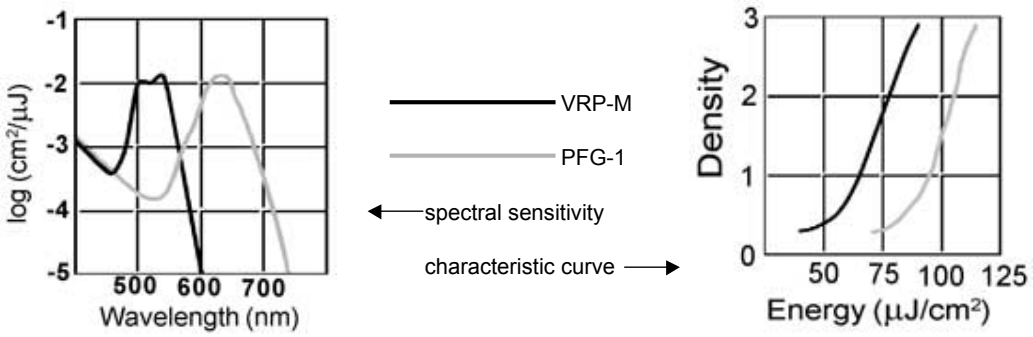

Figure 3.6: Transfer curve of VRP-M holographic material. Source: [ZRRV01]

material achieves a linear transfer curve (Fig. 3.6). For this thesis, fine-grained green sensitive holographic plates (type *VRP-M*, Slavich, Pereslavl-Zalessky, 152025, Russia) were used. The average grain size was 35-40 nm, the resolving power was more than 3000 lines/mm with a spectral sensitivity range from 488 nm to 532 nm with a peak sensitivity at 526 nm. In comparison, ordinary photographic black-and-white film (ISO 160 / DIN 23) has a resolution capability of 150 line pairs (at contrast ratio 1:1000) [Agf02]. A CCD chip with a pixel size of 6.5 μm pixel size has a resolution capability of 77 line pairs per millimeter.

After exposure with an intensity of 20-40 mJ/cm^2, the holograms were illuminated (the so-called latensification) with white light (60 W incandescent lamp at a distance of 600 mm from the hologram plane). Development was done with a 2 min *SM-6* bath [Bje95]. The plates were subsequently bleached (2 min) with *PBU-Amidol* .

3.2.2 Digital recording

As an alternative for holography on a photographic material, recording on an electronic device has been demonstrated by a number of researchers [JS94]. On the surface of a charged coupled device (CCD), photons are absorbed and create electron/hole pairs. The surface of the chip is subdivided into rectangular areas (picture elements or pixels) which conserve the electron/hole pairs due to their band structure. They can be read out to allow measurement of the density of electron/hole pairs which is within a certain range proportional to the light intensity, integrated over the exposure time and the pixel surface. This allows one to digitize the intensity of a light field electronically on a surface with the size of a chip (typically around 20 mm) with a spatial resolution of the pixel spacing (typically around 10 μm). The pixel spacing is larger than the actual pixel size to allow the integration of additional electronic control lines on the chip surface. The ratio of active pixel area and total occupied area is usually around 60$\%$. It is possible to record an interference pattern with pulsed lasers whose actual pulse length is much shorter than the exposure time (in the range of microseconds due to the control electronics). For the digital recording set-up, a 2048×2048 pixel CCD of a digital camera (Kodak, model ES-4.0) was used. The chip had dimensions of 15×15mm^2 and it was capable of digitizing the light intensity with a dynamic resolution of 12 bit (i.e. each pixel intensity is measured as an integer number from 0 to 4095). Due to the low spatial resolution of the CCD, the field-of-view was limited to $\theta_{max} < 5°$ at 526.5 nm. Holograms were recorded digitally in a modified Gabor set-up (Fig. 3.7) where the reference wave is superimposed onto the scattered object wave by a non-polarizing beam splitter cube. Alternatively, the object was illuminated not through the beam splitter cube but with an additional mirror (not shown in Fig. 3.7) to avoid direct reflections of the illumination beam from the front face of the beam splitter cube. These reflections could be avoided by proper anti-reflection coating of the beam splitter. The set-up comprises a stripe-projection unit to allow pulsed holographic topometry: A transparent slide

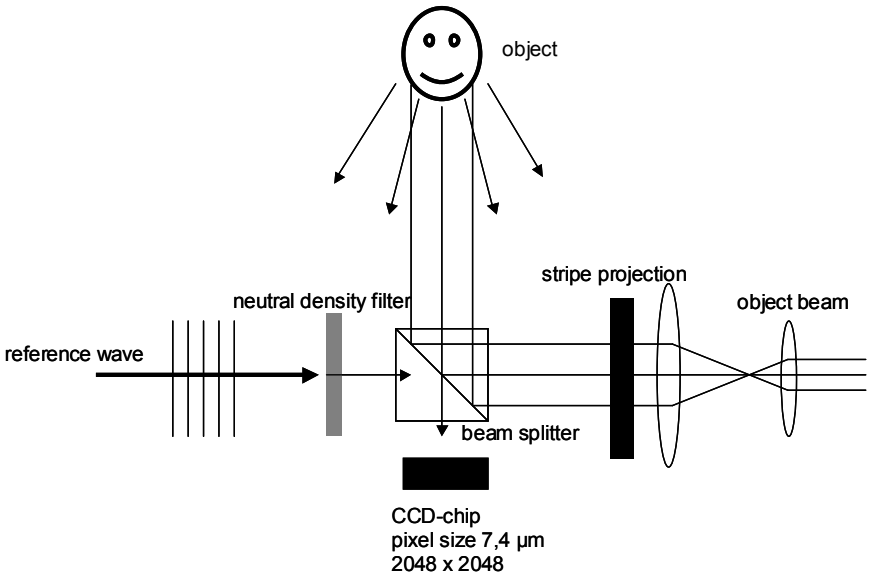

Figure 3.7: Modified Gabor set-up for pulsed holographic recording with stripe projection

with a stripe pattern (50 % absorbing, 50 % translucent) projects high-contrast fringes onto the object to avoid regions containing low lateral spatial frequencies.

3.3 Optical hologram reconstruction

This section describes the experimental set-up for optical hologram tomography (Fig. 3.8). For the optical hologram reconstruction, the complex conjugate of the reference wave has to be created. The reference wave of the Geola GP-2J is approximately a Gaussian beam wave with a far-field divergence $\Theta_{div} = 0.79(1)$ °. A combination of a beam telescope, a convex lens and a parabolic mirror creates the complex conjugate of the reference wave. The reference wave impinges onto the hologram plane at an angle of $66°$, illuminating an elliptical area of the hologram with an axis ratio of $1 : \cos(66°) \approx 0.41$. The laser is a frequency-doubled Nd:YAG solid state laser with cw single longitudinal mode operation (Coherent Verdi). It emits at a wave length of 532 nm. The ratio of the reconstruction over the recording wavelength is thus

$$\mu \quad = \quad 1.0104 \tag{3.2}$$

For hologram tomography, projections of the real image are made with a diffusor projection screen, the tomography screen. It is imaged onto the CCD-chip of a digital camera (Brand Kodak, 2048×2048 pixel at 12 bit greyscale resolution) by a conventional photographic objective (Nikon $f = 35$ mm). For volumes with a cross section smaller than the chip (15×15 mm^2), the CCD itself can be put into the real image volume to measure the intensity[1]. The diffusor plate/camera can be positioned with 1 micrometer accuracy (manufacturer's specification) by a linear translational stage. The image acquisition and the translational stage are controlled by a personal computer.

3.3.1 Multiple perspectives by aperture masking

This section describes the set-up and the numerical algorithm for calculation of a multiple-perspective gradient averaging (MUPEGA) hologram tomography. For this method, a spherical

[1]No such experiments are described in the following sections. This option was used mainly to adjust the set-up.

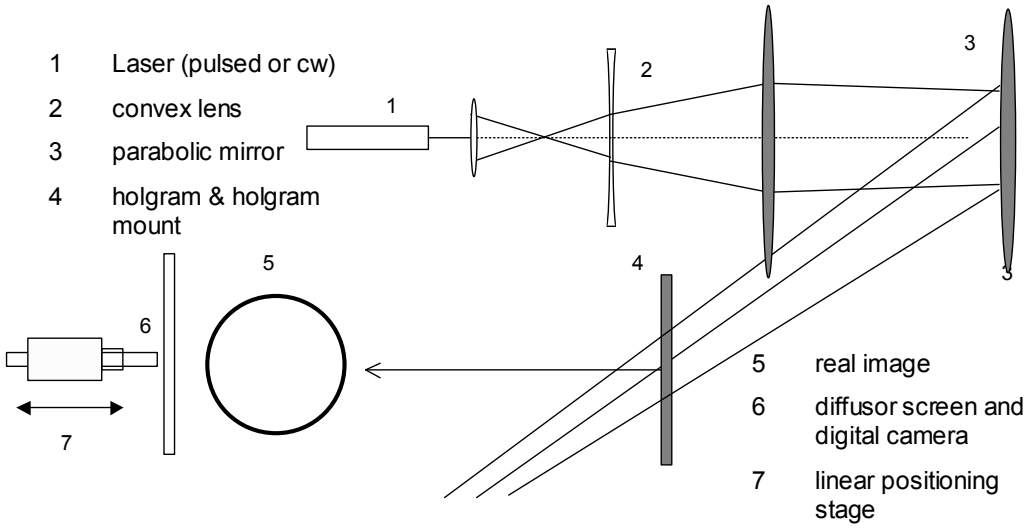

Figure 3.8: Scheme of the set-up for optical reconstruction. The angle at the parabolic mirror is appr. 12 °.

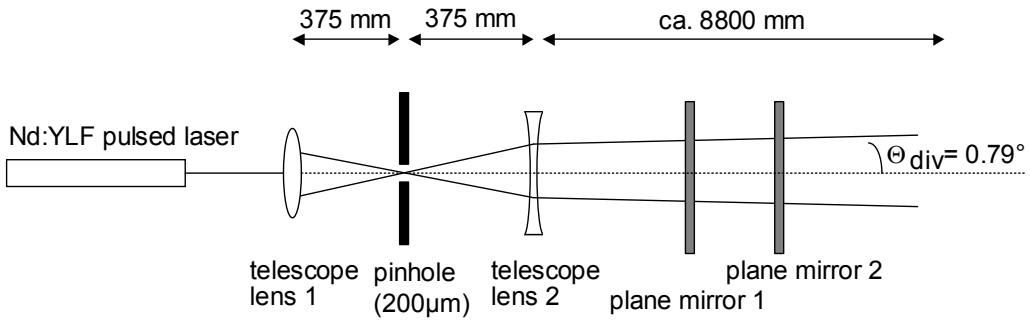

Figure 3.9: Reference beam path for pulsed hologram recording. The angles at plane mirror 1 and 2 are not drawn.

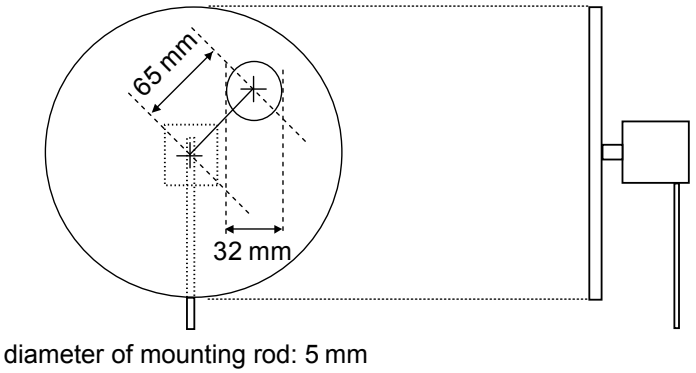

Figure 3.10: Disc with spherical diaphragm and stepper motor

diaphragm (diameter appr. 32 mm) was mounted on a spherical disc with a central point 65 mm from the central point of the disc. The disc itself was mounted on a digitally controlled stepper motor with an angular resolution of 0.36 ° (manufacturers specification) controlled by a personal computer. The disc was mounted on a 5 mm rod in the converging object beam as closely as possible (several mm) in front of the hologram plane. The mounting rod inevitably occluded a small region of the reconstruction beam (Fig. 3.10).

By rotating the disc, the real images $I_n, n = 1 \ldots N$ of several sub-holograms were reconstructed subsequently for a fixed projection screen distance. Each sub-image n gave a real image projection I_n^ζ at distance ζ which was numerically differentiated to give the lateral gradient vector $\langle dI/dx, dI/dy \rangle_n$ for each perspective n. The lateral gradient in x and y direction were calculated as the *difference quotient* of the discrete intensity values. The lateral gradient vector (2D) was averaged by summing the average gradient vector with two components. After all sub-holograms gradients were captured, the average gradient magnitude was stored on the hard disc. As the object was at distances of around 600 mm from the hologram plane and the diaphragm rotated on a circle of radius 65 mm with the rotation axis parallel to the reference beam (i.e. at an angle of 66° to the normal of the hologram), the view vectors of the sub-holograms enclosed different view angle intervals in the horizontal and the vertical axis. The angular intervals were

$$\Omega_{hor} = \arcsin(65/600) \tag{3.3}$$

$$= 6.22^\circ \tag{3.4}$$

$$\Omega_{vert} = \arcsin(65/600)/\cos(66^\circ) \tag{3.5}$$

$$= 15.29^\circ \tag{3.6}$$

Taking the second (larger) value for Ω, the geometrical axial resolution Δz_P (Sec. 2.4.2) can be estimated to be 3.75 times the effective pixel size (Eqn. 2.80). With $\Delta x = 200\mu$m, this gives a geometrical resolution of $\Delta z_P \approx 751\mu$m. The actual axial resolution thus should be lower than this value. A lower bound for the axial resolution is the Rayleigh length defined by the aperture of the sub-holograms (235 μm).

Memory requirements and implementation

Averaging over N perspectives for MUPEGA does not require an N-fold memory since the sub-hologram real image intensities do not have to be stored throughout the complete surface reconstruction. A closed surface relief is constituted by the points of maximum average gradient magnitude. Therefore, it is sufficient to store the overall maximum gradient magnitude values and an array indicating where (i.e. in which slice of the hologram tomography) they occur. If the gradient magnitude of a given slice exceeds the previously calculated overall maximum value, it replaces the latter and the corresponding surface position in the location array. A temporary buffer for calculation of the actual gradient magnitude is thus sufficient for an arbitrary number of perspectives and slices. This is of importance as the storage of a high-resolutional surface easily exceeds the capacity of standard PC equipment if multiple perspective data-sets have to be recorded for subsequent calculations.

The calculations of the average gradient magnitude are carried out by a C++ program which also controls the motion of the translational stage and the stepper motor of the diaphragm. It can be started using the following syntax:

```
CaptureControl c:\data\filename. 300000 200 16 1000
```

This line would start a hologram tomography over a total z range of 100,000 internal units of the linear translational stage. 2,000 units equal one millimeter, so the hologram tomography would

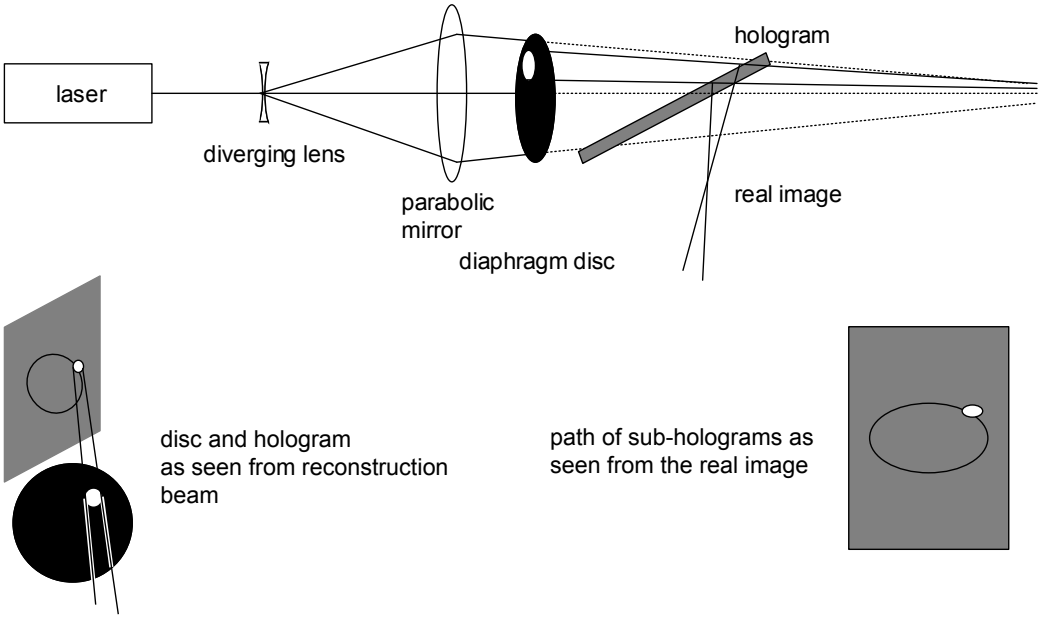

Figure 3.11: Perspective generation by aperture shifting. The area of the sub-holograms are generated by placing the disc with the spherical aperture in front of the hologram. Path and projection of the aperture are elliptical

comprise a z range of 150 mm. The next parameter indicates the number of slices (200). The slice spacing would thus be 0.75 mm. The third number indicates the number of perspective views. The fourth number determines the maximum speed of the linear translational stage (1000 units per second, i.e. 0.5 mm/s). The real image projections are in this example saved into the folder `data`, their names are `filename.001.tif` to `filename.200.tif` and they meet the (uncompressed) file convention for 16-bit `TIFF` images.

3.4 Real image deblurring

In this section, the numerical implementation of the deconvolution algorithms is described. The implementations were realized as plug-ins for the public domain image processing program `imageJ` from W. Rasband [Ras02]. The source code for the fast Fourier transform [JC65] were provided by N. Linnenbrügger [Lin02] who also implemented the inverse filtering plug-in `deconvolutionJ` whose generic form has been described, for example, by Gonzalez and Woods [GW93].

3.4.1 Inverse filtering

Inverse filtering is a technique to deblur images which were imaged by an imaging system with known point-spread-function. An inverse filtering is expressed as a division in Fourier space:

$$O \;=\; \mathsf{FT}^{-1}\left[\frac{\mathsf{FT}[I]}{\mathsf{FT}[h]}\right] \tag{3.7}$$

The right-hand-side might be ill-defined due to zeros in $\mathsf{FT}[h]$. After multiplication of the fraction with $\mathsf{FT}[h]$ and addition of a real constant γ to the denominator, one gets [GW93]

$$O \;\approx\; \frac{\mathsf{FT}[h]\cdot\mathsf{FT}[I]}{|\mathsf{FT}[h]|^2+\gamma} \tag{3.8}$$

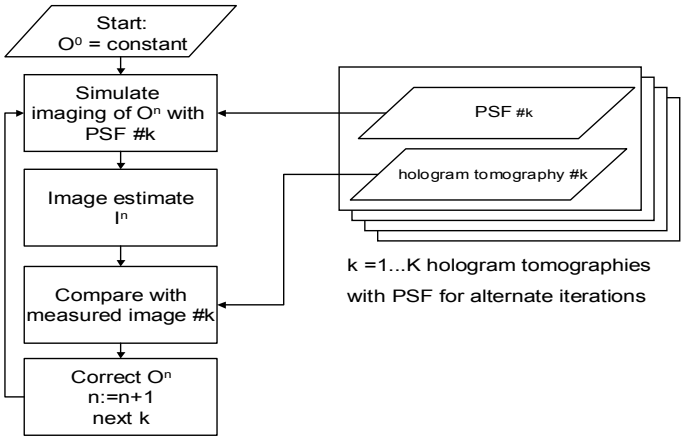

Figure 3.12: Iterative deconvolution flow chart. The iteration stops after a predefined number of iterations

The constant γ is chosen small compared to the average value of the power spectrum of the point-spread-function $|\mathsf{FT}[h]|^2$. Its units are intensity over length - if the intensity is measured as a 12-bit integer number, γ has the units $1/[\text{pixel}]$ or mm^{-1}. The Fourier transform was implemented as a fast-Fourier-transform (FFT) algorithm. FFT allows the calculation of the one-dimensional discrete Fourier transform with n elements with $N_{1D} \propto n\log(n)$ steps. A three-dimensional Fourier transform of grid with n^3 elements comprises $3n^2$ discrete Fourier transforms with n elements and can be calculated with $N_{3D} \propto 3n^3\log(n)$ operations [Pre92].

For the processing of hologram tomography data, the slices obtained from the real images are loaded into the RAM of a personal computer with the `imageJ` software as a so-called image stack. A representation of the point-spread-function can be generated by the plug-in `SyntheticPSF`. It calculates a representation of the PSF with floating-point intensity values (4 bytes per voxel) based on the Rayleigh length and the waist (in pixel units). Inverse filtering can either be realized by evaluation of the terms in eqation 3.8 directly with the `ImageCalculator` command of the `imageJ` software or the `deconvolutionJ` plug-in from N. Linnebrügger.

3.4.2 Iterative deconvolution

Another technique for image deblurring from microscopy is iterative deconvolution. Iterative deconvolution comprises a number of algorithms which try to approximate the object function with or without (blind deconvolution) the prior knowledge of the point-spread-function. Iterative algorithms simulate the imaging process by convoluting an approximation of the object function. At each iteration, a correction to the approximation is derived by comparison of simulated and actual image. An algorithm based on the work of J. Conchello [Con95] iteratively deconvolutes scans of the microscopic image with prior knowledge of the PSF. It takes a discrete representation of the Fourier transform of the PSF and a series of slices of the real image at different axial distances as the input. In the set-up described by Conchello, those are provided by a sequence of microscope images at different focal distances. In hologram tomography, they correspond to the different axial projections of the holographic real image which has the advantage that no changes in the object can occur. To account for holograms which comprise several, synchronously recorded perspectives of an object, the algorithm has been extended for multiple perspectives of the same object: It can alternate between different real image volumes and their respective PSF (Fig. 3.12): At each iteration, the correction of the object estimate is carried out with a different pair of real image volume and (M)PSF (corresponding to a certain perspective

on the object). The object function estimate is thus subsequently projected and compared with the different (blurred) 3D images of the object. A number of several perspectives are iteratively merged by this algorithm. For example, mirror recordings from pulsed holograms can be combined for an augmented axial resolution with this scheme.

The idea of using several projections of the same function for three-dimensional reconstruction has originally been developed for 3D reconstruction from x-ray projections of an object and is called simultaneous algebraic reconstruction (SART). In computer tomography, it is rarely used. Other algorithms, for example the inverse Radon-transform, give superior results non-iteratively but require the projections to be recorded from all directions, i.e. an angle of $\Omega \geq 180°$.

Implementation

The starting point of the iterative deconvolution is the initial guess of the object function, O^0. The current implementation starts with a constant object function estimate $O^0(x, y, z) = 1$. In the following, it is assumed that the object estimate from the previous iteration O^{i-1} and the point-spread function respectively its Fourier transform are known. In the following, an individual iteration is described: For the combination of several perspectives, both the representation of the OTF and the real image measurement are loaded from hard-disc in between iterations. The first step in each iteration is the simulation of the imaging process. The i-th estimate of the object function, O^i is convoluted to give I^i, the i-th estimate of the image. For computational economy, the imaging process is carried out as a multiplication in Fourier space. The object function is represented as a three-dimensional array of floating point (double precision) real numbers (8 byte per voxel). The multiplication thus requires a Fourier transform of the object estimate, a pixel-wise multiplication with the OTF and a back-transform into object space.

Alternatively, the imaging process can be calculated using a direct convolution. Direct convolution realizes space-dependent point-spread-functions without the border artifact from the implicit periodicity[2] of the image. However, the long calculation times and the high memory consumption made it impossible to apply the convolution on an actual portrait hologram. In this context, the calculation of the convolution integral is preferable in Fourier space (i.e. as a multiplication of the spatial frequencies) as opposed to direct evaluation of the convolution integral. Direct convolution requires n^6 multiplications compared to the $N_{3D} \propto 3n^3 \log(n)$ operations with FFT[3].

In the second step, the resulting image estimate is compared with the actual measurement by division to give a correction function E^i. In this implementation, the correction is simply the quotient of measured and simulated image intensity:

$$E^i(x, y, z) \quad = \quad I^i(x, y, z)/I(x, y, z) \tag{3.9}$$

The correction function is then back-projected into the object space to change the estimate for the next iteration:

$$O^{i+1} \quad = \quad O^i \odot E^i \tag{3.10}$$

The back-projection $\odot$ is realized as a convolution with $\tilde{h}(\mathbf{x}) = h(-\mathbf{x})$. One can easily verify that $I^i = I$ is a stable point for the iteration. If a solution exists, the iteration converges towards it as solutions are unique. This second projection is also realized as a Fourier-space multiplication.

[2] A periodic function has a discrete Fourier representation and vice versa. A the discretized Fourier transform implies thus the periodicity of the original function

[3] For small values of n, however, the direct multiplication can be faster as the operations used in the FFT calculation comprise several multiplications

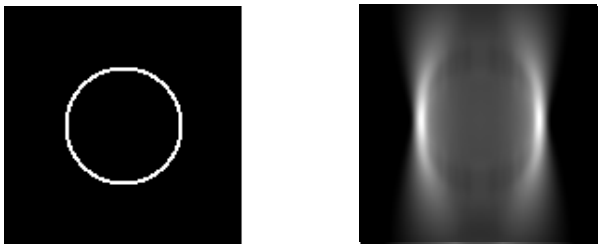

Figure 3.13: Cut through a numerically simulated hollow sphere: Intensity of the object surface (left) and simulated holographic real image (right)

This iterative deconvolution is implemented as plug-ins for the `imageJ` software [Ras02] named `Convo3D` and, for alternating iterative deconvolution with multiple perspectives, `DoubleConvo3D`. The program take the representation(s) of the PSF (and the MPSF), the slices of the real image(s), the object function estimate and the number of iterations as parameters. If alternating perspectives are used (`DoubleConvo3D`), the representation of the mirror PSF and the mirror real image are temporarily stored on hard-disc to free memory for the calculation of the Fourier transforms. After the complete number of iterations, the object estimate is written onto the hard-disc. As with inverse filtering, the representations of the PSF and the MPSF can be generated with the `SyntheticPSF` plug-in and, for the MPSF, a three-dimensional affine transform, for example implemented by the freely available plug-in `TJAffine` which can be downloaded from the `imageJ` web-site [Ras02].

Deconvolution example

As an illustration, an iterative deconvolution of a synthetic image volume is presented in the following. The object function, a hollow sphere of thickness Δ, is defined as

$$O(x,y,z) \quad = \quad \begin{cases} 1 & R < \sqrt{x^2+y^2+z^2} < R+\Delta, \\ 0 & \text{otherwise.} \end{cases} \tag{3.11}$$

The object function O was discretized on a cubic grid of $128 \times 128 \times 128$ volume elements (voxel). The radius of the sphere was $R = 40$ and the thickness Δ was 2 voxels. The real image of the synthetic sphere was simulated by convolution with a point-spread-function of a double-cone with opening half-angle $\alpha = 0.3$ (the singularity of the cone was removed by setting the central voxel to a finite intensity). A cut through the symmetry plane of the object representation parallel to the z (light propagation) axis and the simulated real image can be seen in Fig. 3.13. The iterative deconvolution is demonstrated in Fig. 3.14, where the estimate for the object function $\mathbf{O}^i$ is shown for $i = 2, 10$ and 100. To monitor the convergence, a plot of the average squared difference between estimated and measured intensity versus the iteration number can be seen in Fig 3.15. An artifact arises from the use of the Fourier transform for evaluation of the convolution integral: A discrete function in Fourier space represents a periodic function in object space. In this sense, the object volume is treated as the elementary cell of an infinite, periodic object. The higher intensities near the boundaries are an artifact arising from this implicit periodicity assumption. In the literature, the common way of dealing with those boundary artifacts is to enclose the objects by a larger zone without any intensity and to ignore the volumes close to the boundaries [Con95]. This example demonstrates that with the implementation of the iterative deconvolution algorithm, a numerical reduction of the out-of-focus intensities is possible. From the deblurred intensity distribution, a surface reconstruction can be obtained from the points with maximum intensity. In contrast to the heuristic surface

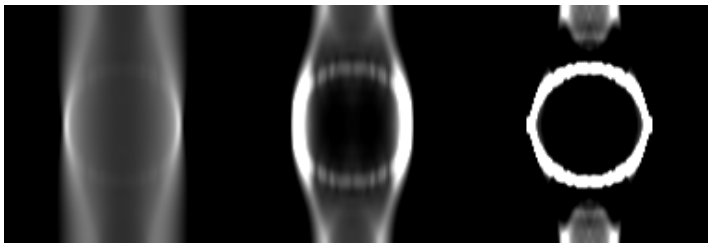

Figure 3.14: Iterative deconvolution of the simulated object (Fig. 3.13): Object estimate O^i for $i = 2, 10$ and 100.

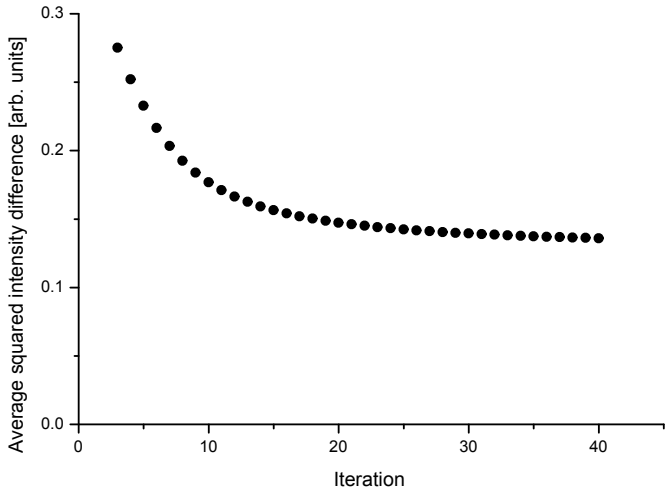

Figure 3.15: Convergence of the iterative deconvolution algorithm: Average squared difference between image estimate and measured image from Fig. 3.14.

finding algorithm which reconstructs only relief surfaces, i.e surfaces which can be described by a two-dimensional function $z(x, y)$, this iterative deconvolution also works with arbitrary 3D objects. However, any real measured data contains noise as opposed to this example of a synthetic real image, for example caused by laser speckles. The intensity noise is inconsistent with any simulated image and thus causes a non-zero error estimate even with the correct object function. The noise in the measured data thus hinders the convergence of the iterative deconvolution. With strong noise, the convergence could be suppressed altogether. Even without noise, a perfectly deblurred image might need a large number of iterations. After a finite number of iterations, one thus can only assume to get an approximation of the object function. As an alternative approach, one can use the partly deblurred estimate of the object function (i.e. the object estimate after a few iterations) for heuristic surface finding: This approach was used in this thesis as the iterations converged too slowly for an intensity-only based surface reconstruction.

Chapter 4

Results

The characteristic properties of the holographic camera, the results obtained with different methods for hologram tomography and examples for the application of holographic topometry are presented and discussed in the following chapter. It starts with the camera characterization, including the measurement of the incoherent point-spread-function (Sec. 4.1.1), the temporal resolution (Sec. 4.1.2) of the recording process as well as the minimum lateral speckle size for projection on human skin (Sec. 4.1.3). An example for mirror recording is presented in section 4.1.4: A planar mirror was placed at an angle of approximately 45° to the hologram plane to record a second perspective with an orthogonal view vector.

The second part of the chapter compares the different methods for hologram tomography. The optimum parameters for weighted neighbourhoods semi-heuristic surface detection are determined (Sec. 4.2.1). Results from hologram real image deblurring with inverse filtering and iterative deconvolution are presented in section 4.2.2. The method of multiple perspective gradient averaging (MUPEGA) for surface reconstruction is used to reconstruct the surface of a test object with the highest axial resolution (Sec. 4.2.3) obtained and a first reconstruction recorded with eye-safe laser intensity.

The third section contains a examples of the application of hologram tomography. A surgical correction of an overjet of the lower jaw was documented and planned with portrait holograms (Sec. 4.3.1). As a further illustration of the technique of mirror recordings, the hologram of an archeological finding, the Husbäke bog body, is presented (Sec. 4.3.2).

A digitally recorded hologram leading to a virtual hologram tomography (Sec. 4.4) concludes the chapter to show the potential of pulsed holography in conjunction with electronic recording.

4.1 Camera characterization

In this section, the spatial (Sec. 4.1.1) and temporal resolution (Sec. 4.1.2) of the holographic camera are determined. The spatial resolution of the surface models depends on the structured illumination and, in this case of projection on human skin, on the penetration of the radiation into the skin. Experiments demonstrate the loss of contrast with the projection of fine laser speckles on human skin by comparison with projection onto an aluminium surface (Sec. 4.1.3). A set-up for mirror hologram recording for synchronous capture of multiple views is presented in section 4.1.4.

4.1.1 Holographic point-spread-function

An experimental determination of the (incoherent) point-spread-function (PSF) of the holographic real image is commonly realized in microscopy by imaging a small, quasi point-like

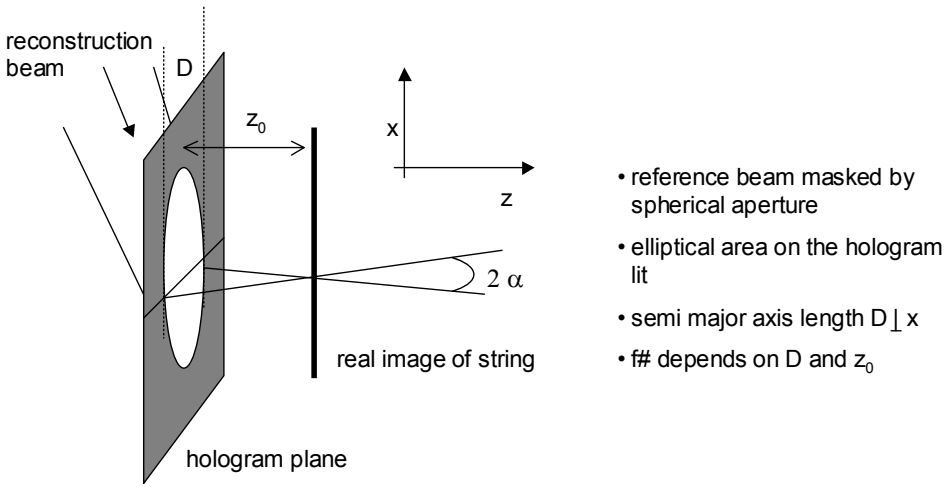

Figure 4.1: Set up for measurement of the line-spread-function: The hologram diameter D is set by the size of the reconstruction beam

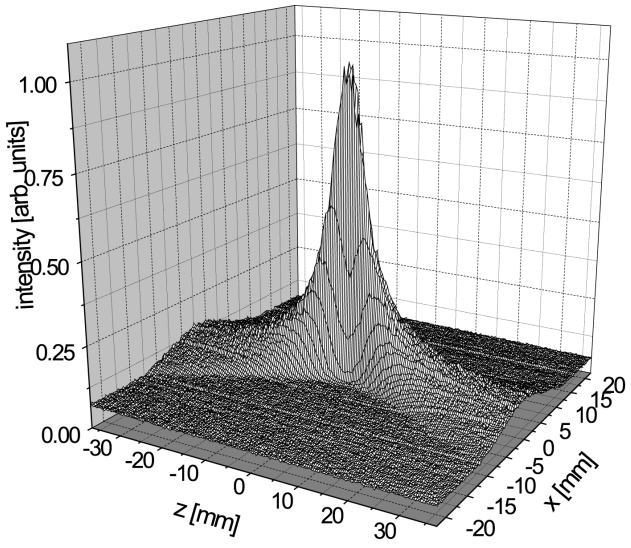

Figure 4.2: Experimentally measured real image intensity of a string measured by hologram tomography

object to obtain an approximation of the image of a point source [FH98]. For the present set-up, a hologram of a white string with a radius of approximately $R_S = 0.2$ mm was recorded. The real image intensity cross section perpendicular to the string was measured to determine the one-dimensional PSF, also known as the line-spread-function of the imaging system. An typical experimentally measured intensity distribution is shown in Fig. 4.2. The real image cross section of the string in a plane parallel to the y axis is a superposition of the intensity emitted from the string surface. Assuming that the intensity from each surface point of the string contributes the same intensity with a PSF of a Gaussian beam, the cross-sectional real image intensity can be written as the sum intensity from all surface points:

$$I(y,z) \quad = \quad I_0 \frac{w_0}{w(z)^2} \int_{-R_S}^{R_S} e^{-2\frac{(y+\eta)^2}{w(z)^2}} d\eta \tag{4.1}$$

where the line-spread function is kernel of the integral. This intensity distribution resembles a Gaussian beam for $R_s \ll w(z)$ as can be seen by expanding equation (4.1) in orders of

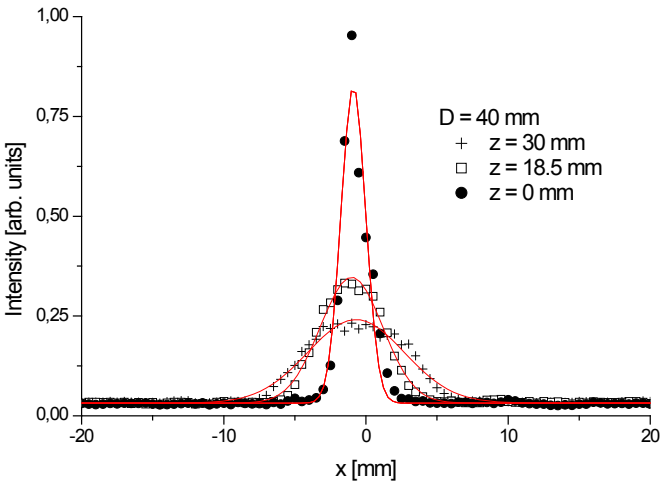

Figure 4.3: Experimentally determined intensity cross-sections of the real image at three different distances.

$R_S/w(z)$ around $R_S = 0$: The first non-vanishing term (the second order) yields a lateral intensity distribution which is proportional to $\exp\left(-2\frac{y^2}{w(z)^2}\right)$. Although proximity to the string, the assumption $R_s \ll w(z)$ does not hold since the waist of the PSF is significantly smaller than 200μm, the cross-section of the measured intensity was nevertheless approximated by a Gaussian beam by least-square fitting to determine the lateral width $w(z)$ of the PSF.

To measure the dependence of the aperture stop on the PSF,the hologram was masked by a spherical diaphragm. The reconstruction beam impinged on the hologram at an angle of 66 ° and thus illuminated an elliptical area of the hologram with a semi-major axis of length D (parallel to the y-axis, i.e. orthogonal to the string and to both x and z axis). The aperture stop $f\#$ of the hologram was defined by the diaphragm size (Fig. 4.1). Any further effects of the aperture on the reconstruction wave field (secondary waves caused by diffraction at the diaphragm) were neglected.

From the real image of the string, the real image was digitized with an axial slice spacing of $\Delta z = 0.5$ mm. A plot of the image intensity as a function of lateral coordinate y and axial coordinate z is given in Fig 4.3 for a fixed aperture stop.

The width $w(z)$ of the intensity cross-section was determined for each slice, i.e. for each axial distance z individually by a least-square fit of an assumed Gaussian cross section although for large axial distances, the cross-section deviates from the Gaussian shape (Fig. 4.3, third curve). For a fixed hologram aperture, the measured dependence of the square of the width w^2 on the axial distance z is depicted in Fig. 4.4.

The z-dependence of the width is in good approximation described by

$$w^2(z) \approx w_X^2(1+\frac{z^2}{z_X^2}) \tag{4.2}$$

where w_X is called the extended width. For an ideal point-like object, the extended width equals the waist of the PSF $w_X = w_0$ whereas with an object of finite size like the string, one can approximately identify the smallest value of the real image with the string radius itself: $w_X \approx R_S$. With an ideal point-like object one could directly deduce the Rayleigh length z_R and waist w_0 from the real image intensity distribution: In this case, $z_X = z_R$. With a finite-sized object, however, only the far-field divergence of the point-spread-function $\frac{z_R}{w_0}$ has to match the far-field divergence $\frac{z_X}{w_X}$ of the real image distribution of equation 4.2. The extended Rayleigh

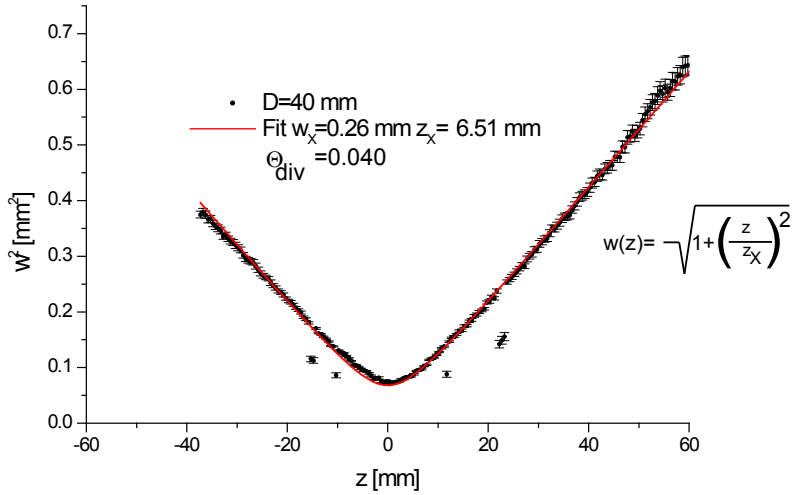

Figure 4.4: Widths of the cross-sections of Fig. 4.3 as a function of axial distance

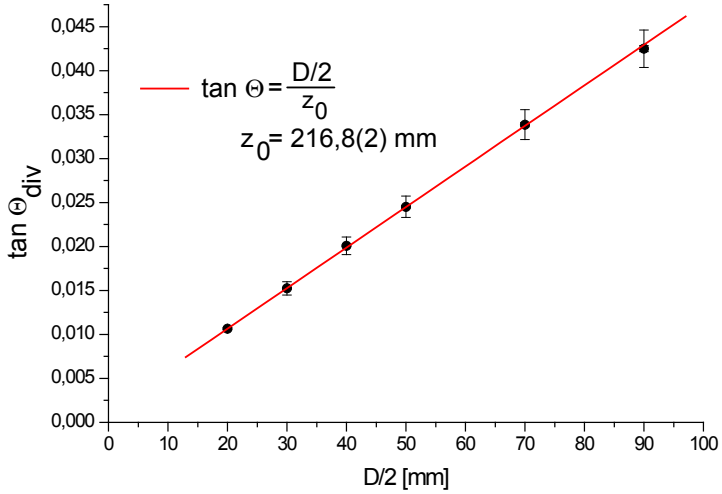

Figure 4.5: Experimentally measured far-field divergence of the real image for different hologram semi-major axis sizes D/2

length z_X is thus

$$z_X = z_R \frac{w_0}{w_X} \tag{4.3}$$

$$\approx z_R \frac{w_0}{R_S} \tag{4.4}$$

The far-field divergence angle has been calculated from the experimentally determined values of w_X and z_X for several hologram aperture stops (Fig. 4.5).

4.1.2 Temporal resolution

The exposure time is most commonly used for the characterization of the temporal resolution of an imaging system. It is defined as the time of image acquisition. Any object which is not moving considerably during the exposure time can be imaged without motion artifacts. In holography, the term considerably means the object must not move over a distance in the order of the recording wavelength: The temporal resolution is thus not only determined by the pulse duration, but also by the wave length. If the object moves too fast, the interference

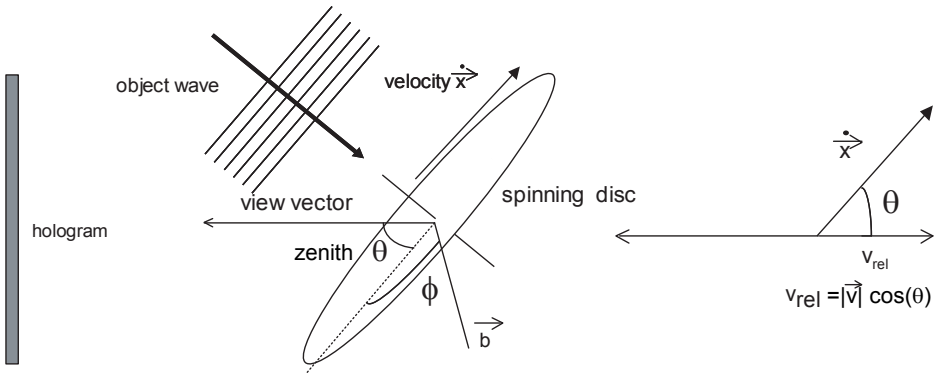

Figure 4.6: Velocity vector of a spinning disc surface. The velocity relatively to the hologram plane determines the interference contrast

pattern is not stable during the exposure and no fringes can be recorded. In this section, a set-up for experimental measurement of the temporal resolution of the pulsed holographic camera is presented. It allows one to determine the maximum tolerable velocity for objects. One can estimate the order of the allowable velocity by the quotient of pulse length and recording wavelength, for the given parameters approximately $\frac{526.5\text{nm}}{35\text{ns}} = 15.0$ m/s.

To determine the maximum allowable velocity, holograms of a spinning disc were made. The points near the axis of the disc move with a lower velocity than the points at the edge of the disc. The points on the disc moving too fast do not contribute to the interference pattern of the disc and are not present in the hologram reconstruction. The intensity of the virtual image is hence a function of the velocity of the object points. The transition between points which are recorded and points with reduced visibility is smooth. For quantitative analysis, v_{max} is defined as the velocity of those points on the disc with half the virtual image intensity of the points with zero velocity. The virtual image was photographed digitally with a $f = 50$mm objective. The view vector was determined with conventional metal rulers and from the aspect ratio of the virtual image of the (spherical) disc. A stripe pattern was projected onto the disc to allow precise determination of the size of the visible parts of the spinning disc.

Evaluation of the maximum tolerable velocity

For the formation of the interference pattern, the direction as well as the magnitude of the velocity vector is of importance: When the object moves relatively to the object wave, the phase of the object wave changes due to movement. Additionally, the phase of the scattered wave on the hologram plane shifts as the distance to the object point changes. Both effects have to be considered and depend on the orientation of the object wave and the holographic plane relatively to the object.

In the experiments, the axis of the spinning disc was oriented parallel to the wave vector of the object wave. The object points thus do not move relatively to the to the wave fronts of the object wave and only the magnitude of the velocity vector parallel to the view vector $v_{rel} = \dot{x}_{\|}$ (Fig. 4.6) has to be considered.

A dedicated, non-moving Cartesian coordinate system can be defined in the plane of the disc by two orthogonal vectors $\vec{a}, \vec{b}$ where the latter is perpendicular to the view vector $\vec{b} \perp \vec{v}$. The trajectory of each point $(a(t), b(t))$ can be written as

$$a(t) = r_0 \cos(\phi_0 + \omega t) \tag{4.5}$$

$$b(t) = r_0 \sin(\phi_0 + \omega t) \tag{4.6}$$

As the b-component does not contribute to v_{rel}, the magnitude of v_{rel} can be expressed by the (scalar) time derivative of the a-component :

$$v_{rel} = |\cos(\theta)\dot{\vec{x}}| \tag{4.7}$$

$$= \cos(\theta)\frac{d}{dt}a(t) \qquad [v_{rel}] = \mathrm{m/s} \tag{4.8}$$

where θ is the zenith of the view vector in the spherical coordinate system whose horizontal plane is the disc. The time derivative $\frac{d}{dt}a = \dot{x}$ equals

$$\dot{a} = \frac{d}{dt}r_0 \sin(\phi_0 + \omega t) \tag{4.9}$$

$$= \omega r_0 \cos(\phi_0 \ + \omega t) \tag{4.10}$$

$$= \omega \cdot b(t) \tag{4.11}$$

For all points, v_{rel} is thus proportional to the abscissa of a coordinate system whose ordinate is parallel to the view vector. Fig. 4.9 shows photographs of the virtual image of the spinning disc. The disc appears dark in the hologram images where the relative velocity v_{rel} towards the view vector has been too high to yield an interference pattern. By changing the observation point, different perspectives with different visibility of the disc can be seen from the same hologram.

The remarkable property that *different perspectives show different visible areas of the object* can be used to determine the maximum tolerable surface velocity for pulsed hologram exposure. Whether or not a certain point on the disc appears in the virtual image depends on the view vector and - according to equation 4.13 - to its abscissa.

The view vector of such a perspective is conveniently expressed by its azimuth and zenith angle. The zenith θ can be calculated from the aspect ratio (horizontal to vertical) of the disc:

$$\theta = \arcsin\left(\frac{\Delta X}{\Delta Y}\right) \tag{4.12}$$

where ΔX and ΔY were measured in the photograph of the virtual image. The relative velocity is then

$$v_{rel}(t) = \cos(\theta)\omega b(t) \tag{4.13}$$

Also noteworthy is that viewing the disc under various azimuth angles changes the orientation of the visible/invisible area on the disc. This is because the $v = 0$ line (i.e. the ordinate of the coordinate system) appears always parallel to the view vector and includes the disc hub (Fig. 4.7).

A hologram of a spinning disc ($D = 0.12$ m) was made with an angular frequency of the disc of $\omega = 2\pi \cdot 200$ Hz. The maximum absolute velocity (at the disc edge) was thus 75.4 m/s. The hologram was made with structured object beam of high contrast stripes. Several photographs of the virtual image were taken from different zenith angles. An intensity cross sections of a photograph of the real image is shown in Fig. 4.8.

The cross-sectional intensity distribution was assumed to have a Gaussian envelope in the virtual image. A least-square intensity fit determined the cross section of the visible area in the virtual image photographs. The observable zenith interval was from $\theta = 25^\circ \ldots 50^\circ$ obtained from a the same hologram. A plot of $\cos(\theta)$ vs. w is shown in Fig.4.10.

A least-squares line fit gives a maximum tolerable velocity of

$$v_{max} = 15.4 \pm 0.4 \quad \mathrm{m/s} \tag{4.14}$$

where the uncertainty of 0.4 mm/s stems from the χ^2 of the least-square fit.

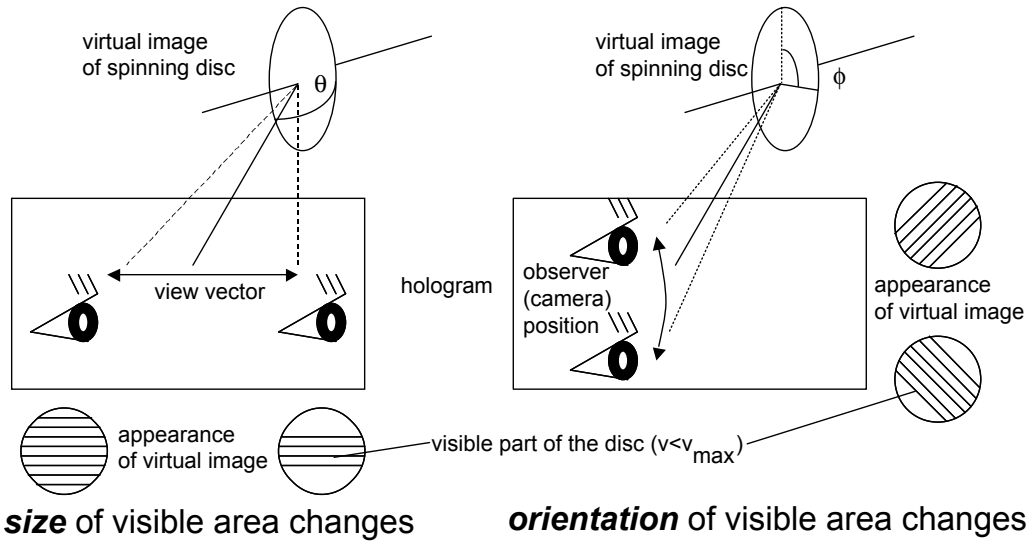

Figure 4.7: Virtual image of a spinning disc: Different zenith (left) and azimuth (right) view angles changes size and orientation of the visible area

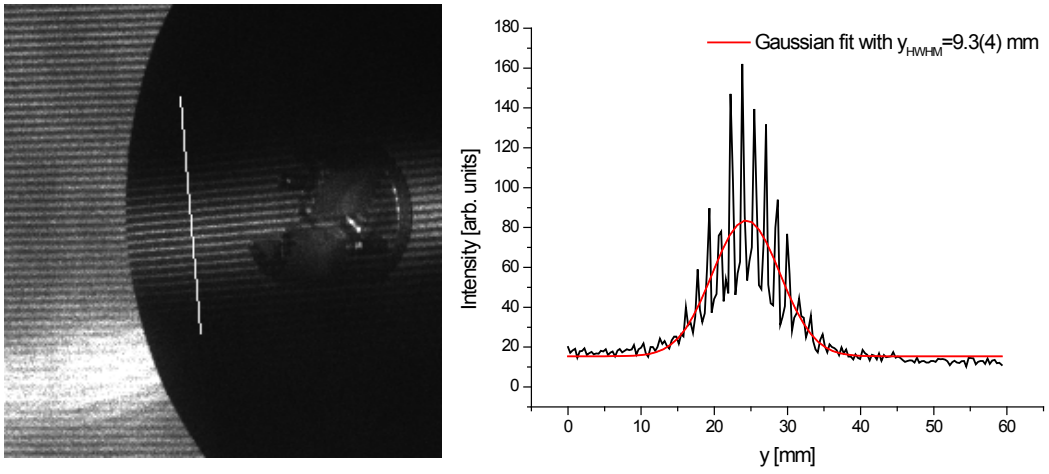

Figure 4.8: Virtual image of the spinning disc (left) . The white line indicates the cross-section measurement (right)

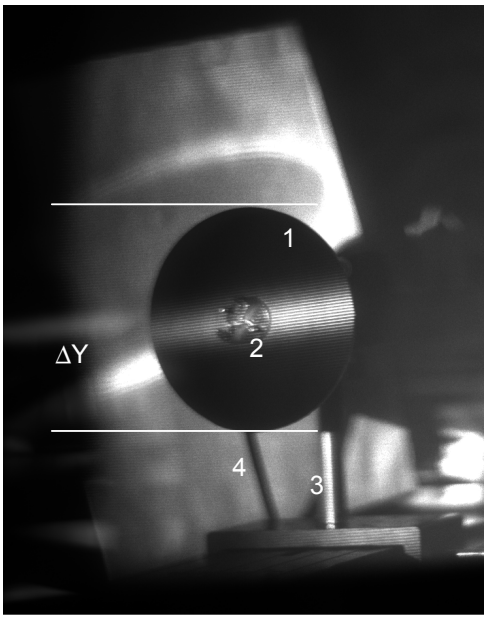

A

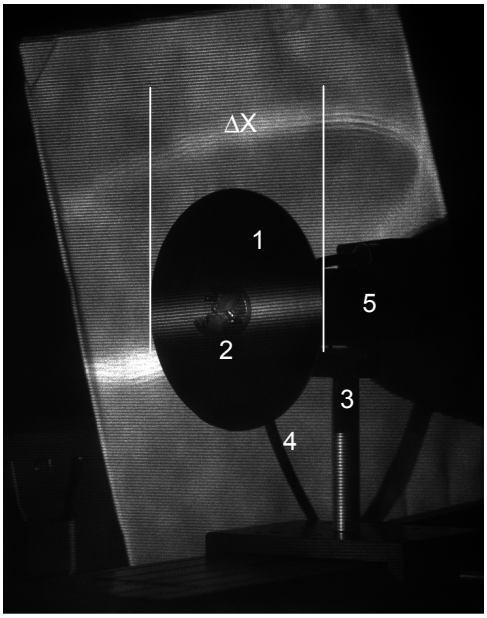

B

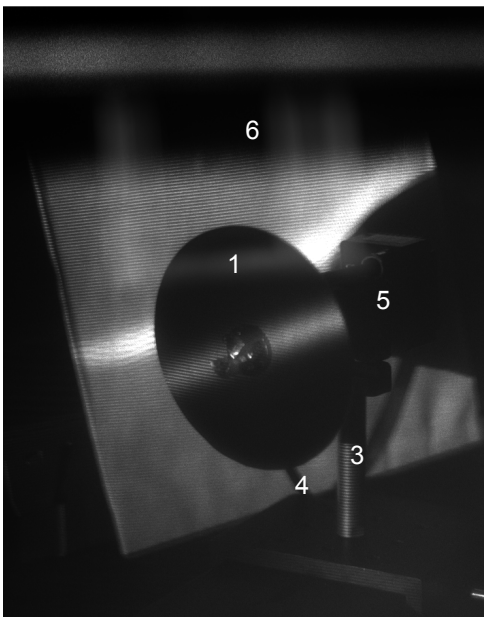

C

1□ spinning disc

2□ disc hub

3□ mounting rod

4 □ motor control cable

5 □ motor

6□ hologram border

A , B: different zenith

A , C: different azimuth

Figure 4.9: Photographs of three views on the virtual image of the same hologram with different zenith and azimuth angle

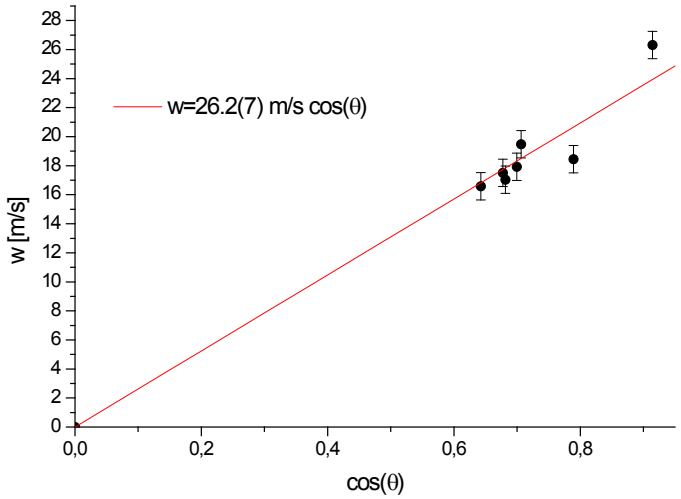

Figure 4.10: Experimentally determined dependence of the width w of the visible area on the spinning disc as a function of zenith angle

4.1.3 Speckle projection

In this section, the maximum spatial resolution obtainable with speckle projection on human skin and the eye-safeness of the projection are discussed. It is shown that on human skin, the minimum average speckle size is 0.5 mm due to light diffusion into the tissue.

The common way of speckle pattern generation is focusing a coherent laser beam into a diffusor plate (Sec. 3). The resulting speckle field can be projected onto any surface and gives a characteristic laser speckle pattern (Sec. 2.1.4). The smaller the spot size of the laser beam, the larger is the average speckle size. Due to the light diffusion into the tissue, however, there is a lower limit on the speckle sizes which can be projected onto skin (Sec.4.1.3).

For eye-safe recordings, a limit on the speckle size stems from the laser safety regulations: The intensity of a laser pulse must not exceed a certain threshold if the focal spot of the laser can be observed by the eye (which is the case if no laser goggles are worn). The maximum intensity depends on the solid angle under which the focal spot appears as seen from the observer. The larger the solid angle, the higher the maximum allowable intensity. Laser safety regulations thus impose that for a given intensity, the spot size on the diffusor screen must be larger than a certain area. In terms of the average speckle size, this means that the speckle size for eye-safe recordings can not be made arbitrarily large as this would require arbitrarily small focal spot sizes (Sec. 4.1.3).

Speckle contrast

The lack of high-contrast features in the skin surface makes heuristic surface finding difficult and lowers the axial resolution. Deliberate speckle projection creates a high-contrast intensity modulation on the object surface and leads to a better axial surface localization with a trade-of in lateral resolution since fine lateral details are lost. A fine speckle pattern would thus be preferable for the lateral resolution. However, due to penetration of the radiation into the skin, the projected structures cannot be made arbitrarily small. The loss of speckle contrast due to light diffusion into the skin was deduced by comparison of the contrast of a speckle field projected on human skin versus the contrast of the same speckle field projection on brushed aluminium. The latter shows no reduction of speckle contrast due to light diffusion as the penetration depth of visible light into the aluminium bulk can be neglected (the skin depth at optical frequencies is in the nm range for all metals). The contrast ratio (i.e. the contrast on human skin divided by the contrast on aluminium) served as a measure for the reduction of contrast due to the penetration of the light into the skin. The average speckle size was changed by variation of laser spot size on the diffusor plates in the holographic camera. Variations of the speckle field contrast and other systematic effects (limited resolution of the camera etc.) cancel out in the contrast ratio. The average speckle size was estimated by the first minimum of the autocorrelation function (Fig 4.11). An example for the speckle field projection photographs on human skin and aluminium at different speckle sizes is depicted in Fig. 4.12. The contrast

$$C = \frac{\sigma_I}{\langle I \rangle} \qquad [C] = 1 \tag{4.15}$$

of the speckle photographs decreases with the speckle size on human skin as fine structures smear out. The ratio of speckle field contrast projected on human skin over the contrast on aluminium is shown in Fig.4.13. The measurements were conducted on the skin at the back of the hand of the author. For large speckle sizes, the ratio of the contrasts is equal to one or even larger than one as the intrinsic features of the skin (absolute contrast under white light appr. 0.12) modulate the image stronger than the brushed aluminium surface (white-light contrast appr. 0.04). The intrinsic skin features of facial skin strongly depend on the subject itself: Small pores in the skin, hair, pigment etc. also vary the skin contrast.

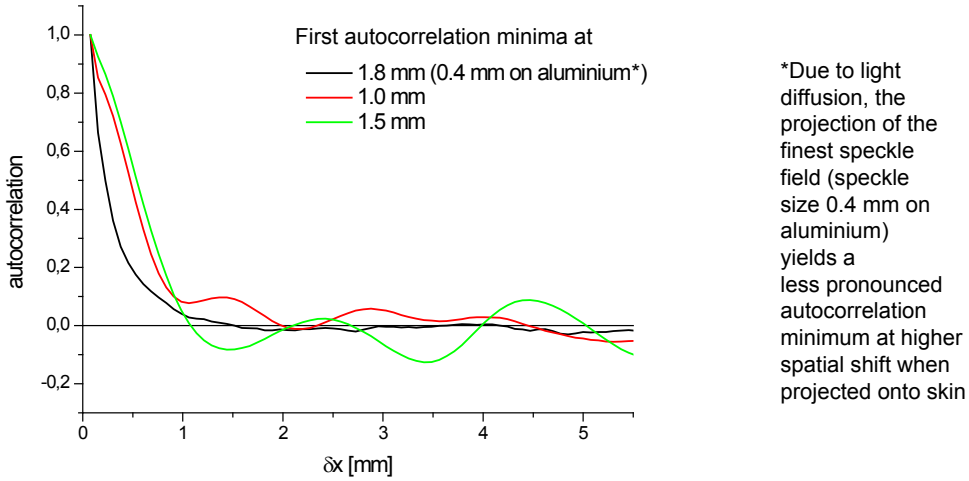

Figure 4.11: Autocorrelation curves of speckle patterns on skin. The first minimum of the curves determine the respective speckle size.

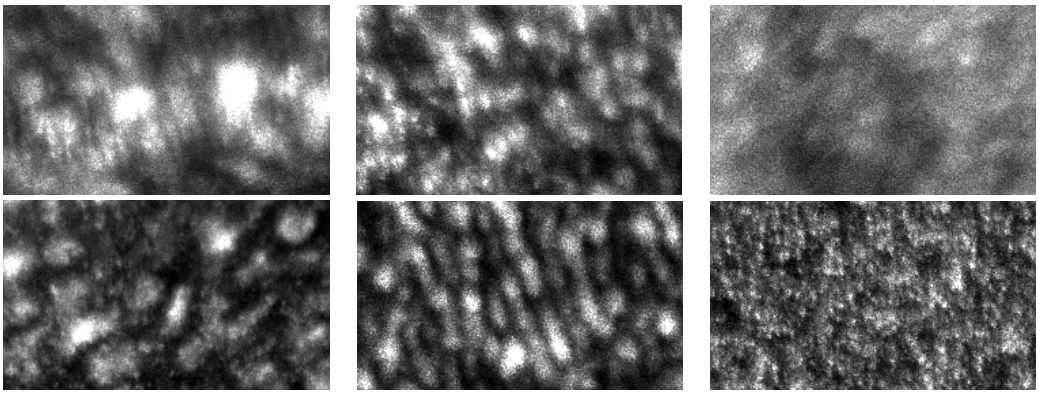

Figure 4.12: Photographs of speckle projections on human skin (upper row) and brushed aluminium (lower row). Avg. speckle size 1.5, 1 and 0.5 mm

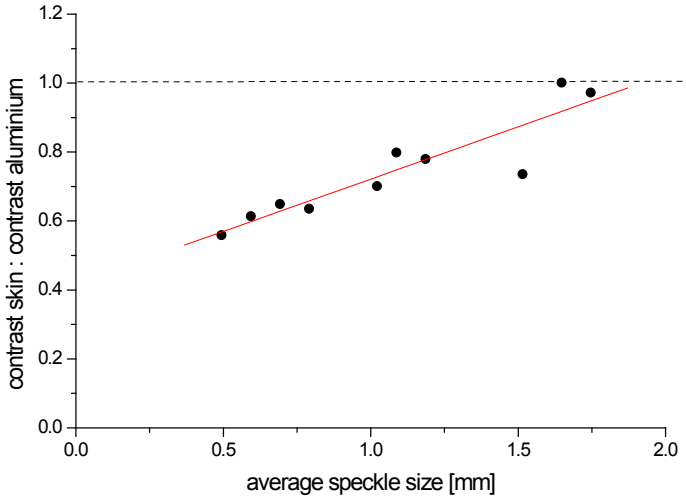

Figure 4.13: Ratio of the speckle contrasts on human skin over the speckle contrast on aluminium

On the back of the hand of the author, no speckles with sizes below 0.5 mm could be projected : Speckle projection with an even larger spot (i.e. a finer field) size cause the projections of the speckles pattern on human skin to smear out. The first minimum of the auto-correlation function is thus actually at larger sizes, i.e. the apparent speckle size increases though the speckle field is finer as can be confirmed by measurement of the auto-correlation of the projection of the field on aluminium: Projections of a speckle field with average sizes as small as 0.2 mm were realized on the aluminium surface. The speckle contrast on human skin at a speckle size of 0.5 mm is approximately $\frac{1}{2}$, the diameter of the focal spot is approximately 3 mm. Further experiments with a larger number of volunteers might indicate an optimum speckle size as a function of the skin colour and structure.

Laser safety

When imaging human subjects, safety regulations for laser radiation have to be observed. The current guidelines for exposure to laser radiation [oNIRP00] define the exposure limit (EL) for light of different wave length and pulse duration. The exposure limit is the intensity which must not be exceeded when the pulse is measured with a detector with an aperture of diameter 7 mm. For pulses of visible radiation of a wavelength between 400 and 700 nm, the EL for pulses of 35 ns is

$$EL \;=\; 0.5\, C_E \text{ mJ/cm}^2 \tag{4.16}$$

where the factor C_E depends on the angle α under which the extended source appears from the eye:

$$C_E \;=\; \begin{cases} 1 & \text{for } \alpha < \alpha_{min}, \\ \alpha/\alpha_{min} & \text{for } \alpha_{min} < \alpha < \alpha_{max}, \\ \alpha^2/(\alpha_{min} \cdot \alpha_{max}) & \text{otherwise.} \end{cases} \tag{4.17}$$

The limiting angles are $\alpha_{min} = 1.5$ mrad and $\alpha_{max} = 0.1$ rad. In the present set-up, the radiation source is the camera object beam diffusor at an eye distance of approximately 900 mm. The diffusor is illuminated with a collimated beam for speckle projection or a widened beam for homogeneous illumination. For a completely illuminated diffusor screen (a square of side length 300 mm), the factor C_E is hence approximately 1,500, whereas for focal spot sizes smaller than 1.35 mm, C_E equals one. The intensity emitted from one of the diffusor plates of the camera was measured with a pyro-electric detector (coherent LM-P3) at a distance of 900 mm. The detector had a circular aperture with a diameter of 10 mm. Although laser safety regulations indicate that the measurement are to be made with a diaphragm diameter of 7 mm, the measured intensities of the (homogeneous) speckle field should not depend strongly on the aperture size. With speckle projection, the pulse energy was measured to be

$$E \;=\; 40 \pm 5\mu\text{J} \tag{4.18}$$

corresponding to an intensity of $51 \pm 6\mu$J/cm^2. The intensities varied with the total pulse energy, which was around $1.1(2)$J (as indicated by the internal pyroelectric pulse meter of the camera). This intensity is about two orders of magnitude above the exposure limit. For a focal spot radius of 150 mm, the geometric correction factor $C_E = \alpha/\alpha_{min}$ equals 100, making speckle projection eye-safe (at the same intensity). However, the speckles projected with a spot size radius of 150 mm are too small for high-contrast projection onto skin as shown in the preceding section: To obtain the smallest projectable speckles, the a focal spot size on the diffusor screen must not exceed approximately 3 mm- a larger focal size creates an even finer speckle pattern.

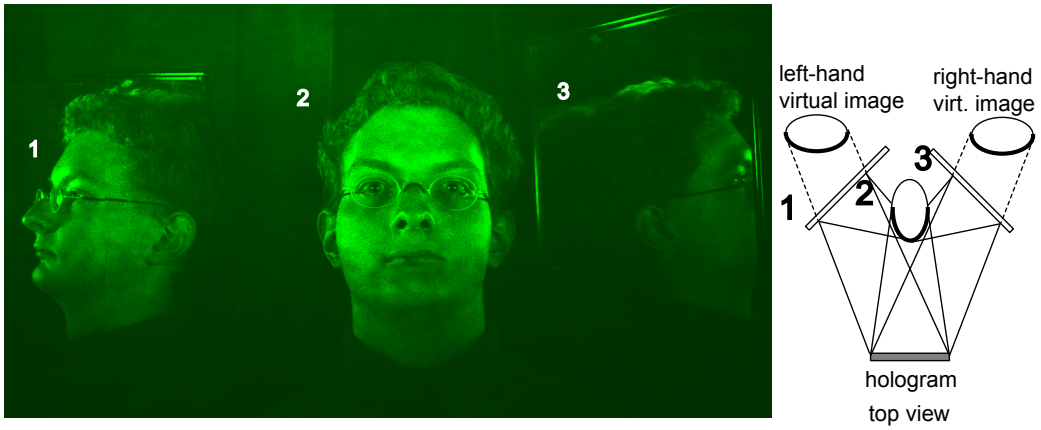

Figure 4.14: Virtual image of a portrait hologram recorded with two mirrors showing one frontal and two profile perspectives

4.1.4 Multi-view holograms with mirror recording

In this section, the technique of 3D recordings by object mirroring is presented. Mirror recording is essential for a complete object description: With a planar hologram, the wave field of the object can only partially be recorded. For example, with a planar hologram of side length 300 mm at a distance of 600 mm, the field-of-view (i.e. the angular interval included by the boundary view vector) recorded by the hologram is $\Omega = 2 \arcsin\left(\frac{150}{600}\right) \approx 29°$. A higher field-of view is only achievable by a larger hologram plane, up to an angle of 180 ° (respectively a solid angle of 2π). An even larger angle is thus only recordable with subsequent exposures which have to be made at the same time to avoid motion artifacts. In this section, the synchronous recording of an extended field-of-view with planar mirrors is presented. In this context, the holograms recorded with planar mirrors are referred to as mirror recordings to distinguish them from single planar holograms which are masked to produce several sub-holograms with different perspective. Both techniques rely on the principle of hologram perspective (i.e. the change of the 3D holographic image due to reconstructions with different view vectors). Contrary to the aperture-masking technique, mirror recording is capable of actually extending the field-of-view recorded in the hologram beyond the angle defined by the aperture stop of the mother hologram.

To illustrate synchronous pulsed mirror recording, a hologram of an object was recorded which included two mirror perspectives. The hologram reconstructions of the direct and the mirror objects correspond to relief images seen from different perspectives and give additional depth information from an orthogonal view. Multi-view holograms were made with and without speckle projection.

Virtual image

A portrait hologram with two almost orthogonal mirrors was recorded without any structured illumination. Fig 4.14 shows a photograph of the virtual image of the direct and the two mirror objects (the image was assembled from two photographs as an appropriate wide-angle objective was not available). The direct object appears in the centre, the right hand [1] and left hand mirror and their virtual images appear at a higher axial distance from the hologram. The frame of the left hand mirror can be seen. The left hand mirror was smaller than its counterpart and clips the nose partly in this perspective. The hologram contains also doubly-mirrored objects (i.e. mirror images of virtual mirror images) which are not clearly visible from the given perspective; a mirror image of the mirror image of the back of the head is partly visible. The distance

[1] The terms right and left hand are used in the medical convention, i.e. as seen from the patient.

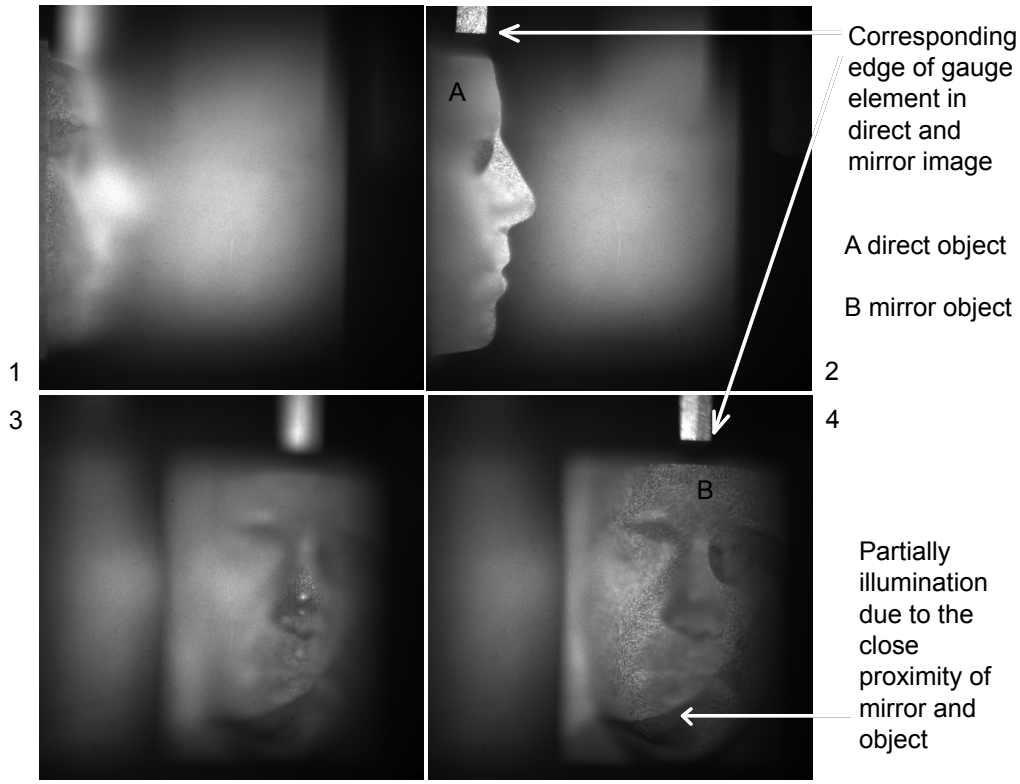

Figure 4.15: Slices of a real image of direct (left) and mirror object (centre). The four slices (1), (2), (3) and (4) are not at equal distances

between head and mirror was approximately half a meter, but no contrast reduction due to limited temporal coherence occurs. A second mirror was used for mirroring the opposite side.

Real image and 45∘-degree views

The virtual produced by a plane mirror can be recorded into a hologram and is reconstructed as a second real image at the apparent location of the virtual image produced by the mirror. The mirror real image is three-dimensional and can thus be used for topometry. It is separated from the mirror real image by twice the distance between object and mirror surface. As the projection screen in the reconstruction set-up has a diameter of only 400 mm, a complete digitalisation of the real image of a human face requires separate scans of the real image volume of the direct and the mirror objects. To avoid the registration problem associated with the combination of separate real image scans (i.e. the determination of the relative orientation of the different real images), a small test object was used (Sec. 4.2.1) to demonstrate 45°-mirroring. Four slices of the real image tomography can be seen in Fig. 4.15.

The mirror normal $\vec{m}$ and its position was derived from the position of direct and mirror real image of a well-defined object. This gauge object has been the corner of an aluminium prism and the mirror normal has been determined to be

$$\vec{m} = \begin{pmatrix} 0.686(1) \\ 0.048(1) \\ 0.725(1) \end{pmatrix} \tag{4.19}$$

where the uncertainty estimates stem from the discretisation error in the hologram tomography.

4.1.5 Discussion

Holographic point-spread-function

The experimental measurement of the holographic point spread function showed no significant deviation from a Gaussian cross-section for most axial distances although the cross-section is more precisely a convolution of a Gaussian curve with a rectangular envelope (the object function of the string) as depicted in Fig. 2.9. The axial dependence of the width of the cross-section of the point-spread function approaches the far-field divergence angle defined by the hologram aperture stop. Although the string has actually been too thick for a direct determination of the Rayleigh length and waist, the measured intensities fit in well with the theoretical predictions (Sec. 2.2). An improved measurement of the PSF could be be realized by a hologram of a back-lit slit since the object wave field scattered by smaller strings is too dim for hologram recording.

Temporal resolution

The method of using perspective views of the virtual image of a spinning disc to is - to my knowledge - novel in the context of pulsed holography. It allows a straight-forward determination of the maximum tolerable velocity for pulsed hologram recording. By variation of the view vector, the size of the visible area of the virtual image of the disc can be changed. The highest visibility is reached when the view vector and the spin axis are parallel: the relative movement of the disc towards the hologram plane is then zero and interference is not hindered by motion (assuming that the surface roughness can be neglected). The visibility of the disc decreases smoothly in regions where the velocity was too high to give a stable interference pattern. The contrast of the virtual image can be approximated by a Gaussian curve with a half-width (half maximum) of 15.4 ± 4 m/s.

This result is surprising as at 7.5 m/s (half a wave length per pulse duration), the hologram should be completely invisible due to destructive interference. In contrast, at a velocity of 15.4 m/s, the pattern intensity has still half its maximum value. The origins of this high visibility are not well understood and future research should be carried on this phenomenon.

Speckle contrast and laser safety

By measurement of of the speckle contrast ratio on aluminium and skin, the minimum average size of a speckle pattern projected onto human skin was determined. A drop to a contrast ratio from 1 down to $\frac{1}{2}$ is measured for the average speckle size of 0.5 mm. It was not possible to obtain speckle patterns with a minimum in the autocorrelation function below 0.5 mm on human skin. A finer speckle field effectively yields a coarser pattern as the fine details smear out on human skin. The minimum average speckle size of the (axial) penetration depth of green radiation of 1.3 mm deduced by Bongartz [Bon02] from literature data [Lip93] is approximately three times the minimum average speckle size of 0.5 mm. Assuming an isotropic random walk, the penetration depth approximately equals the minimum speckle size as two point-like surface points can be separated if the broadening due to diffuse scattering, i.e. the width of their intensity distribution, is smaller than their distance. The small minimum speckle size thus indicates that the scattering in human skin is anisotropic with small-angle (forward) scattering beeing more likely than 90°-scattering. Further studies on the speckle projection onto human skin have to include the influence of the skin type as well as a detailed numerical model of the skin tissue as - for example - described by Osterholz [Ost02].

Intensity measurements indicate that a speckle field with an average size of 0.5 mm can not be used for eye-safe hologram recording. Eye-safe recordings the intensity necessary for hologram recording require that solid angle of the focal spot is larger than the spot size which

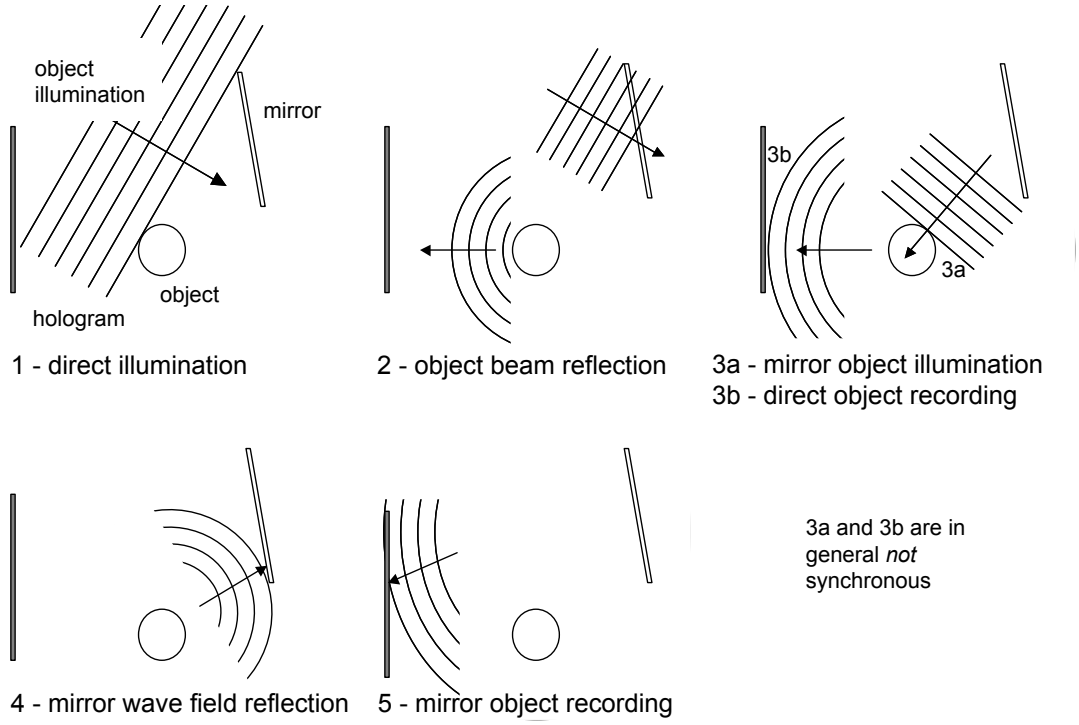

Figure 4.16: Quasi synchronous recording: Direct object illumination and imaging and mirror object illumination and imaging take place within 35 ns. Pulses are actually longer than sketched and all events overlap

project the minimum speckle size (diameter appr. 3 mm) and thus only a *finer* speckle field can met the laser safety regulations. As was shown, such a field cannot be projected onto human skin due to the diffusion into the tissue: The speckles projected with an eye-safe focal spot size are by far too small to give high-contrast on human skin.

As a consequence, an eye-safe speckle projection is inhibited by laser safety regulations and the scattering properties of human skin. To meet laser safety regulations, the intensity of the speckle field has to be approximately two orders of magnitude lower: With the current recording material, holographic recordings are not possible at these intensities.

Mirror recording

With mirror recording, the wave field of an arbitrary object can be recorded from multiple perspectives. The main advantage is the (quasi) synchronous recording. Fig. 4.16 illustrates the propagation of laser pulses with mirror recording: Direct and mirror object interfere with the same reference wave. In the set-up presented, this means that both are recorded within an interval of 35 ns. One should note that the representation of the laser pulses in Fig. 4.16 are depicted too short: Due to the vicinity of the object and the pulse length of several meters, the events 1 to 5 actually overlap, i.e. the scattered radiation from the mirror object reaches the hologram plane while the scattered radiation from the direct object is still impinging on the hologram. Even a 360° field of view on the object would not require moving the set-up or rotating the object with mirror recording. In contrast, in conventional photogrammetry systems, quasi-synchronous recording can only be achieved by using several cameras whereas with laser scanning, a truly synchronous topometry is impossible. Systems with projection or scanning only measure range data from a single camera at a time. A further advantage of mirror recording is the economical use of the large holographic storage capacity. If, in contrast, two distinct holograms were recorded, their relative orientation would have to be known to allow a precise registration and the second holographic medium would have to be covered from the

object illumination. With mirror recording, the second perspective can be reconstructed with the same reference beam parameters, so only one complex-conjugate wave field has to be tailor-made for optical reconstruction. A draw-back of the mirror recording technique is the reduced recording volume: The recordable volume in pulsed holography depends on the coherence length of the pulses. With a 5 m coherence length, the maximum distance of two object points is 2.5 m. Theoretically, one could thus record objects within a sphere of nominal[2] volume of

$$V = \frac{4}{3}\pi R^3 \mathrm{m}^3 \approx 65.4 \mathrm{m}^3 \tag{4.20}$$

Mirror recording reduces the usable coherence length by twice the time-of-flight difference of direct and mirror image. A planar mirror placed at a distance of 100 mm thus reduces the recordable volume diameter by 200 mm. For the topometry of human faces, this is usually not a problem in my set-up due to the high coherence length (5000 mm) of the recording laser.

[2]Neglecting technical restrictions due to, for example, object occlusion.

Figure 4.17: Test object data set as CAM prototype (left), grey-coded relief image (middle) and VRML computer model (right)

4.2 Surface topometry methods

In this section, the spatial precision of the surface reconstruction obtained with different algorithms is presented. Bongartz [Bon02] estimated the accuracy of the reconstructions by measurement of the slope of a reconstructed planar surface: The reconstructed surface was indeed planar to an accuracy of 120 μm. In this thesis, holograms of a non-planar subject were made. The surface of a test object with known shape was recorded and reconstructed by hologram tomography. The semi-heuristic surface finding was done with weighted neighbourhoods. The precision of the measurement was estimated by the deviation of the reconstructed surface from the computer model data set. Additionally, an (data-intrinsic) uncertainty was derived from the figure-of-merit values to estimate the accuracy of the measurement. A quantitative comparison of the different algorithms from hologram deconvolution, multi-perspective gradient averaging concludes the section.

Test object

To evaluate the algorithms, portrait holograms of a test object were made. The test object is a computer-aided-manufacturing (CAM) model produced with an automated milling machine (nominal resolution 10 μm). The data set used for CAM was a previously reconstructed facial model (Fig. 4.17). The model data set consisted of a grid of 200×200 axial coordinates. For comparison with the reconstructed data sets, additional points were linearly interpolated. The material of the model had a similar colour and reflectivity as Caucasian skin, but unlike a real human face contained no intrinsic skin contrast or features like hair. Reconstruction was made with cw radiation at 532 nm. Aberrations due to the wavelength shift were neglected.

4.2.1 Weighted Neighborhoods

The precision of semi-heuristic surface reconstruction with different neighbourhood sizes and weight functions are compared in the following. The semi-heuristic surface finding algorithm calculates a figure-of-merit (FOM) as a function of axial distance from the hologram plane for each lateral coordinate (x, y). The peak value of each function $FOM_{x,y}(z)$ indicates the slice of maximum sharpness, i.e. the axial distance z_0 where the surface of the real image was located. The relief is thus represented by a two-dimensional relief function $z_0(x, y)$ which denotes the

actual surface location. Any actual sharpness measure operates on a lateral neighbourhood of pixels around the central pixel. In this thesis, weight functions were introduced to modify the influence of the neighbourhood pixels to give higher contributions of pixels in the direct proximity. The term neighbourhood denotes the finite number of adjacent pixels. In previous works, [Bon02], all pixels of a square neighbourhood contributed with the same amount to the figure-of-merit.

The width of a weight function is characterized by its standard deviation σ_w. This is the common nomenclature for Gaussian functions which are the only weight functions used in this thesis. Nevertheless, other functions can also be used for weighting. The same applies to the variance which is the figure-of-merit for image sharpness: Any other figure of merit could be used in place of the variance.

The width of the weight function should be less or equal to the neighbourhood size: The neighbourhood size indicates the support of the weight function, i.e. the number of adjacent pixels used for calculation of the figure-of-merit. The Gaussian function has infinite support, so theoretically all pixels contribute to the figure-of-merit of each pixel. The figure-of-merit of a single pixel can thus only be calculated in a number of steps which raises quadratically with the number of pixels in each slice: The time complexity for the analysis of a slice with n pixel is ($O(n^3)$). Truncating the weight function to a finite neighbourhood size reduces the time complexity to a linear dependence ($O(n)$) as each figure-of-merit can be calculated within a constant number of computations.

To evaluate the influence of different weight functions and neighbourhood sizes, the real images of the holograms of the test object were digitized and the data set was analyzed with different weight parameters. The resulting surfaces were compared with the CAM data set of the test object and an intrinsic measure from the semi-heuristic surface reconstruction, the so-called noise-equivalent resolution.

Noise-equivalent resolution

For the semi-heuristic surface finding, the weighted variance

$$f_{wv} \quad = \quad \frac{1}{n} \sum_{\xi,\eta \in N} w(\sqrt{\xi^2 + \eta^2})(I_{(\xi,\eta)} - \mu)^2 \qquad [f_{wv}] = [I^2] \tag{4.21}$$

is calculated for each lateral coordinate for each slice. As the image contrast is highest for real image projections onto in-focus position of the projection screen, the position of the maximum weighted figure-of-merit indicates the position of the surface. Additionally to this the figure-of-merit peak, the figure-of-merit comprises a background signal (Fig. 4.18). The background signal originates from (blurred) out-of-focus projections of distant real image points and subjective laser speckle noise. Contrary to objective speckle noise, which forms on rough surfaces illuminated with coherent radiation as the skin of the object (projected speckles) or the projection screen, subjective laser speckles form on the detector surface itself. The detector surface is in this case CCD-chip of the digital camera which captures the projection screen. The term subjective indicates that the speckle pattern depends on the roughness of the retina, the size of the iris and the focal distance of the eye of a human observer: Different observers (even the two eyes of the same person) see a different, hence subjective, speckle pattern. In contrast, an objective speckle pattern has the same appearance for every observer. Subjective laser speckles form on the CCD if it images a coherently illuminated object, in this case the projection screen illuminated by the real image. The contrast and the coarseness of the subjective speckles depend on the aperture size of the camera objective. The larger the aperture, the less speckle noise is present. To minimize the contribution of the subjective speckle, a high-aperture objective (f1.4 at f=35 mm) was used. Furthermore, 2×2 adjacent camera pixels were added to yield 1024×1024 effective pixels.

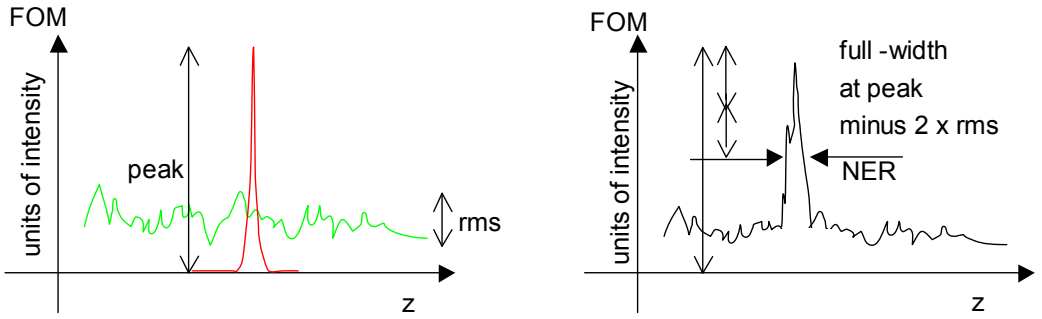

Figure 4.18: Figure-of-merit (right) as superposition of ideal peak (red) and background (green) to define the noise-equivalent resolution (NER)

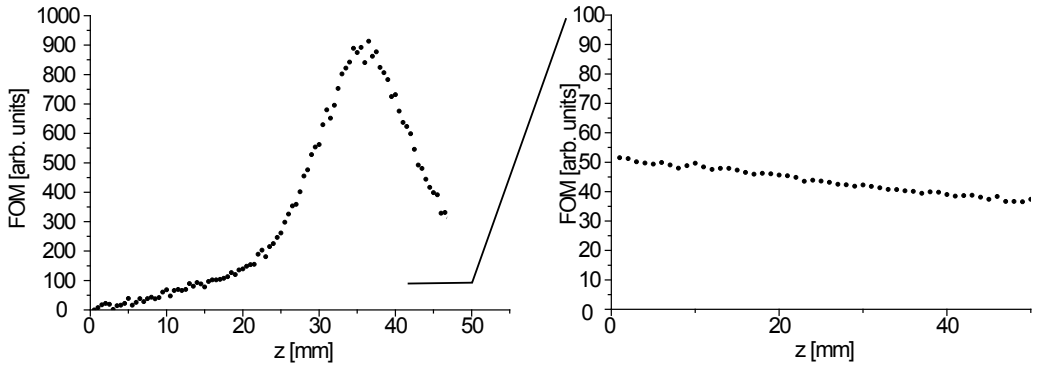

Figure 4.19: Figure-of-merit of a conventional (left) and a class-0 pixels (right, different scale)

As the laser speckle noise and the background from out-of-focal points both reduce the axial resolution and can not be distinguished, an interpretation in the (signal analysis) terms of signal and noise is appropriate: The strength of the combined background and noise component in the figure-of-merit is described by the root-mean-square (rms) deviation of the figure-of-merit from its mean value. Theoretically, the peak itself should be omitted when calculating the mean and the rms value; in practice, the inclusion of the peak has little influence and the difficult problem of separating peak and off-peak was omitted. The signal-to-background ratio SN (in correspondence to the signal-to-noise level in signal analysis) is the quotient of maximum weighted variance f_{wv} and the rms at a given pixel. For quantitative analysis, the noise equivalent (axial) resolution (NER) of a pixel is defined as the *full-width of the figure-of-merit at peak minus twice the rms level* if that value actually exists[3] and zero otherwise. This definition relates the strength of the background signal to a distance in a simple way. Each pixel, i.e. each lateral coordinate has its own NER. The distribution of all NER values characterizes the *accuracy* of a real image digitalisation- in contrast, the *precision* of the surface shape measurement can only be obtained by comparison with the actual surface.

The highest peak of the distribution is called the most frequent NER ($mNER$) and has a characteristic which its full width at half maximum, $FWHM(NER)$. A particular problem of speckle projection is the statistical nature of the pattern - depending on the neighbourhood size and width of the weight function, a number of lateral pixels might be too far away from any speckle edge to allow surface detection. The figure-of-merit of such a pixel shows no distinct maximum (Fig. 4.19) and the NER value is thus zero. Those pixels are referred to as class-0 pixels and their incidence was estimated from the NER histogram. The slice distance Δz can

[3]The figure of merit peak might be smaller than twice the rms value

be chosen arbitrarily down to the scale of the wave length (1 μm nominal resolution of the linear positioning stage). Both axial slice distance and the width of the figure-of-merit peak determine pose a lower limit on the effective axial resolution. The axial slice distance was thus chosen small enough to allow optimum localization of the maximum figure-of-merit, but on the other hand as large as possible to minimize memory requirements and computational costs.

Surface matching

For the estimation of the precision of the surface measurement, a well-known surface shape was compared to the experimentally determined relief obtained by hologram tomography. The real image of the test object was digitized with a slice thickness of Δz =0.200(1) mm and an effective pixel size of Δx=0.241(1) mm at 1024×1024 pixels. The histogram of the noise-equivalent resolution (NER) of the reconstruction was calculated to give the most frequent noise-equivalent resolution ($mNER$) and the width of the peak in the NER histogram.

To match the original and reconstructed relief, the relative orientation between them must be known. The problem of finding a suitable rigid coordinate transformation which transform one of the surfaces onto the other, the so-called registration, is non-trivial. It requires the definition of a distance measure for two surfaces which are defined by a finite number of points. If this distance between the (transformed) surface and its counterpart is zero or, at least, has a global minimum, one can assume that the transformation indeed registers one surface onto the other. The Hausdorff distance [ASCE02], for example, can be used as such a distance measure. It is defined as the sum of the distances from all points on one surface to the nearest point on the other surface. This definition implies that the Hausdorff distance of surface A regarding surface B is not necessarily the same as that of B regarding A. This distance has to be minimized under variation of the relative orientation of the two surfaces, i.e. a rigid transformation which includes six degrees of freedom to describe a translational and general rotation. A complete least-square optimization for all six degrees of freedom for optimum match was omitted in this thesis. Instead, the test object was aligned parallel to the hologram plane before hologram recording and only the lateral and the axial positions were determined by least-square optimization. This partly matching was achieved by varying the translation vector to give a minimum in the summed squares of the axial distances between the reconstruction and original model. For this simplified matching process, the original data had been interpolated to the same resolution as the reconstructed model. One of the three rotational degrees was matched manually by rotation of the reconstructed data around the z-axis to align the model edge parallel to the y axis. This algorithm cannot align the two models correctly if they are tilted axially, so the orientation of the test object was carefully checked before the exposure. The resulting estimates for axial and lateral resolution are thus upper limits on the actual deviation. The surface deviations determined by the partial matching process were ranged between 100 μm and -in one case- 300 μm (mean value 129 μm) for subsequent matching of different exposures with unchanged parameters, indicating that the surface matching process was below the quantization error from the lateral pixel size (200 μm).

A complete surface matching (a so-called surface registration) of surface shapes measured with the set-up described in this thesis was made by A. Nüchter [Nüc02] who implemented an algorithm of iterative closest points (ICP) developed by P. Besl and N. McCay [BM92] for the registration of 3D shapes. The ICP algorithm aligns two point clouds by finding a rigid transformation (i.e. an arbitrary translation and rotation) which minimizes the sum of a certain error function. The error function is the sum of the geometrical distances of a number of point pairs. Obviously, the choice of corresponding point pairs is of importance to the error function. The correct assignment of point pairs would require the prior knowledge of the rigid transformation. To overcome this problem, the ICP algorithm starts with an initial guess of the rigid transformation which yields an estimate of the correct error function. It then finds the

rigid transformation to minimize this error function estimate. This rigid transformation then serves to guess another error function estimate. The algorithm finally converges to the correct rigid transformation. For a comparison of different semi-heuristic surface finding algorithms, however, such an iteration has been omitted since the outliers (i.e. points which were found far from the surface) strongly influenced the iterations. For the comparison of the different hologram tomography algorithms, however, the CAM and the measured surface relief were only partially matched and the average magnitude of the axial distance δz between original and reconstructed surface was determined :

$$\delta z = \langle |z_1(x,y) - z_2(x,y)| \rangle \tag{4.22}$$

$$= \frac{1}{n} \sum_{x,y} |z_1(x,y) - z_2(x,y)| \tag{4.23}$$

where the summation denoted by $<,>$ is carried over all pixels of the relief.

Neighborhood size

Any contrast-detection algorithm works on a number of pixel. A single pixel has no contrast in itself, but only within its neighbourhood. A large neighbourhood restricts the lateral resolution of the algorithm but increases the axial surface localization, as Bongartz [Bon02] pointed out. His experiments indicated that the optimum neighbourhood size is appr. 7×7 pixels.

With speckle projection, a neighbourhood ideally covers exactly one speckle edge. As the speckles are statistically distributed, some neighbourhoods inevitably contain more than one, others no speckle edge at all. With weighted neighbourhoods, one can lower the influence of distant speckle edges by weighting with a window function. A Gaussian window function is characterized by its variance σ_w. The calculations were restricted to adjacent pixels in a square $s_L \times s_L$ neighbourhood ($s_L = 3, 5, 7, 9$) and was truncated to zero outside a square of side length s_L around the central pixel. The size s_L of this square is called the (lateral) neighbourhood size. A plain calculation of the figure-of-merit can be seen as weighting with an infinitely broad Gaussian, i.e. $2\sigma_w \to \infty$. The average intensity of each pixel was subtracted from the slices before semi-heuristic surface detection to compensate the non-isotropic scattering characteristic of the diffusor screen: As the scattering characteristic of the diffusor screen follows approximately Lambert's law[4], the central region of the diffusor screen appears slightly brighter than the edges.

Fig. 4.20 shows the statistical distribution of the axial deviation from a semi-heuristic surface reconstruction with different neighbourhood sizes.

To evaluate the influence of the width of the weight function, a heuristic surface reconstruction with different neighbourhood sizes from 3×3 to 9×9 pixels with $\sigma_w = 3$,4 and 5 pixels (the choice of integer numbers for σ_w is arbitrary) and constant weights ($\sigma_w = \infty$) was calculated. Tab. 4.1 shows the results of the analysis. The most frequent noise-equivalent resolution ($mNER$) and the width of the corresponding peak at half-maximum $FWHM(NER)$ were included. Their values and uncertainties were determined by a least-square (Gaussian) peak fit to the NER distribution. As the matching was only partial, the last column in 4.1 should be used for comparison between the different algorithms and gives an upper limit of the axial resolution. Additionally, the incidence of class 0 pixels was estimated by the NER histogram: If the NER value was ill defined as twice the rms exceeded the FOM peak, the pixel was assigned to the group of class-0 pixels. They were included in the average deviation calculation. At neighbourhood sizes of 3×3 pixels, the class-0 pixels cannot be distinguished from pixels with extraordinarily thin figure-of-merit peaks. Increasing the width of the weight function signifi-

[4] A surface scatters with an intensity proportional to the cosine of the view vector and surface normal according to Lambert's law

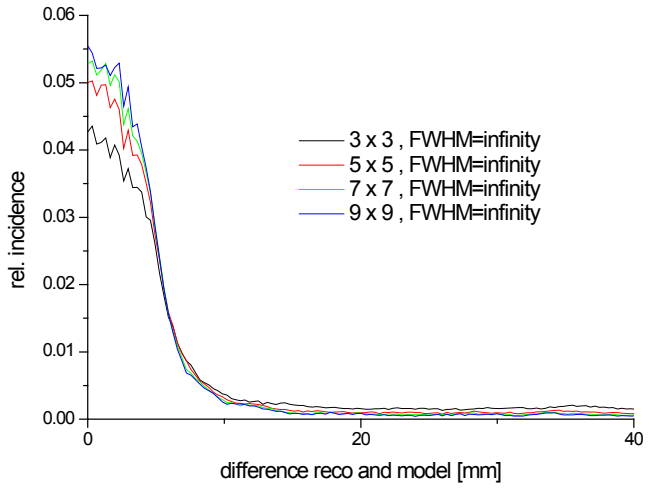

Figure 4.20: Statistical distribution of the axial deviation between reconstructed and original surface at different neighbourhood sizes

$2\sigma_w$	s_L	*mNER* [mm]	FWHM NER [mm]	rel. inc. class 0	mean. deviation [mm]
3 pixels	3×3	N.A.	N.A.	N.A.	8.97
	5×5	2.48(2)	1.6(1)	12.1	3.57
	7×7	2.99(3)	1.8(3)	3.4	2.81
	9×9	2.97(3)	1.4(1)	3.4	4.21
4 pixels	3×3	N.A.	N.A.	N.A.	10.01
	5×5	2.47(2)	1.4(1)	17.5	5.01
	7×7	2.54(2)	1.5(1)	7.2	3.02
	9×9	3.01(3)	1.4(1)	6.7	2.76
	11×11	3.31(5)	1.3(2)	3.7	2.90
5 pixels	3×3	N.A.	N.A.	N.A.	10.49
	5×5	1.72(3)	1.5(1)	15.9	5.96
	7×7	2.56(2)	1.6(1)	6.2	3.66
	9×9	3.07(4)	2.0(1)	6.7	2.76
	11×11	3.31(3)	1.3(2)	6.1	2.80
∞	3×3	N.A.	N.A.	N.A.	11.37
	5×5	1.84(3)	1.9(1)	13.3	7.91
	7×7	2.71(2)	1.5(1)	4.8	6.37
	9×9	3.19(4)	1.6(1)	2.6	5.54

Table 4.1: Different neighbourhood size and weighting functions in FOM calculation

cantly lowers the incidence of class 0 pixels as more speckles lie within each neighbourhood. The average deviation of reconstructions with weighted neighbourhoods is lower than without weighting ($\sigma_w = \infty$). The average NER increases with neighbourhood size, indicating that a larger neighbourhood results in a broader FOM peak and/or a higher rms. This can also be explained with the larger number of speckles within each neighbourhood even though they have less influence due to the weights. Best agreement between model and reconstruction is found with a FWHM of four to five pixels when calculation is carried out in a neighbourhood of at least 9×9 pixels. Larger neighbourhood sizes tend to have little effect on the average deviation.

The achieved average deviation is high compared to the sub-mm requirements in the medical context. Since it is impossible to increase the resolution further by projecting a finer speckle pattern (Sec. 4.1.3), one cannot improve the resolution on human skin by another projection pattern. For technical applications, however, a better surface localization with a smaller pattern is possible.

4.2.2 Deblurring

For numerical image deblurring, two methods were implemented: Inverse filtering and iterative deconvolution (Sec. 3.4). Both require the knowledge of the PSF of the system. A spherical diaphragm (concentric to the hologram center) masked the reconstruction beam. The hologram is thus elliptical and the point-spread-function is approximately (Sec. 4.1.1)

$$h(x,y,z) = \frac{1}{w^2(z)} \exp\left(-2\frac{(\epsilon x)^2 + y^2}{w^2(z)}\right) \tag{4.24}$$

$$w(z) = w_0\sqrt{1+\left(\frac{z}{z_R}\right)^2} \tag{4.25}$$

where ϵ is a positive number to account for the elliptical hologram shape with $\epsilon = 1$ for spherical holograms. In the given set-up, $\epsilon = 1/\cos(66°) = 2.458$. For iterative deconvolution and inverse filtering, the convolution integral of the real image and PSF based on a discrete representation of both have to be calculated. The FFT algorithm requires that the discrete values of the real image and h are loaded into the random-access-memory (RAM) of the digital computer. Therefore, the available memory limits either object size or resolution. For the following sections, the volume was restricted to $256 \times 256 \times 256$ volume elements (voxels). At the dimensions required to cover a human head, this corresponds to voxel dimensions around 1 mm^3.

Inverse Filtering

The real image of the hologram of the test object (4.2.1) was digitized with a slice thickness $\Delta z = 0.5$ mm. The effective pixel size was $\Delta x = 0.241(1)$ mm. To reduce memory consumption, the slices were re-scaled down to 256×256 pixels by addition (i.e. four adjacent 12-bit greyscale values from the camera pixel were added to one 16-bit image pixel) to an effective pixel size of $\Delta x = 0.964(1)$mm. The hologram plane was illuminated in an elliptical region with semi-major axis lengths of $111(1)$ mm and $275(1)$ mm, respectively. Fig. 4.21 shows one of the real image projections before and after deconvolution by inverse regularized filtering with two different regularisation parameters γ (Eqn. 3.8). The out-of-focus intensity is significantly reduced. To illustrate the effect of the inverse filter, the maximum intensity for each lateral position was determined. In correspondence to the full-width at half maximum of the NER, the width (FWHM) of this maximum intensity was determined for all lateral coordinates. Fig. 4.22 shows three typical distributions of the axial intensity peak width for undeconvoluted real image and the dependence of the width on the regularisation parameter. For $\gamma = 0.01$, an axial intensity width of 68 mm has the highest incidence. With $\gamma = 0.001$, the axial intensity width

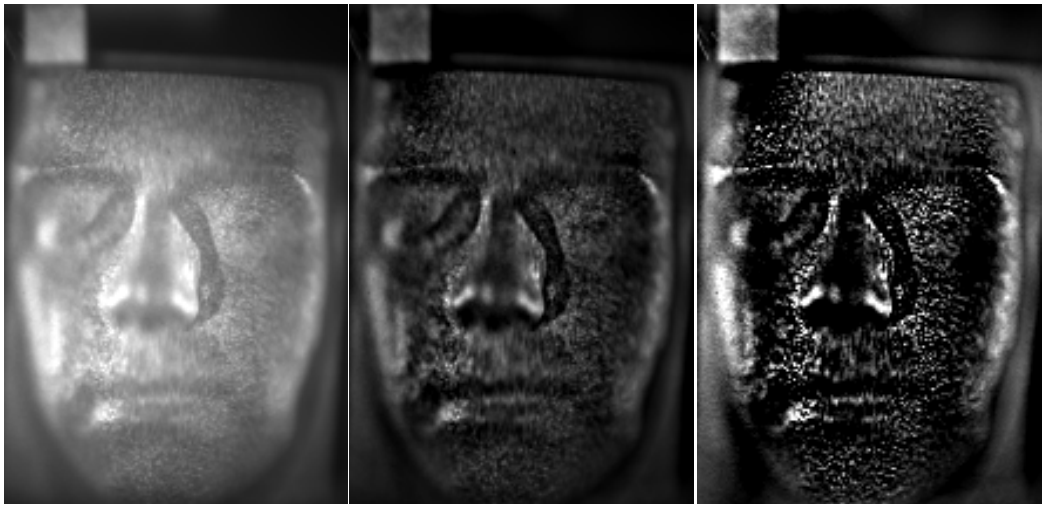

Figure 4.21: Slice from hologram tomography before (left) and after inverse filtering with regularisation parameter $\gamma = 0.01$ (middle) and $\gamma = 0.001$ (right)

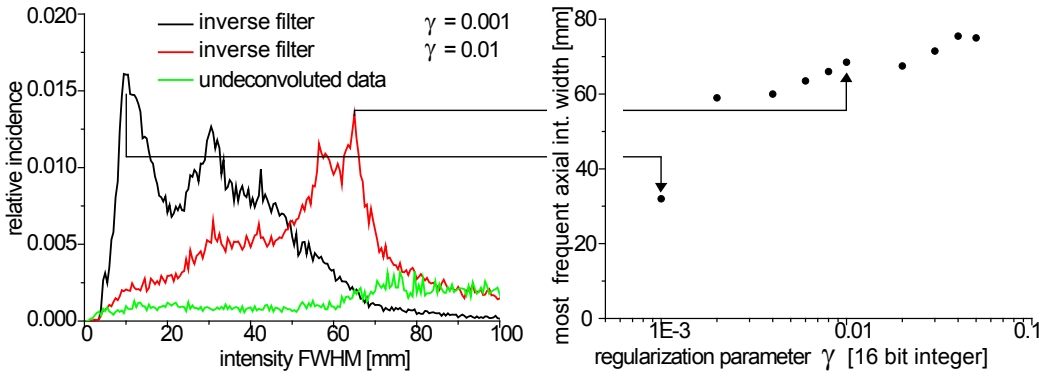

Figure 4.22: Histogram of the axial intensity FWHM (bin size 0.5 mm) from undeconvoluted and inversely filtered real image volume (left). The most frequent FWHM is plotted versus the regularisation parameter (right)

	γ [intensity(0...4095)/pixel]	δz [mm]
undeconvoluted	-	9.24
inverse filter	0.01	7.89
inverse filter	0.001	12.00

Table 4.2: Deconvolution improves semi-heuristic surface reconstruction for some choices of regularisation parameter

which occurs most frequently is 32 mm. Although this seems to indicate a superior deblurring with lower regularisation parameter, the accuracy of the surface reconstructions is actually not improved with low γ: This was verified by comparing the reconstructed surfaces with the original data set as described in the preceding section. From this surface matching, the average axial deviation δz of reconstructed and original surface points was calculated (Tab. 4.2). For a regularisation parameter around $\gamma = 0.01$ one gets indeed a better match of original and reconstructed surface. At low regularisation parameter, however, the average axial deviation increases. The functional dependence is unclear: The optimum regularisation parameter seems to depend on the object itself, making inverse filtering unsuitable for the surface topometry of unknown objects. Gonzalez and Woods have described an iterative procedure to optimize the regularisation parameter ([GW93], pp. 286), but their algorithm is unsuitable for hologram tomography as it assumes two-dimensional images.

The results obtained with weighted neighbourhood semi-heuristic surface reconstruction with smaller slice thickness and smaller lateral pixel sizes yielded better surface reconstructions than the inverse-filtered real image intensities which had to be made at a coarser resolution. However, with inverse filtering, the average deviation of the reconstructed surface was lowered with appropriate regularisation parameter, indicating an improved precision.

Iterative deconvolution

Spatial frequencies which were removed during the imaging process cannot be reconstructed by inverse filtering. The use of structured illumination is thus complementary with inverse filtering for three-dimensional measurement. Eye-safe portrait holography is, on the other hand, only possible with unstructured illumination. Therefore with iterative deconvolution, an alternative algorithm for image deconvolution has been implemented which is capable of out-of-band extrapolation. Out-of-band extrapolation means that theoretically, it can restore the spatial frequencies which are not transmitted due to the missing cone (Sec. 2.2.2). This enables one to reconstruct all spatial frequencies even from a portrait hologram without structured illumination. In practice, the presence of noise hinders a restoration of those spatial frequencies. To minimize the influence of noise, all experiments were made with structured illumination to make the results comparable to the other techniques.

Iterative deconvolution applies subsequent corrections to construct an approximation to the unblurred object function. At each iteration, the blurring is simulated (realized as a multiplication with the point-spread-function in Fourier space) and the result is compared with the actual measurement. A correction term is calculated based on the deviations between measured and simulated intensities. Algorithms differ by the way the correction is applied via back-projection to the object approximation (Sec. 2.2.2).

An iterative deconvolution algorithm (Sec.2.2) based on the expectation-maximum algorithm of J.A. Conchello [Con95] was implemented for this thesis (Sec.3.4.2). Conchello proved that the algorithm is capable of band extrapolation. The algorithm has been adapted to combine multiple measurements of the real image intensity of the same object which can - for example - be obtained by mirror hologram recording (alternating iterative deconvolution, Sec. 3.4).

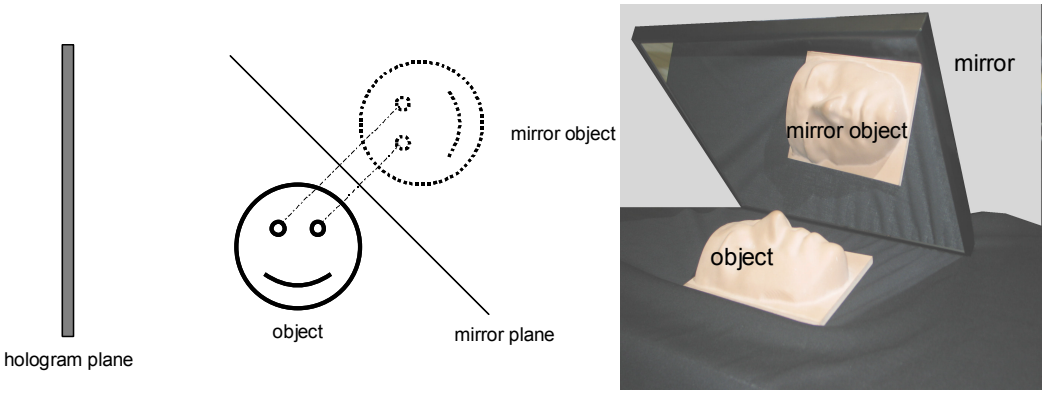

Figure 4.23: Geometry for recording two perspectives of the test object with a plane mirror

A hologram from the test object (Sec.4.2.1) was made at a slice thickness of $\Delta z = 0.955(1)$ and 512×512 pixels per slice at an effective pixel size of $\Delta x = \frac{1}{2}\Delta z = 0.4775(10)$mm. A plane mirror was placed next to the object to record a second perspective: The mirror enclosed an angle of appr. 45° with the hologram plane (Fig. 4.23). The hologram thus includes two approximately orthogonal perspectives of the test object: One direct view of the profile and one mirror view of the front. The actual position and the orientation of the mirror was deduced directly from the real image of the test object: The corner of an aluminium square was identified in the hologram tomography of the direct as well as in the mirror region of the hologram tomography. From the two coordinates of the corner, the position of the mirror and the direction of its surface normal mirror were deduced (Sec. 4.1.4). Fig. 4.24 (left, middle) shows slices of the real image intensities of the direct and the mirror object. In the left column, the test object appears frontally - this is the real image of the mirror object. The direct real image gives a side view of the test object.

It was numerically mirrored onto the location of the other view (middle column) to allow the iterative deconvolution without any transformation steps. This effectively reduces the number of computation steps for reconstruction. The blur from the point spread function appears as horizontal cones in this image volume, the blur from the mirror point-spread-function causes axial cones. After 50 alternating iterations (i.e. 25 iterations with the physically mirrored real image volume and the axially blurring point-spread-function, each followed by an iteration with the numerically mirrored real image volume), the object function approximation reaches a stationary point. The mean squared difference between measured and simulated real image intensity alternates with the two different point spread functions/hologram tomography volumes. Both the mean squared difference for the side view and the front view approach an asymptotic value: After approximately 50 iterations, the change in mean squared intensity difference per double iteration drops to 10^{-4} of the initial change.

Fig. 4.24 shows the approximation of the real image volume (i.e. the iteratively deconvoluted real image) at different axial cross-sections. The approximation has a strongly reduced intensity in areas which were not included in either of the two real image volumes. This can be seen near the 'nose' of the test object. In a horizontal stripe where the intensity in both real image volumes was high, the intensity in the deconvoluted image is also high. The out-of-focus intensity drops quickly, indicating that the two-view deconvolution indeed causes a blur removal.

However, a surface reconstruction from the locations of maximum intensity was impossible without contrast-detection (i.e. additional semi-heuristic surface finding). This might be due to anisotropic scattering from the skin surface: When the object is seen from two orthogonal perspectives, the same object point might scatter a different intensity into different directions. Furthermore, object points occluded in one of the real image reconstructions also cause an

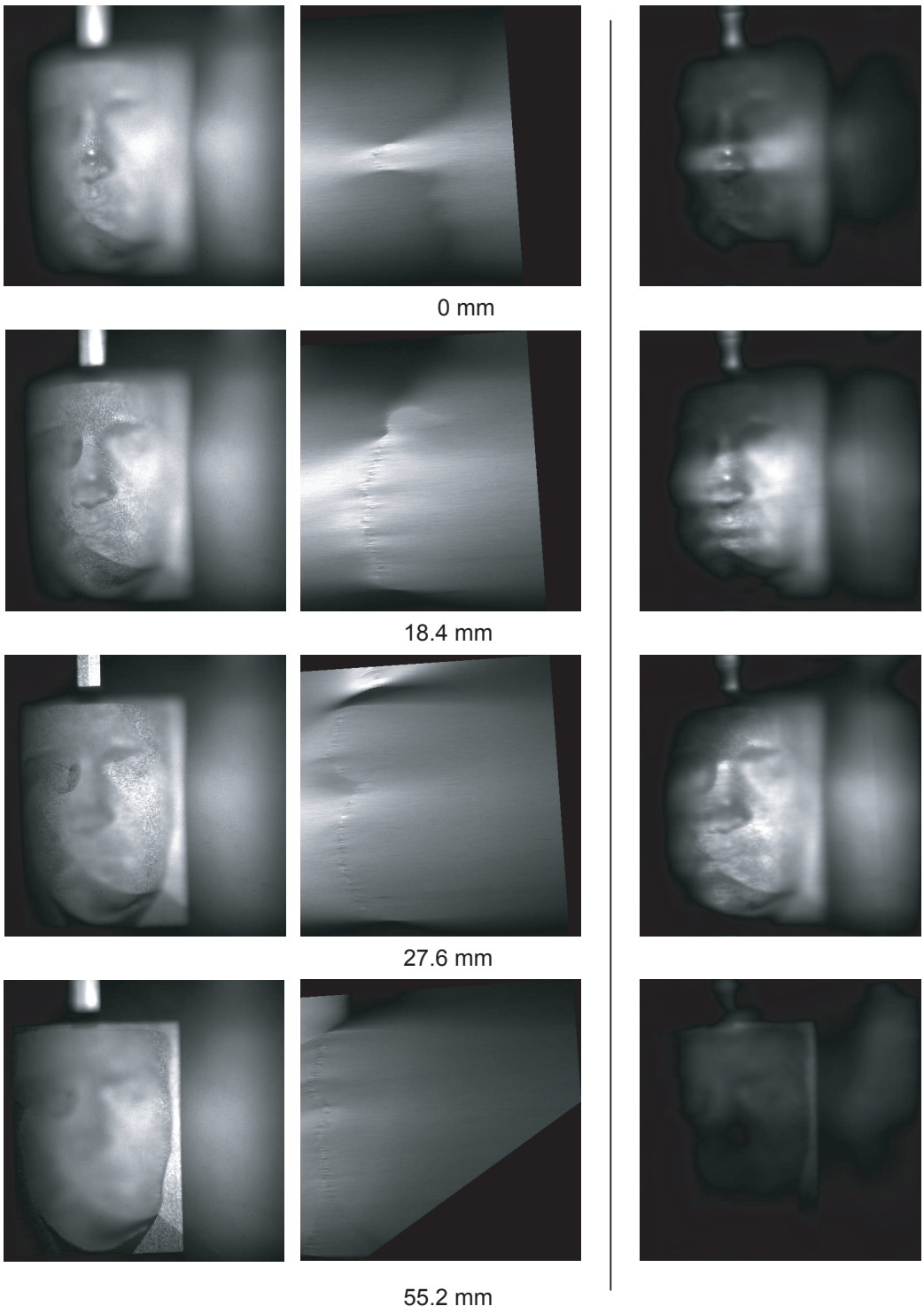

Figure 4.24: Object approximation (right) from alternating iterative deconvolution of two views of the real image volume (left,middle)

incorrect error estimate. An extension of the alternating deconvolution to more than two views should further enhance the quality of the deconvoluted images as occlusions of a particular point then occur less frequently.

4.2.3 Multiple perspective gradient averaging (MUPEGA)

Eye-safe, unstructured illumination results in portrait holograms with a high lateral resolution. Even small details as single hairs are present in the real image reconstructions. However, unstructured illumination yields semi-heuristic surface reconstructions with poor axial resolution, especially in the absence of high spatial frequencies in the object. Even with speckle projection, the axial resolution is several orders of magnitude higher than the diffraction limit defined by the Rayleigh length of the real image of a point source. In order to increase the axial resolution even with eye-safe illumination, I have developed the technique of multiple perspective gradient averaging (Sec. 2.4). From a planar (mother hologram), several sub-holograms are created by partial illumination. The low axial resolution of the sub-real images results in a high depth of field of the real image projections: For spherical holograms, the Rayleigh length increases quadratically with the inverse of the hologram diameter (Eqn. 2.42). For gradient averaging, the lateral gradients of multiple sub-hologram real images are projected onto a screen at a fixed axial position. The resulting averaged gradient magnitude values comprise mainly the gradients from in-focus features, as out-of-focus features cancel out (Sec. 2.4). A complete hologram tomography with MUPEGA is then created from the averaged gradient magnitude at different axial distances (slices) of the projection screen.

For an experimental verification of the MUPEGA hologram tomography, a spherical aperture on a disc (Fig. 3.10) with a fixed diameter $D = 32$ mm rotated around an axis at a radius of 65 mm to generate the real images of the sub-holograms (Sec. 3.3.1). The real image of the test object was digitized using the multiple-perspective gradient-averaging (MUPEGA) technique. Each averaging included 16 sub-hologram perspectives. The effective pixel size was $\Delta x = 120(1)\mu$m. The Rayleigh length from the sub-holograms was $z_R = 235\mu$m, the maximum angle between the view vectors of two sub-holograms was Ω =12.44°, corresponding to a geometrical axial resolution (Sec. 2.4.2) of $z_P = 815\mu$m. The axial slice distance was chosen $\Delta z = 500\mu$m. The average gradient magnitude values of the digitized slices were post-processed with a Gaussian blur filter[5] (width 4 pixels = 0.481 mm). This increases the gradient intensity in the interior of the projected speckles which appear outlined in the gradient averaged slices. Fig. 4.25 shows a hologram tomography of a plane 5 mm before focus, in-focus and 5 mm after focus with and without post-processing filter. The reconstructed surface was built from the average gradient magnitude by connecting the voxels with maximum gradient magnitude: For each lateral position, the surface relief is defined by the axial coordinate with the highest average magnitude strength.

The resulting relief has a certain surface roughness. A hologram tomography from the test object (4.2.1) was calculated with 16 perspectives. Using more perspectives did not result in an improved deblurring of out-of-focus contributions. Each of the 16 sub-holograms has an overlap of appr. 5.7° with the two adjacent sub-holograms. Fig. 4.28 shows the grey-coded relief of the model data set. The surface was constituted by the points with maximum averaged gradient-magnitude. Three cross-sections along the xz plane through the relief are shown, bright points correspond to a high average gradient magnitude. The third cross-section shows the trace of a scratch on the projection screen: The gradient at the scratch edge was high independently from the real image. The high-gradient trace parallel to the axial coordinate axis z masks the gradient information from the surface, leading to a spike in the surface reconstruction. The most frequent

[5] A Gaussian blur filter is a convolution with a discrete, two-dimensional Gaussian curve

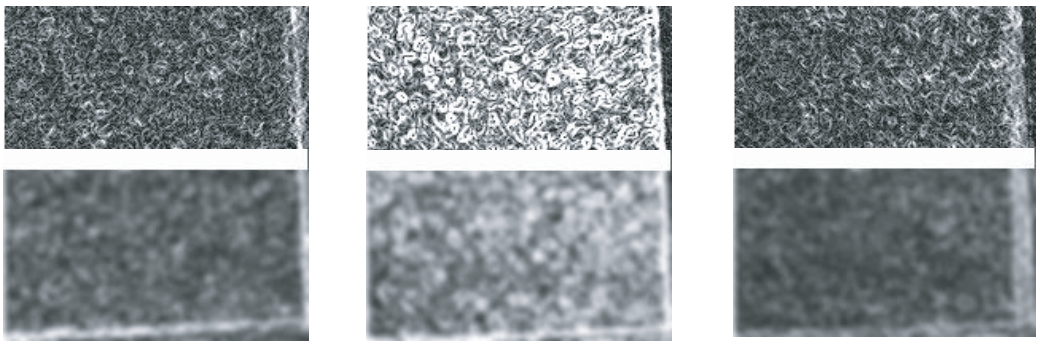

Figure 4.25: Upper row: Averaged lateral gradient magnitude calculated from 16 sub-holograms with different axial positions of the projection screen: 5 mm before (left), in (middle) and 5 mm behind the real image of a planar surface. Lower row: With post-processing filter

noise-equivalent resolution of the reconstruction ($mNER$, see Sec. 4.2.1) was

$$mNER = 3.06(6)\text{mm} \tag{4.26}$$

$$FWHM(NER) = 2.0(2)\text{mm} \tag{4.27}$$

Fig. 4.27 shows the NER histogram and a graphical representation of the NER values. For quantitative analysis, both surfaces were matched by minimization of the axial distance magnitude as described in Sec. 4.2.1. The average magnitude of the difference between the two surfaces δz was numerically evaluated to be

$$\delta z = 1.95\,\text{mm} \tag{4.28}$$

The histogram of the NER values are depicted in Fig. 4.26. If one assumes that the surface distances are distributed normally, a least-square fit yields a standard deviation of

$$\sigma_z = 0.89(4)\,\text{mm} \tag{4.29}$$

The distribution of the axial distances is not exactly described by a normal distribution. The histogram shows an asymmetric deviation broader than the normal distribution for negative axial differences (Fig. 4.26, right). A small axial tilt might be the source for this deviation: Negative axial distances occur more frequently in the upper left region of the difference relief (Fig. 4.26, left).

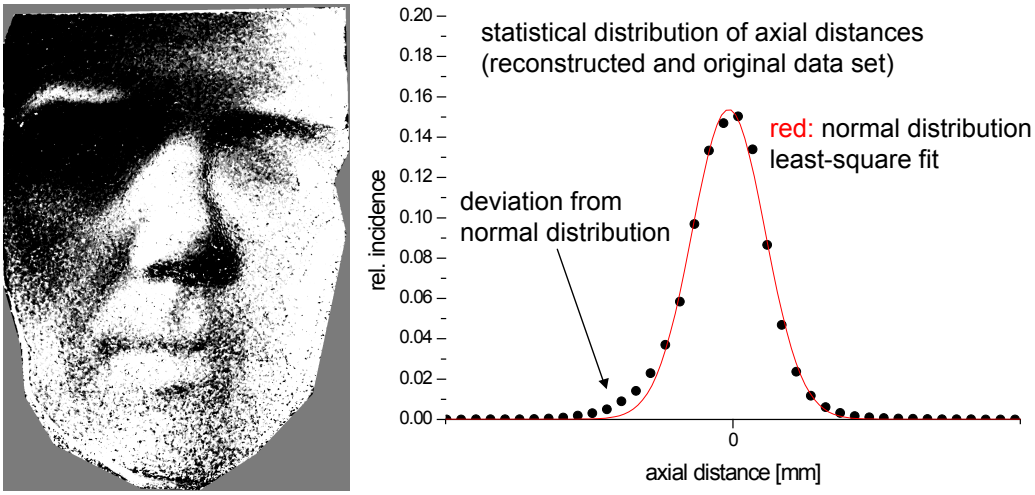

Figure 4.26: Left: spatial distribution positive (bright) and negative (black) deviation of the reconstructed surface from test object surface. Right: Fit of a normal distribution to the histogram

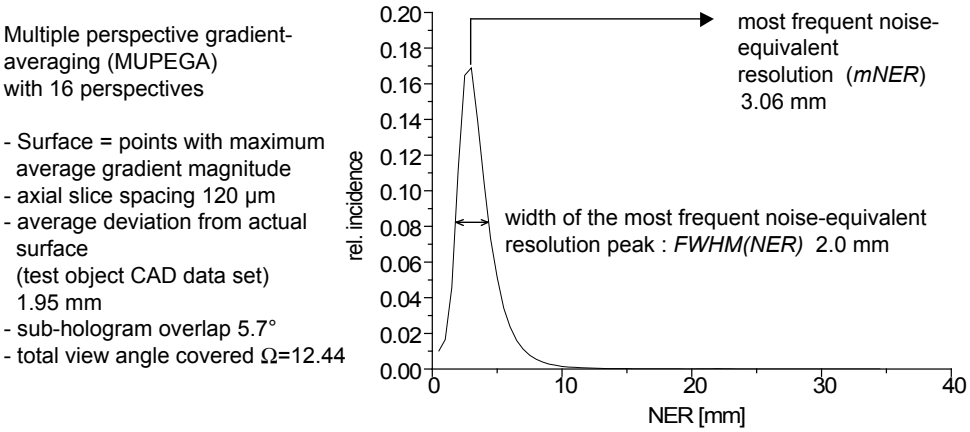

Figure 4.27: Histogram of the noise-equivalent resolution of a multiple-perspective gradient averaging hologram tomography of the test object

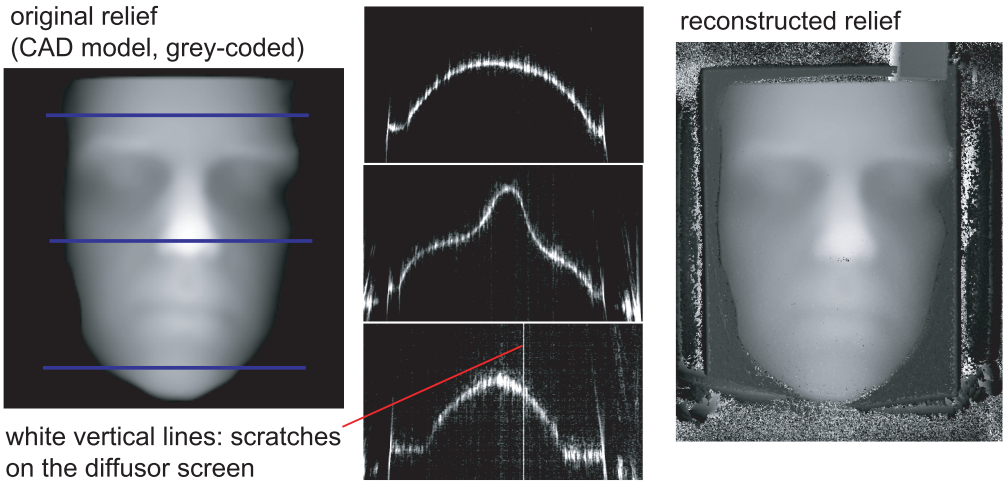

Figure 4.28: Original (left) and reconstructed (right) test object surface. Three top-view cross-sections of the magnitude of the averaged lateral gradient from 16 perspectives (centre) correspond to the blue lines.

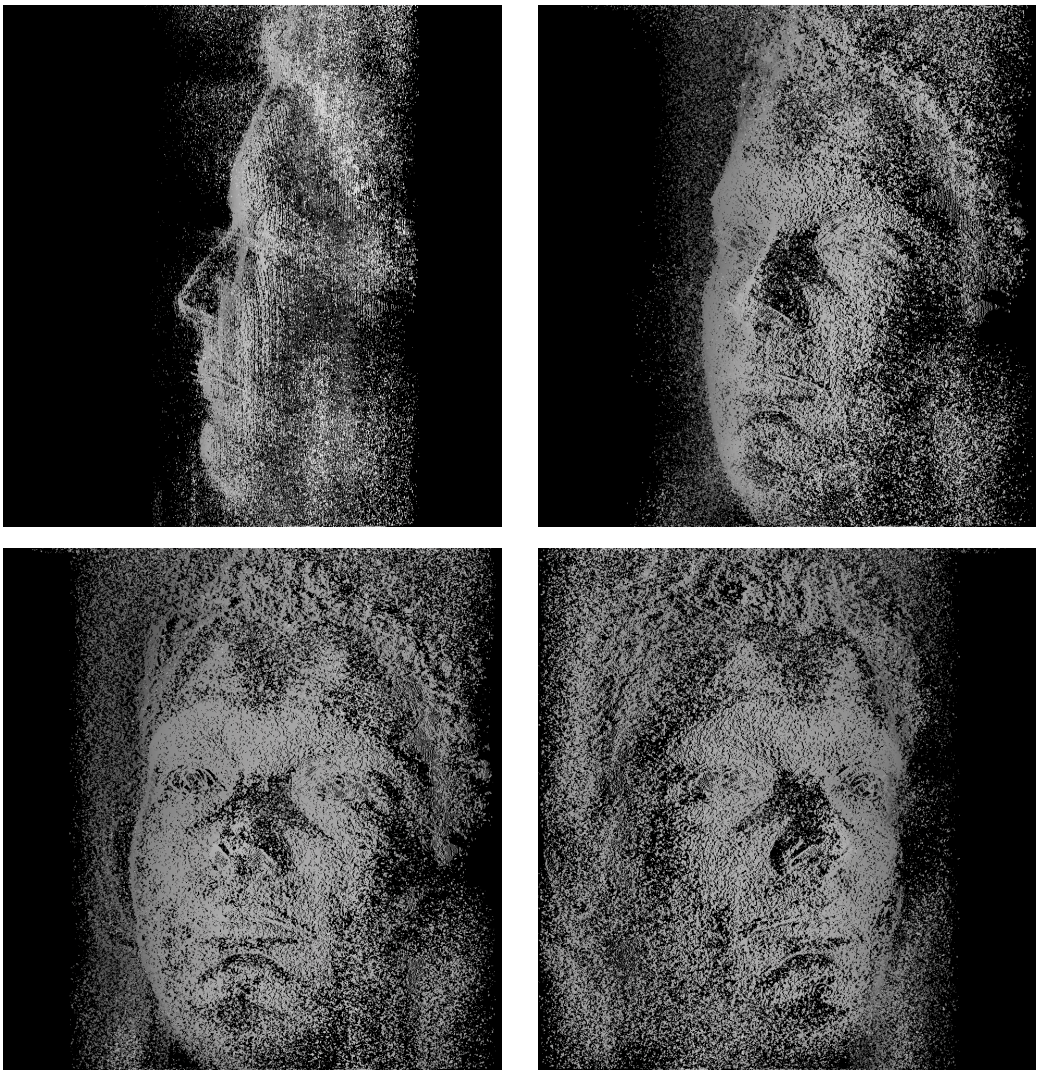

Figure 4.29: Different views of a 3D point cloud model obtained with MUPEGA from an eye-safe portrait hologram

Homogeneous illumination

Without structured illumination by stripe or speckle projection, the real image can contain regions with low contrast which make heuristic surface reconstruction at high axial resolutions impossible. On the other hand, object illumination with an unfocused beam and diffusor plates is desirable in medical applications since the laser safety regulations allow eye-safe hologram recording only with illumination by extended laser sources (Sec. 4.1.3). To illustrate the use of the MUPEGA technique for surface topometry, a surface reconstruction was obtained from a portrait hologram recorded with eye-safe, unstructured illumination. The human skin has a low lateral contrast, but since the MUPEGA is sensitive to even low-contrast features, a surface localization was achieved.

Fig. 4.29 shows a three-dimensional model of the points of maximum gradient strength. The points were not connected to form a contiguous surface since too many outlying points were found due to a high noise in the real image scans. A comparison of the profile view with a photography is given in Fig. 4.30.

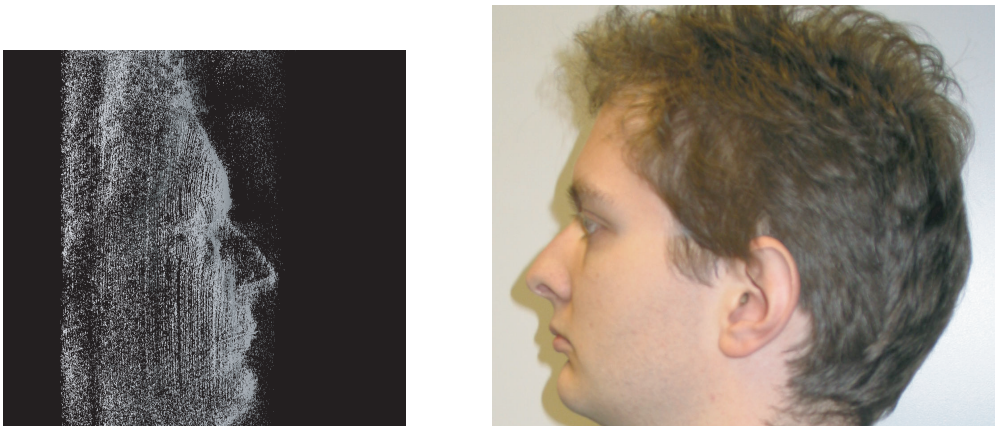

Figure 4.30: Profile view of point cloud model (left) obtained with MUPEGA from an eye-safe portrait hologram of a volunteer and a corresponding photography (right)

4.2.4 Discussion

Weighted neighbourhoods

The use of the weight functions for figure-of-merit calculations allows one to identify the lateral resolution by the width of the weight function. Square artifacts resulting from the shape of the neighbourhoods can be significantly reduced. This is illustrated in Fig. 2.13 where semi-heuristic surface reconstruction algorithm was applied to a simulated real image. The semi-heuristic reconstruction without weight function shows significant artifacts. The lateral resolution δx of a (weighted) semi-heuristic surface reconstruction is defined by the width of the weight function. The intrinsic noise-equivalent resolution (NER) of the semi-heuristic surface finding algorithm gives an estimate of the accuracy of the reconstruction. The precision can only be determined by a comparison of the reconstructed surface with the actual surface shape, for example from the hologram of a well-known test object. Accuracy and precision of the reconstructions lead to an estimate for the axial resolution which is much above the diffraction limit defined by the Rayleigh length. The accuracy and the precision of the surface reconstructions are worse than the values reported by Bongartz [Bon02] which might be due to the more realistic test object used in this thesis. However, the axial resolution can be significantly improved by using a weighted figure-of-merit instead of square neighbourhoods.

Deblurring

The experiments conducted indicate that deblurring can successfully be used to reduce out-of-focus intensity in projections of holographic real images. Despite of the limitations on the resolution imposed by memory consumption of the algorithms, a significant reduction of out-of-focus intensity was shown. Inverse filtering can thus be used to improve the quality of the real image projections if an appropriate regularisation parameter is used. The optimum choice of γ depends on the signal and its noise spectrum. Several methods for guessing a value for γ are described in literature [GW93]. They assume certain properties of the imaging system and do not seem to yield valid results for holography.

The memory requirements for a high-resolution hologram iterative deconvolution exceed the currently available personal computer architecture by only a modest factor. The storage of the real image intensity with $1024 \times 1024 \times 512$ voxels at floating-point precision (8 bytes per pixel for a complex number) requires approximately 4 GBytes of random access storage (RAM). At the time of writing, no such machine was available to the author[6], but mid-term

[6]The 32-bit address space of the industry standard limits the usable memory to 1.8 Gbyte.

technical developments are likely to overcome these limitations. Even without any technical advances, a number of optimization schemes could be used to lower memory consumption:

- The real image intensity (and the point spread function) is a real number. Its Fourier transform has a discrete symmetry. Storing its Fourier transform thus only requires half the RAM.
- The point spread function itself possesses even more symmetries: It and its Fourier transform could be stored as an analytical expression.
- With the appropriate FFT scheme, random-access memory can be substituted by sequential memory (i.e. hard-disc space) and an appropriate algorithm [Pre92] at the cost of computational efficiency

The overall resolution of the deconvoluted models is still inferior to the that of the models from direct (weighted) heuristic surface reconstruction. Iterative deconvolution has, however, the higher potential for topometric applications, as the algorithms include the option to merge several synchronously captured perspectives of the same object. The use of several perspectives allows one to measure the shape of arbitrary surfaces in contrast to the relief surfaces obtainable from a single perspective. Future research on hologram tomography should focus on an implementation of a multi-view SART-like algorithm for topometry: The use of perspective information in conjunction with the iterative approximation of the object is in my opinion the most promising approach to high-resolutional surface shape determination from holographic recordings in spite of the fact that today, it is of limited use due to technical restrictions.

Multiple perspective gradient averaging (MUPEGA)

As a synthesis of multi-view algorithms and tomography algorithms, the gradient averaging algorithm operates slice-wise and uses the in-slice gradients of multiple perspectives for a triangulation of object features. Due to the creation of the sub-holograms on a closed, elliptical path, the lateral gradient averages out for projections onto an out-of-focus screen whereas for in-focus projections, the gradient magnitude sums up for all perspectives. The experimental verification gives an improved axial resolution compared to standard surface finding techniques. The algorithm shows promising results in conjunction with eye-safe portrait holograms. The reconstructions obtained with eye-safe homogeneous object illumination did not result in surface reconstructions of the same quality as the recordings with structured illumination, but it seems likely that further improvements in the reconstruction set-up, for example the reconstruction with an exact wavelength match ($\mu = 1$), can improve the relatively high NER of the MUPEGA reconstructions and thus improve the axial resolution. Even with the current set-up, small object features as single hair can be resolved in the three-dimensional MUPEGA models. The MUPEGA algorithm allows precise surface shape measurements from eye-safe hologram recordings. The exposures made from the test object also indicate that the MUPEGA reconstructions have a sub-mm resolution (0.89 mm). With the current equipment, MUPEGA constitutes thus the best solution for surface shape measurements in the medical context.

Figure 4.31: Surface model and photographs of a patient before (left) and after (right) orthognatic jaw surgery.

4.3 Applications

The medical application has been the main motivation for the development of pulsed holography for surface shape measurement. A first clinical case is presented in the following section. As a further application, the holographic recording of an archeological object is described in section 4.3.2. Although a fast recording is not a major aspect in this context, the high resolution of holographic recordings is also desirable in the context of archeology. Apart from their topometric application, holographic recordings are also a valuable educational tool. In a public exhibition at the ”Deutsche Museum”in Munich [GBH01], portrait holograms recorded with structured illumination proved to be an ideal tool to raise concern for scientific topics. In the context of cultural heritage, holograms could thus provide an excellent way not only for scientific, but also pedagogical purposes.

4.3.1 Medicine

In this section, an example for the medical application of pulsed hologram tomography is given. In cooperation with C.U. Fritzemeier (Klinik für Kiefer- und plastische Gesichtschirurgie at the University of Düsseldorf), a patient undergoing a complex jaw surgery was recorded before and after the surgery. In maxillo-facial operations, a precise topometry of the patient is needed for operation planning. In order to achieve optimum operation results, accurate determination of the skull and the soft tissue covering it are essential: While the skeleton determines the basic proportions of the face, the thickness of the soft tissue is important for the appearance of the face. A study of Garlie and Saunders [GS99] on 615 lateral radiographs of adolescents aged from 6 to 20 years indicates that the facial tissue thickness varies from individual to individual - a significant prediction of any facial surgery should thus be based on an actual measurement of both soft and hard tissue of the face.

Apart from the prediction of the outcome of an individual operation, three-dimensional shape measurements are also of importance for the scientific improvement of surgical procedures. With common 2D imaging techniques, the quantification of the results of plastic surgery is difficult and can be influenced by a number of factors (light, lens, distance, background, patient’s position) as indicated in a study by A. Salmi *et al.* [SAAF97]. A three-dimensional surface shape documentation is thus an important tool for objective comparison of different operational techniques.

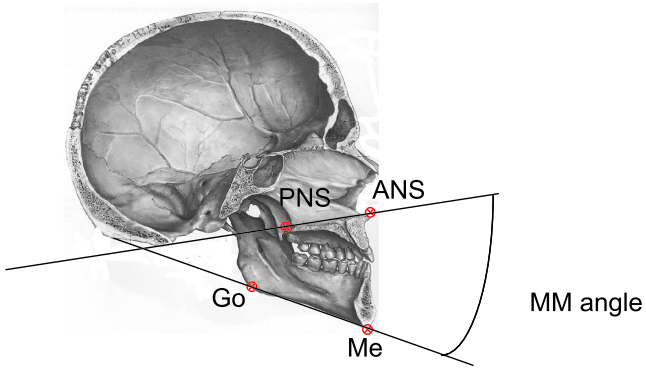

Figure 4.32: Definition of the maxillo-to-mandibular plane angle MM. Skull model from [TT98]

Indication

The patient undergoing surgery suffered from a long-face syndrome caused by a heritable disorder of the connective tissue known as Marfan syndrome. The Marfan syndrome affects the skeleton, lungs, eyes, heart and blood vessels. In many cases, patients with Marfan syndrome receive orthodontic treatment because of crowded teeth or extreme maxillary overjet even before diagnosis of or suspicion about the Marfan syndrome [WMB98].

The long-face syndrome characteristics are determined by the cephalometric maxillo to mandibular plane angle (MM angle): The palatal plane is defined by the anterior nasal spine (ANS) and the posterior nasal spine (PNS), the mandibular plane by the gonion (go), the most posterior inferior point on the angle of mandible and the menton (Me), the lower most point on the mandibular symphysis (Fig. 4.32). A MM angle which is larger than 32° indicates a significant deviation from the norm of 26° and the risk of developing severe characteristics of the long-face syndrome. These include excessive eruption of posterior teeth, large increases in vertical dimension, dental and skeletal open bite, and a retrusively positioned mandible [Pri97]. Frequent cephalometric radiography (every six to ten months) is advised to monitor the MM angle of patients with an increased risk of developing a long-face syndrome.

In the treatment of the long face syndrome, Fritzemeier performed an orthognatic surgery to correct the protrusion of the lower jaw. Immediately before and two months after the surgery, a frontal portrait hologram of the patient was captured.

Documentation and operation planning

The holograms were recorded with structured illumination and stripe projection[7]. The recording was not eye-safe and small laser goggles had to be worn by the patient during recording. Fig. 4.31 shows the three-dimensional computer models of the patient before and after the surgery in comparison with profile photographs. The second model shows the protective goggles and the adhesive tape which was used for eye protection. In the first model, these regions were excluded from the computer model. For operation planning, C. Tille and H. Seitz from the research center `caesar` provided a physical rapid-prototyping model for the surgeon (Fig. 4.34) based on the post-operational hologram. To combine the surface shape with the CT skull data set, the relative spatial orientation of two data sets has to be known. Finding the correct transformation from one data set to the other is the problem known as registration. In order to match the surface shape from hologram tomography with the CT data, an automated registration by least-square optimization was attempted by Z. Krol (research center `caesar`). However,no satisfactory

[7] At the time of recording, speckle projection was not yet available

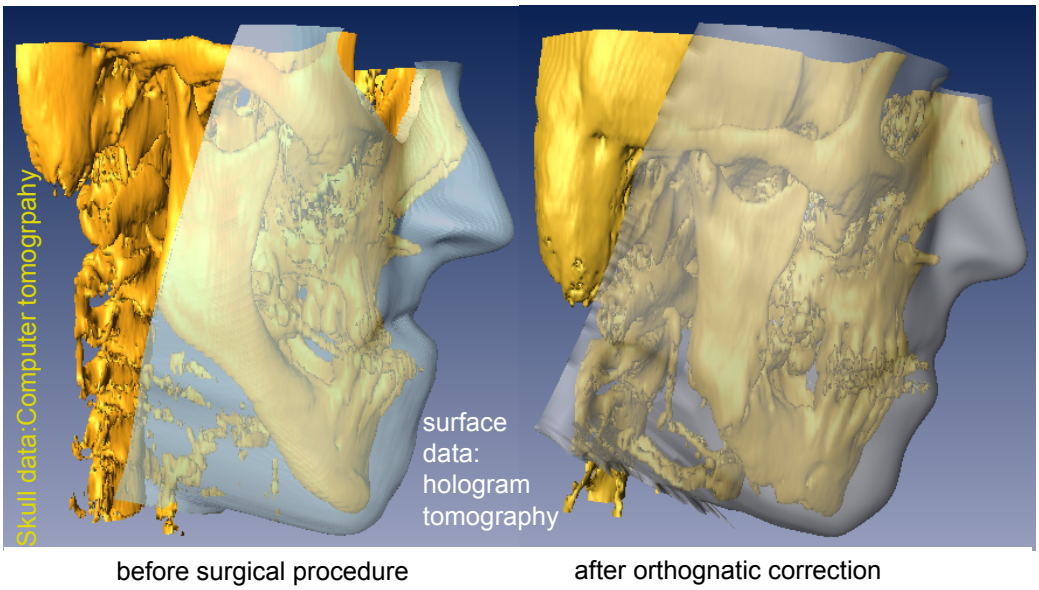

Figure 4.33: Superposition of a CT data set (yellow) and surface data obtained with hologram tomography (white) before (left) and after (right) the orthognatic surgery (Fig. 4.31). Registration was made manually (see text). Visualization in cooperation with Prof. U. Hartmann (FH Remagen)

results were obtained with the algorithms [Kro96] originally developed for the registration of two CT data sets. The main problems encountered were due to

- the poor localization of the skin surface in CT data sets,
- the different patient pose in CT and hologram recording (sitting/laying down),
- in particular, changes in the soft tissue under gravitation and
- a strong dependence of the registration algorithm on single outliers, i.e. points which are far away from the detected surface.

In order to overcome the problems of surface registration, a manual registration of the two data sets was attempted and is shown in Fig. 4.33. A rough contour of the skin was deduced by applying a so-called thresholding filter to the CT data set: All voxels with an absorptivity within a certain interval were connected to generate the skin surface. The upper bound of this interval has to be adjusted to distinguish the hard tissue (bones) from the soft tissue. Even more care has to be used for the lower bound which separates the skin from the surrounding air since the skin-to-air contrast is weak with x-ray imaging. The orientation of the hologram data set was subsequently adjusted to give a visually appealing match.

4.3.2 Archeology

In this section, an application of mirror hologram recording for archeology is presented. Images of archeological objects have always been of great interest to the scientific community and the public. In this context, holography has been used for recordings of cuneiform inscriptions or paintings [Dv97]. With hologram tomography, topometric surface data sets can be derived from archeological objects. In addition, volume hologram copies can be made and displayed with ordinary low-coherence incandescent lamps. Transport and display of holograms do not require special measures as opposed to the handling of fragile archeological findings.

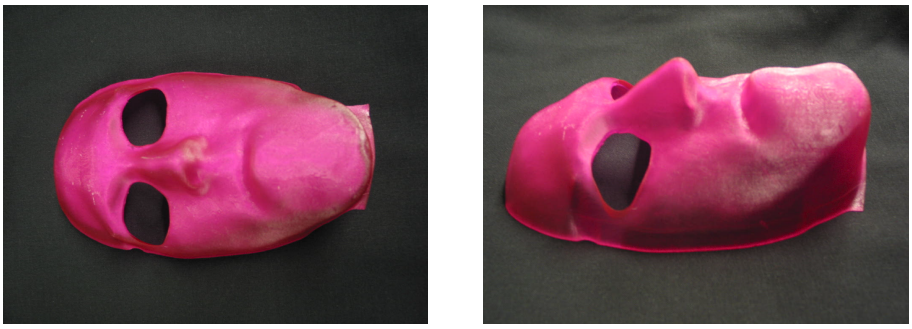

Figure 4.34: Pre-operative rapid prototyping model of a patient (Fig. 4.31) to visualize the relief data obtained with hologram tomography. Courtesy of C. Tille and H. Seitz.

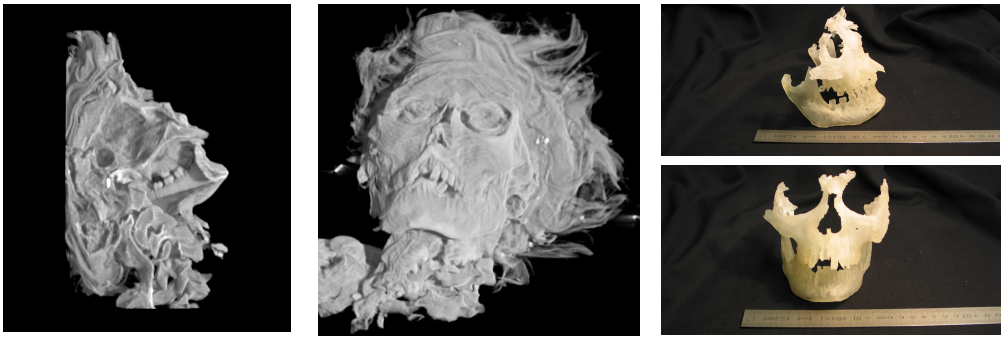

Figure 4.35: Three-dimensional CT model (left, middle) and photograph of a rapid prototyping model of the Husbäke bog bodies' skull. Courtesy of C. Tille and H. Seitz

To demonstrate the abilities of hologram topometry, a series of portrait holograms were made from the *Husbäke* bog body. It was found in 1936 near the city of Oldenburg, (Lower Saxony, Germany). The circumstances of the death of the male mummy are unknown. Assumptions include that the young man had an accident in the swamp or was victim of a crime, as the skull apparently had been damaged. In addition to the hologram tomographies, a research collaboration with the Landesmuseum Natur und Mensch in Oldenburg and the groups Holography and Rapid Prototyping of the research center `caesar` obtained CT models of the bog body (Fig 4.35). The soft tissues of the body were extraordinarily well preserved in the swamp, as sphagnum moss in the bog hindered decomposition. The death of the body was dated by carbon isotope analysis [(Ed02] between 20 BC to 200 AD. A photograph of the bog body in front of the holographic camera can be seen in Fig. 4.36. As the body was fixed to its support which could only be placed vertically, a large mirror at 45° to the hologram plane was used to provide an orthogonal perspective on the object. Two photographs of the virtual image of the direct and the mirrored object can be seen in Fig. 4.37. The photographs have different focal planes. The mirror object appears in the background above the direct object which gives a profile view of the bog body. Holograms of the complete body without stripe projection were obtained for white-light reflection hologram copies. These copies can be exhibited instead of the fragile bog-body and show the object surface features with high resolution.

Multiple hologram tomographies were made from the bog body with a stripe-projection arrangement. However, the surface models obtained with pulsed hologram tomography are inferior in resolution compared to the 3D models from computer tomography. As no restriction on the CT dosage rate had to be observed and no patient movements caused artifacts, the x-ray method provided high-resolution shape measurements.

Figure 4.36: The bog body, holographic camera (left) together with and 45° mirror (right)

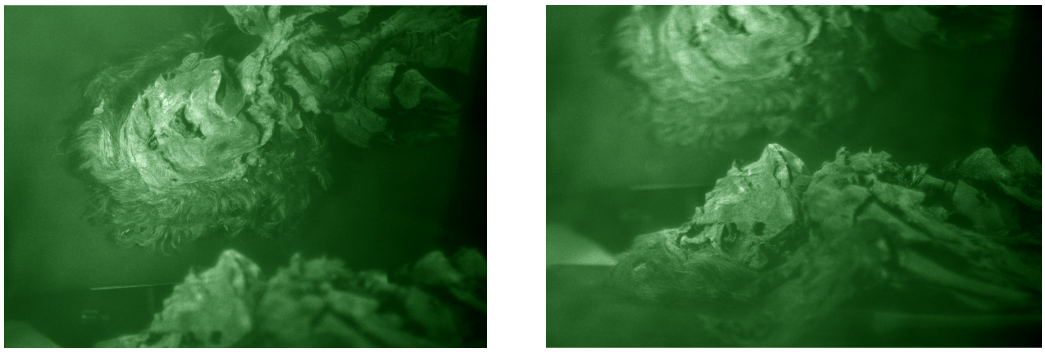

Figure 4.37: Photographs of virtual image of the bog body focused to the mirror object (left) resp. the direct object (right)

4.3.3 Discussion

Medicine

In order to help the physician to plan surgical procedures and to simulate the results, both the bone structure and the soft tissue thickness of the patients face have to be known. For the bone structure, three-dimensional models are obtained with x-ray computer tomography. In conjunction with the surface model from hologram tomography, the soft tissue thickness can be deduced from the two models. This requires appropriate registration of the two data sets which is a non-trivial and even an ill-posed problem if the soft tissue shape changes in between the two recordings. As the soft tissue shifts under gravity, the posture of the patient during the CT differs dramatically from that one during holography. The CT usually requires the patient lying down whereas holograms (and 2D photographs in plastic surgery) are recorded in an upright position to resemble the normal appearance of the patient. A better match between soft- and hard tissue date sets requires a more elaborate registration. With the currently available algorithms for hologram tomography, a first clinical application of facial topometry by hologram tomography was achieved. A preliminary evaluation of the technique of hologram tomography by the physician who accomplished the surgery [Fri03] indicates that the computer models from hologram tomography are a valuable tool for operation planning. At the time of writing, another study on hologram tomographies from patients with tumor resection cavities is being conducted and will be presented in future works. Based on the the experiences of the present work, a second holographic camera (Sec. 5.2) is beeing build. Additional clinical trials will be conducted in the in the maxillo-facial department of the Basel canton hospital (Abteilung für Kiefer- und Gesichtschirurgie, Kantonsspital Basel).

Archeology

Pulsed holography for archeological applications has major advantages over conventional photography. Holograms include full parallax - they give quantitative information (length, volume, surface, roughness) of the surface of the object. The mirror recording technique was successfully used to synchronously record an extended field-of-view of more than 90° in a single hologram. The advantages of holographic recordings - short exposure time, no focal plane adjustment, robustness to high object contrast, large capture range - suit the needs of many archeological applications. For example, a complete excavation site could be recorded with a pulsed holographic set-up if the pulse energy and the temporal coherence length of the laser could be made large enough. This could allow posterior identification of the position of archeological findings which is a major aspect for excavations with a tight time schedule. Current 3D documentation of archeological sites is based on photogrammetric measurement techniques, for example in the 3D MURALE project [J.01] which establishes 3D measurement techniques to "*reconstruct building elements and whole buildings from building blocks, pottery from pottery sherds, statues from statue elements and stratigraphy*[8] *from all finds within the excavation*"[J.01]. A prerequisite for the use of holography at an excavation site is a mobile holographic set-up which can be used even without dark-room conditions.

In between the field of medical and the field of archeological research, the forensic science is interested in the reconstruction of the faces of deceased persons. In many cases, only the skull of a deceased person is available, making the identification difficult. A reconstruction of the face from an experienced artist who sculpts a physical model of the head is an unreliable, yet often used method for identification. A more elaborate, computer based reconstruction technique for skull-based facial reconstruction could be used if one knew the approximate thickness of the soft tissue for persons of a certain age and gender. With the pulsed holography set-up presented

[8] Stratigraphy investigates the sequence of sedimentary structures, fossils and archeological findings for identifying and dating purposes of excavations

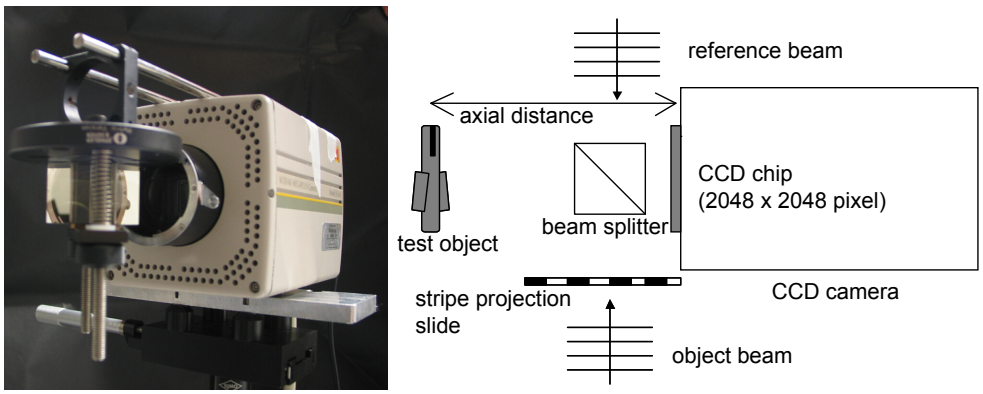

Figure 4.38: Beam-splitter and CCD camera (left) and sketch of the in-line set-up (right)

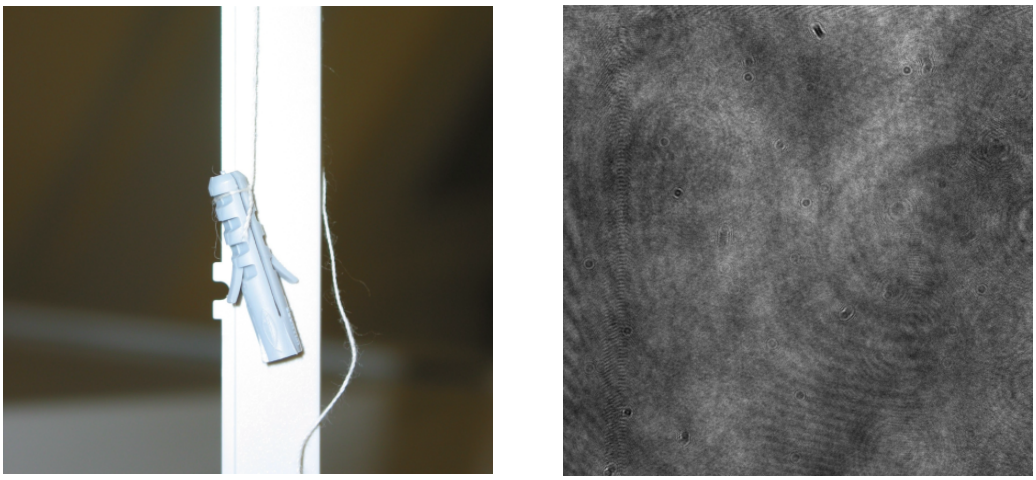

Figure 4.39: Photography (left) and digital hologram (right) of the test object

.

in this thesis, measurements of the skin surface could determine the soft tissue thickness in conjunction with a CT data set of the skull. From a large number of such soft tissue thickness measurements, one could derive typical values for a certain age and gender for post-mortem computer-generated facial reconstructions.

4.4 Digital recording

In the last section of this chapter, a surface topometry from a digitally recorded hologram is presented. Since the recording material, a CCD chip with 2048×2048 pixels, allowed only on-axis recordings of small objects, a hologram of a dowel (Fig. 4.38, left) was made with an object distance of appr. 150 mm. To enhance the axial surface determination, the object was illuminated with stripe projection. The hologram was reconstructed using O. Skotheims software `Holovision` [Sko01]. It allows numerical reconstruction of the object wave field from the intensities on the hologram plane under the assumption of a plane or spherical reference wave. The intensity of the interference pattern in the hologram plane serves as the input of the program. The object wave field intensity can be calculated at arbitrary points if the wavelength (526.5 nm) and the pixel spacing (6.7 μm) are known. Reconstructions of the object wave field at different distances (in the present case, axial distances from 146 mm to 154 mm) yield the

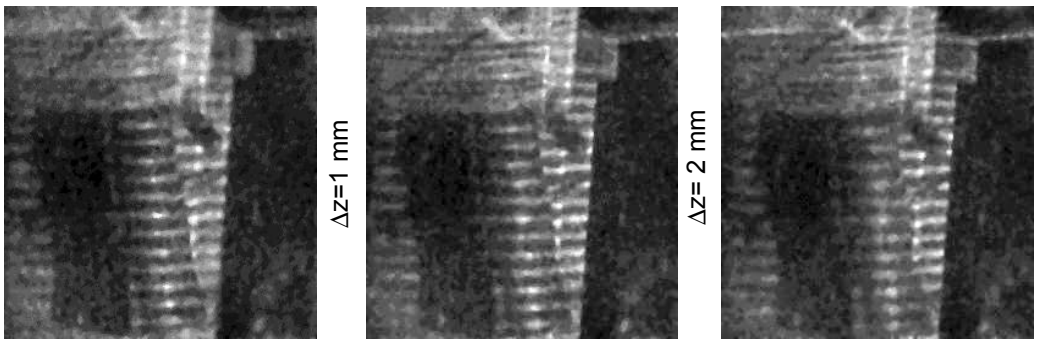

Figure 4.40: Numerical reconstructions at different axial distances (148, 149, 152 mm) of a digitally recorded pulsed hologram (Virtual hologram tomography)

.

same slice-by-slice representation as in hologram tomography with optical reconstruction: The method is thus called virtual hologram tomography. The software `Holovision` calculates the reconstructed wave field by numerical evaluation of the Rayleigh-Sommerfeld integral in the Fresnel approximation. The object wave field and the reference beam were superimposed by a beam splitter (Fig.4.38). The recorded holograms bear no similarity with the object (Fig. 4.39). The larger interference structures are due to small dust particles in the light path - they can be interpreted as in-line holograms from semi-transparent point objects. Numerical reconstructions at three different axial distances are shown in Fig. 4.40. From the virtual hologram tomography, only a noisy relief map of the object surface can be derived. By eye, the different position in the focal plane can be observed : The stripe pattern on the dowels surface in Fig. 4.40 appears sharper in the anterior numerical reconstruction (left) than in the posterior reconstruction (right). This indicates that the axial resolution is in the order of the diameter of the dowel (8 mm).

4.4.1 Discussion

With the current, low resolution of digital devices, holography is still restricted to applications where the object under consideration is small. In some medical applications, digital holography might be useful, for example in dentistry where objects of the size of single teeth are of interest [MR90] or with compact systems for endoscopic cavity examination [BDW+00].

The current digital recording technique already shows the potential of CCD recording: Without any wet-chemical or other processing, holography can be used for real-time topometry. In contrast to scanning techniques, the one-shot recording has an exposure time which is several orders of magnitude shorter than the actual CCD readout time. The temporal resolution is thus defined by the laser pulse length. Digital read-out takes only a fraction of the time for wet-chemical processing and with the prospect of CCD with a higher pixel number, the future application of digital holography in medical topometry seems very likely. The restrictions on the small field-of-view due to the large pixel sizes of several microns could be circumvented by suitable optical elements if the number of pixels is sufficiently high. Today, the maximum number of CCD pixels in a camera is 340.000.000 [Vei03] (distributed on several chips) for astronomical observations.

The technique of virtual hologram tomography can be used for semi-heuristic surface finding in digital holographic recordings. Using several perspectives from digital recording could also improve topometry: In this context, the synchronous recording with several CCDs at different locations and angles is preferable over mirror recording, as the limited angle of view of a CCD-recorded hologram hinders the recording of direct and mirror object. From a technical

point of view, this is not a disadvantage, since a given number of pixels can be more economically read out if they are distributed on a several CCDs. A scheme for recording extended objects thus could comprise a pulsed laser and several synchronously recorded digital holograms from different CCD chips. For a compact system, the reference beam could be applied with an optical fiber as has been demonstrated by Schedin *et al.* [SGTS99] who designed an all-fiber hologram recording system with a pulsed laser.

Chapter 5

Conclusion

This chapter summarizes the results obtained with different methods for hologram tomography and compares pulsed hologrammetry with existing optical topometry systems. Future developments of pulsed holographic systems are discussed in an outlook. The chapter is concluded by a section on the similarities of hologram tomography with cosmology, where the holographic principle (i.e. that a wave field is determined by its phase and the amplitude on a bounding surface) in conjunction with the analysis of the entropy of black holes leads to a two-dimensional model of the world.

5.1 Methods for surface reconstruction from holograms

In this thesis, five methods for surface shape measurement of hologram tomography have been examined: Weighted neighbourhoods is an extension of the previously described [Bon02] method of semi-heuristic surface finding by sharpness detection. It was successfully used to overcome the artifacts arising from sharpness calculation on square neighbourhoods where each pixel of a square area contributes to the same amount to figure-of-merit. By attributing a weight factor to each pixel to account for its distance to the centre of the area, a significant reduction of these square artifacts was achieved. These weights can be implemented for a large class of sharpness measures and do not speed up computation significantly. Reconstructions obtained with weighted figure-of-merit are quantitatively superior to those without.

The two deblurring methods applied to hologram tomography, inverse filtering and iterative deconvolution, both have been studied extensively in microscopy and computer sciences. Despite their origin from incoherent imaging, they can also be applied to holography. Both methods require the prior knowledge of the incoherent point-spread-function of the imaging system and assume that the PSF is approximately constant throughout the image volume. The a priori calculation of the holographic PSF leads to an optical transfer function without zero crossing, making a deblurring by inverse filtering theoretically feasible. Since the magnitude of the OTF function approaches zero quickly within the missing frequency cone, the use of an inverse filter is inhibited in the presence of noise: A division by the small values of the OTF function strongly augments the noise fraction of the measured image intensity. A regularised inverse filter was therefore used to deblur the holographic real image volumes. This technique shows a significant reduction of background intensity from out-of-focus object points. As a draw-back, the choice of the regularisation parameter strongly influences the outcome of the filtering. A reasonable method for optimum choice of the regularisation parameter was not found. In future works, a more elaborate technique for optimum choice of this parameter based on a noise estimation might be derived. While regularised inverse filtering offers a simple one-step calculation, iterative deconvolution relies on subsequent simulations of the imaging process. This apparent draw-back can be used for alternating iterative deconvolution: Synchronously captured

perspectives of an object and its mirror image were used for multi-view reconstruction with an extended view angle on the object. The iterative deconvolution of a test object by alternating use of holographic real images with different perspectives was demonstrated. However, the numerical combination of multiple real images of the same object by iterative deconvolution was limited in the present work by the the available computer memory capacity. As is well-known in computer tomography, an optimum three-dimensional reconstruction requires projections of the object to be recorded from all angles. A mirror recording could thus lead to an improved spatial resolution in addition to a larger view angle onto the object. By mirror recording, an almost arbitrary number of different perspective views can be recorded synchronously. In conjunction with iterative deconvolution from alternating perspectives, this method has the highest potential for ultra-fast high precision pulsed hologrammetry although with currently available personal computers, the method is restricted to a small number of different object views.

As memory limitations restrict the benefit from numerical methods for image deblurring, the multi-perspective gradient averaging method (MUPEGA) was developed. It combines multiple perspectives projected on a screen by lateral gradient calculation, a method also used in pattern recognition schemes. In addition to its main benefit, the high sensitivity even with the low contrast of - for example - holograms recorded with eye-safe, unstructured illumination, it has the advantage of economical memory use and efficient calculation. Future development might further improve the perspective generation from planar holograms by aperture masking, but one could also imagine that the perspective holograms from mirror recordings are used in a MUPEGA scheme. The optimization of the MUPEGA thus seems to be promising for short-term improvements of the axial resolution of holographic topometry while in the long-term, increased memory and storage capacity are likely to augment the importance of the numerical deblurring methods for hologrammetry and general 3D imaging in conjunction with the multi-perspective recordings obtained with planar mirrors, a technique which might be labelled holographic SART. The concept of hologram perspective is the key to both the MUPEGA and the holographic SART- to my knowledge, the present work makes use of this concept for the first time in the context of topometry.

5.2 Comparison with existing system

At the time of writing, hologram tomography undergoes additional testing with volunteers. Maxillo-facial surgeons in the universities of Basel, Düsseldorf and Cologne participate in an evaluation of the pulsed holographic camera system. A comparison with the manufacturers' specification of commercially available optical topometry systems (Fig. 5.1) shows that the spatial resolution obtainable with the current hologram tomography systems is still below the nominal resolution of common conventional systems, while the acquisition speed is extraordinarily high. Apart from the ultra-fast recording, another advantage of the two-step process is the simple recording procedure. Portrait holograms record structures down to the size of a single hair without any prior adjustment of the camera. Most laser scanning topometry system cannot detect such small features: Since hair is a common feature of human faces, the omission of it leads to unnatural three-dimensional computer models. The capture range of pulsed holography is larger than with commercial scanners, surpassed only by systems using time-of-flight measurements.

The experiments conducted for this thesis led to a novel design of a holographic camera which is being built at the time of writing. Commissioned by the research center `caesar` and the hospital of Basel (Abteilung für Kiefer- und Gesichtschirurgie, section maxillofacial surgery), it comprises capabilities for mobile pulsed recording, real image reconstruction with the recording wavelength ($\mu = 1$) and daylight recording. It will be used for further clinical evaluation of pulsed portrait holography without the need to transfer patients to the holographic

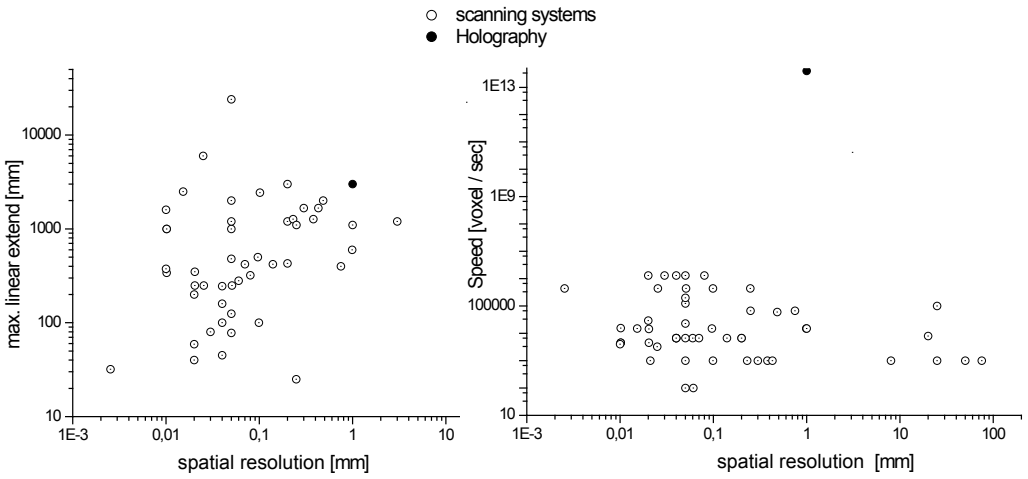

Figure 5.1: Spatial resolution versus range and speed of commercially available topometry systems. Source: [Har02a] based on manufacturer's specifications

laboratory.

5.3 Outlook

More than a decade had passed after the first paper on holography [Gab48] before the advent of the laser triggered the holographic revolution of the 1960ies. Holographic television was expected to be realized in the near future - a vision which dimmed together with the scientific interest in holography in the 1980ies. Most research in holography is today dedicated to the development of optical elements for telecommunication or data storage. The latter has has not yet surpassed rivaling techniques, for example the digital versatile disc (DVD) or magnetic storage media whereas holographic optical elements (HOE) as, for example, narrow-band holographic filters, are used in research and engineering regularly.

In the field of topometry, holography benefits from the recent advances in the technique of solid-state lasers: Frequency-doubled pulsed lasers offer a simple holographic recording technique and require less movable parts than laser scanning systems. Pulsed hologram tomography measures arbitrary surfaces without any scanning and is free of motion artifacts. When produced in large numbers, fast hologrammetry devices might therefore be even cheaper than laser scanners. These systems could give a high spatial resolution even when equipped with CCD or other electronic media if the main limiting factor of current digital recordings - the small viewing angle on the object - is overcome by composite recording of multiple holograms at different locations.

For medical applications, the qualitative information about the body surface in general and the face in particular could improve the diagnosis of hidden diseases, as for example the Marfan syndrome.

Numerical data processing techniques are rapidly approaching the capacity necessary to handle the large data sets which are recorded in medical facial topometry. The obvious implication is that the algorithms described in this thesis should be able to handle full-scale patient data sets at high resolution in the near future. Problems associated with the incomplete convergence of iterative deconvolution algorithms in this thesis may be overcome by adapting SART-type algorithms without the simplification of spatially-invariant PSF.

With increased electronic storage capability, one might also imagine the use of silver-halide hologram recording material for numerical reconstruction. By appropriate magnification of the

hologram, a numerical reconstruction the object wave field could be realized. With currently available techniques, however, a 300×300 mm^2 hologram with 3000 line pairs per mm is too large for direct digitalisation.

The theory of holography has only recently led to increased research in a different branch of physics: Following an essay of G. t'Hooft [T'H93], L. Susskind concluded that *"phenomena taking place in three-dimensional space can be projected onto a distant 'viewing screen' with no loss of information"* [Sus95]. For example, an event represented by a wave-function defined on the common four-dimensional (time/space) coordinate space can be described by its values on a three-dimensional surface which encloses the event. One could imagine to reconstruct a scattering event of two identical particles by measurement of the complete two-particle wave function on a temporal and spatial surface surrounding it. Such surface corresponds to a certain hologram perspective onto the event in the terms developed in this thesis. As in hologram tomography, the description of the event has a limited resolution if this surface has a finite size.

Susskind further argues that if one describes the world by a discrete lattice theory, one has to conclude that *"instead of a three dimensional lattice, a full description of nature requires only a two dimensional lattice at the spatial boundaries of the world."*[Sus95] The apparent three-dimensionality of the world is thus similar to the apparent three-dimensionality of the real holographic image: The hologram is a two-dimensional and has only a two-dimensional number of degrees of freedom (the index of refraction on the hologram plane). The argument assumes that the world is described by a finite lattice of "spin-like degrees of freedom"with a lattice spacing of the Planck length. With a three-dimensional spin lattice, the maximum possible entropy is proportional to the volume in space. According to the Bekenstein-Hawking formula, the entropy of a black hole is proportional to its surface area. Was the dimensionality of the finite lattice larger than two, a volume in space with a higher entropy than a black hole could be transformed into a black hole with lower entropy by the addition of mass, violating the second law of thermodynamics. The dimensionality of the finite lattice has thus to be two or lower[1]. Many publications on this cosmological application of the holographic principle were proposed, among others the replacement of the holographic principle by a generalized second law of thermodynamics or a change in the definition of "degrees of freedom"[WA00].

Within the scope of this thesis, no review of these ideas can be given, however, the recent interest in holography in this topic indicates the high potential of D. Gabor's ideas which still contribute to scientific progress.

[1] Susskind also presents a different line of reasoning from string theory

Appendix A

Textures

In computer sciences, a texture is a two-dimensional image which is mapped onto the surface of a three-dimensional model to achieve a photo-realistic impression. The following gives a short introduction to the basic concepts of textures and presents an algorithm for a camera-based texture algorithm for three-dimensional patient models. It presents a method to apply a photography as a texture onto 3D models from hologram tomography. An implementation of an algorithm to translate topometric relief data from hologram tomography into a three-dimensional texturized model is presented.

A.1 Basic terms

A texture is most commonly used to combine a high-resolution image to a low-resolution geometrical object in order to evoke a higher level of detail. By mapping a digital photography onto a geometrical model of a human face, one can create photo-realistic impressions of patients. These models allow the reliable identification of individuals as opposed to the geometrical models which are sometimes hard to recognize. Additionally, the combination of low-resolutional geometrical model and high-resolution texture allows one to reduce the number of spatial points in the model considerably without an apparent reduction in the quality of the visualization. Textures represent thus an effective method for 3D model compression for visual applications.

In this chapter, textures are represented by two-dimensional functions $t(u_1, u_2)$ which map the Euclidean texture plane into a colour space. In this context, no concise definition of the colour space is given. For a technical realization, one can think of it as a subspace of $\mathbb{R}^3$ where a colour is represented by a triple of positive numbers. Any such red-green-blue (RGB) value denotes the stimulation of the red (green, blue) colour sensitive receptors in the human eye according to the tristimulus theory. Any camera maps a 3D object onto its image, a (rectangular) region A of the Euclidean texture plane.

A photorealistic texture is usually recorded with a photographic camera: A three-dimensional object is imaged onto the two-dimensional photographic plane, mathematically a non-bijective projection. To illustrate this formalism, consider a pinhole camera (Fig. A.1). An object point $\vec{x} = (x_1, x_2, x_3)$ is imaged according to the theorem on intersecting lines if and only if the image point

$$\vec{u} \;=\; \begin{pmatrix} -x_1 \frac{B}{x_3} \\ -x_2 \frac{B}{x_3} \end{pmatrix} \tag{A.1}$$

lies within the image area. These expressions take the form of a linear equation if they are expressed in the so-called homogeneous coordinates wich describe the projective space.

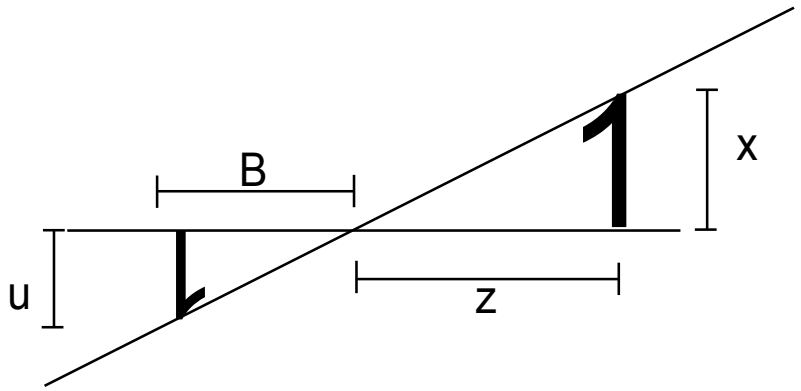

Figure A.1: Imaging an object with a pinhole camera of image distance B

A.1.1 Projective geometry and homogeneous coordinates

An element of the three-dimensional projective space $\mathbb{P}^3$ is a quadruple of four real numbers $\vec{x} = x_1, x_2, x_3, x_4$. In Euclidean space $\mathbb{R}^3$, the point $\vec{x}' = (x_1/x_4, x_2/x_4, x_3/x_4)$ is the canonical equivalent to this point. Obviously, each band in projective space $\vec{x} = (p_1/\kappa, p_2/\kappa, p_3/\kappa, \kappa)$ with $\kappa \neq 0$ corresponds to exactly one point in Euclidean space $\vec{x}' = (p_1, p_2, p_3)$. The quadruples with $x_4 = 0$ do not have an equivalent in Euclidean space. For example, the quadruple $(1, 8, 3, 1)$ and $(3, 24, 9, 3)$ both represent the (Euclidean) space point $(1, 8, 3)$. Accordingly, the two-dimensional projective space consists of triples $\vec{u} = (u_1, u_2, u_3)$ equivalent to points of the Euclidean plane $\vec{u}' = (u_1/u_3, u_2/u_3)$ plus points with no correspondence $\vec{u} = (u_1, u_2, 0)$.

In these homogeneous coordinates, the projection from three-dimensional object space into two-dimensional texture space (Eqn. A.1) takes a linear form:

$$\vec{u} \;=\; \mathbf{A}\vec{x} \tag{A.2}$$

with the camera matrix of the pinhole camera $\mathbf{A}$:

$$\mathbf{A} \;=\; \begin{pmatrix} B & 0 & 0 & 0 \\ 0 & B & 0 & 0 \\ 0 & 0 & 1 & 0 \end{pmatrix} \tag{A.3}$$

The additional coordinate in projective space replaces the non-linear division in equation (A.1). The points with no correspondence in Euclidean space $\vec{x} = (x_1, x_2, x_3, 0)$ can be interpreted as points at an infinite distance and do not need to be considered separately in this formalism.

A translation or rotation of the pinhole camera can be modeled by (right-) multiplication of the camera matrix with a 4×4-translational matrix $\mathbf{T}$ resp. a similar rotation matrix $\mathbf{R}$:

Translation by $\vec{t} = (t_x, t_y, t_z)$:

$$\mathbf{T} = \begin{pmatrix} 1 & 0 & 0 & t_x \\ 0 & 1 & 0 & t_y \\ 0 & 0 & 1 & t_z \\ 0 & 0 & 0 & 1 \end{pmatrix}$$

Rotation of α around the z-axis:

$$\mathbf{R}^z = \begin{pmatrix} \cos(\alpha) & -\sin(\alpha) & 0 & 0 \\ \sin(\alpha) & \cos(\alpha) & 0 & 0 \\ 0 & 0 & 1 & 0 \\ 0 & 0 & 0 & 1 \end{pmatrix}$$

A change in image distance B (lens camera equivalent to a zoom, i.e. a change in focal length) by a factor β can also be modeled by matrix multiplication:

$$\mathbf{R}^z = \begin{pmatrix} \beta & 0 & 0 & 0 \\ 0 & \beta & 0 & 0 \\ 0 & 0 & \beta & 0 \\ 0 & 0 & 0 & 1 \end{pmatrix}$$

In general, any (Euclidean) affine transform $\mathbf{T} \in \mathbf{R}^{3\times 3}$ in object space can be applied to the camera matrix by multiplication with

$$\mathbf{A}' = \mathbf{A} \left(\begin{array}{ccc|c} & \mathbf{T} & & \begin{matrix} 0 \\ 0 \\ 0 \end{matrix} \\ \hline 0 & 0 & 0 & 1 \end{array} \right)$$

The twelve parameters in the camera matrix A can therefore describe most of the camera parameters like focal length, position, orientation and the like. Only few effects of physical cameras like chromatic aberration and depth of focus are not included in this model. A number of algorithms exist for the determination of the camera matrix elements from photographs of gauge objects [FLM92].

A.2 Texture algorithm

In this section, a camera-matrix based texture algorithm is presented. Its implementation takes a grey-valued image as input and constructs a three-dimensional computer model in the virtual reality modeling language (VRML) standard. An arbitrary number of digital photographs can be mapped onto the model. All twelve parameters of the camera matrix can be individually set. Additionally, one can define up to three different numbers for the visibility of each model point. This visibility is a real number and describes which camera texture image is mapped onto the model point. This feature can be used to account for points which were occluded by other parts of the object on a certain camera positions.

The algorithm in Fig.A.2 starts with a relief function representing the surface $z(x, y)$ of the object. The implementation requires this surface function in the form of a grey-value file (file format TIFF) with dimensions $X \times Y$ and 8 bits per pixel (bpp) corresponding to grey values $0 \ldots 255$ or alternatively with 16 bpp ($0 \ldots 65535$). Each pixel corresponds to a lateral coordinate (x, y), its grey-value is the z-coordinate. The implementation allows the definition of a region-of-interest on the rectangular image file in order to allow models with non-rectangular shapes. The representation as grey-values limits the axial coordinates to discrete values. For example, a model represented by depth values represented by 16 bpp and a physical depth of 300 mm has 4 μm deep steps instead of a smooth depth relief. These steps would be 256 times larger (1.17 mm) if only 8 bpp were used.

The physical coordinates of an object point are calculated for each point P of the surface of the model:

$$P = \begin{pmatrix} p_1 \\ p_2 \\ p_3 \end{pmatrix} = \begin{pmatrix} X \cdot \delta x \\ Y \cdot \delta y \\ Z(X,Y) \cdot \delta z \end{pmatrix} \equiv \begin{pmatrix} X \cdot \Delta x \\ Y \cdot \Delta y \\ Z(X,Y) \cdot \Delta z \\ 1 \end{pmatrix} \tag{A.4}$$

where $\delta x, \delta y, \delta z$ denote the physical size of one pixel or the equivalent of one grey value, respectively. Now each point of the surface model P is projected into texture space for each

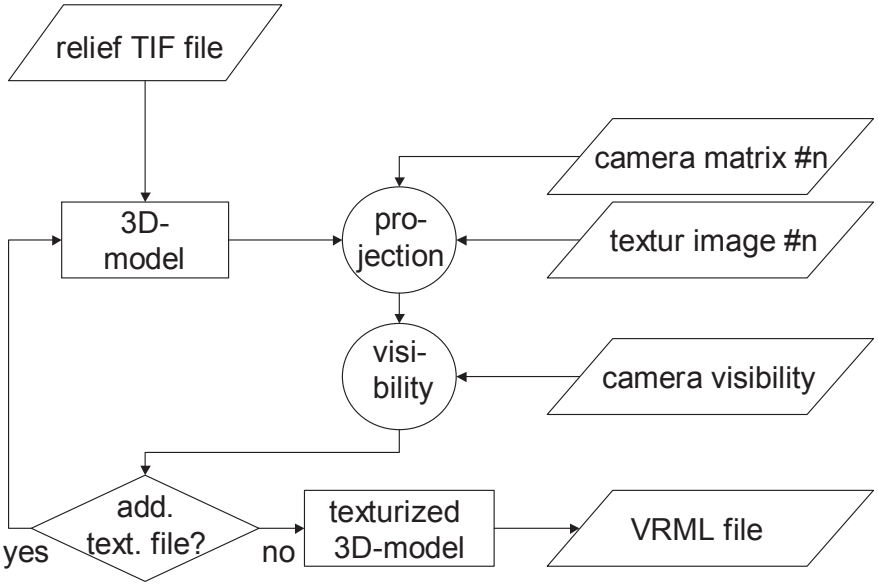

Figure A.2: Camera-matrix based texture algorithm

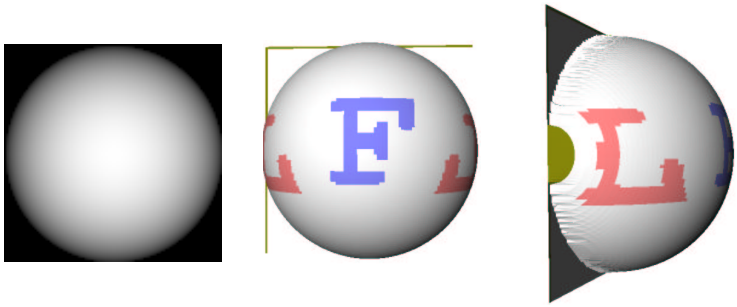

Figure A.3: Computer model of a semi-sphere as grey-value relief (left) and VRML model (middle, right) with two superimposed texture images (Fig. A.4

camera to give the two-dimensional texture coordinate $\vec{p}$:

$$\vec{p} = \begin{pmatrix} u' \\ v' \end{pmatrix} = \begin{pmatrix} u/w \\ v/w \end{pmatrix} \equiv \begin{pmatrix} u \\ v \\ w \end{pmatrix} = \mathbf{A}'\vec{P} \tag{A.5}$$

$\vec{p}$ denote the position of the surface point on the image plane of the camera. The program can merge an arbitrary number N of camera image files, each with an individual camera matrix $\mathbf{A}'$. The camera matrices are defined by twelve real numbers stored in a separate file which also contains the file names of the texture images. Any of the point projections within or outside the boundaries of a particular camera image. The latter means that this point was not included in the field-of-view of that particular camera, so the camera image contains no colour information of that surface point. If the texture coordinates of a surface point are within the boundaries defined by the camera image, it is visible to the camera and the surface point is coloured according to the camera image file. One point might be visible from several camera positions: In that case, the colours from different texture images might vary from and the surface point is assigned the average colour, i.e. the geometrical mean of the R, G and B values of all camera images.

Fig. A.3 gives an example of a textured image made out of a relief file of a semi-sphere. The texture images are depicted in fig. A.4, the camera matrices used represent two parallel projections with a relative orientation of 90°. The camera matrix algorithm does not model

Figure A.4: Texture images of A.4.

any obstruction. This can be seen in Fig. A.3, where the ”L”(left) texture image is projected onto both sides of the hemisphere. These obstruction effects cannot be modeled easily without a complete ray-tracing which requires extensive computations. A mechanism to account for obstructed cameras was implemented: The colour-averaging process was modified with appropriate visibility weighting factors, i.e. each camera contributes to the colour of the computer model proportional to an arbitrarily factor. For each model point, the relative weight of camera n can be defined. When a particular camera cannot see the point i_0 the visibility weight is thus zero. In addition to occlusions, this mechanism can also describe smooth transitions between regions which are imaged from multiple cameras.

The current implementation of the camera matrix texture algorithm allows an unlimited number of camera textures to be used. However, the number of different weights is limited to three as the camera visibilities are stored as a RGB-coded graphic file format: The weights are defined by an image file with the same dimensions as the grey-level relief file. Each pixel of this visibility file corresponds to an object model point. The red component of the visibility file defines the relative visibility of camera 1, the green component that of camera 2, the blue that of camera 3. This is merely a convention to allow economic storage and convenient handling of the camera visibilities weights. The RGB-values used to define the visibility are in no way connected to a physical colour and should not be confused with the RGB-values of the texture files.

Manual

The implementation of the camera matrix texturing algorithm is a plug-in for the free software package `imageJ` [Ras02]. The plug-in is called `Relief2VRML`. A graphical user interface is used to set the following parameter values:

- lateral physical dimensions of the relief file in mm
- longitudinal physical equivalent of one grey value (Δz)
- texture script file name

The relief file for 3D model generation is the active file of the `imageJ` program. The output VRML file has the same path and name as the relief file plus the extension `wrl`. The texture script file name is an ASCII file in the imageJ root directory - if no such file exists, no textures are applied. The script file contains the camera matrix elements and the file names of the texture image files. For example, the texture script file used for Fig.A.3 is:

```
# Tue Jul 16 14:14:11 GMT+02:00 2002
Cameras=2
CameraTexture0=d\:\\150702\\links.tif
```

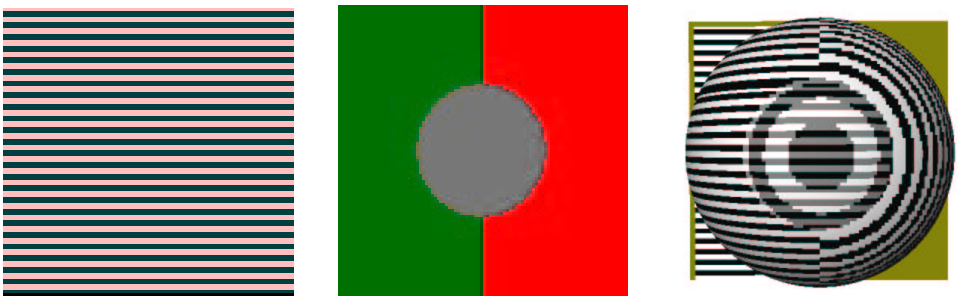

Figure A.5: Computer model (right) of a semi-sphere with two textures (left, second texture is 90° rotated) with camera weight file (middle: 50 % green, 50% red)

```
CameraMatrix0=0;0;64;-1;0;64;0;-1;0;0;0;1;
CameraTexture1=d\:\\150702\\front.tif
CameraMatrix1=64;0;0;-1;0;64;0;-1;0;0;0;1;
```

Lines starting with a # are ignored by the program and can be used for comments. The lines containing the two camera matrices start with `CameraMatrix0` and `CameraMatrix1`. They list the matrix elements of the camera matrices line-by-line. An image file describing the visibilities of the model points can be set by adding the line

```
CameraWeight=file.tif
```

An example for the use of a visibility weight file is given in Fig. A.5. Hologram tomography is only capable of recording a monochromatic wave field of an object. Although research on colour holography resulted in the first true-colour reflection holograms recorded with three different cw-laser (see, for example [BJV96]), pulsed colour holography has to my knowledge not been realized yet. The technical problems encountered include the need of three high-coherence, short-pulsed lasers which preferably emit radiation synchronously and with a sufficiently high pulse energy. Additionally, the recording material has to be sensitive at those three wavelengths. Since photorealistic models of human faces can be created with textures, this method is preferable over true-colour holography for topometry. Coloured surface models have the advantage of a better acceptance by the physician and the patient. In operation planning, the physician uses certain landmarks of the computer model to localize the planned operation sites. A high-resolution surface texture is thus helpful to improve the physician's orientation. The patients who volunteered for the hologram tomography case studies strongly favoured the texturized models over purely geometrical models. A better acceptance of computer simulations based on the models can thus be expected. This could give a psychologically important momentum to increase the patients' satisfaction with the operation outcome wich is an important aspect as indicated by a study of Varela and Garciacamba [VG95] on the influence of the patients' body image and self-concept in orthognatic surgery.

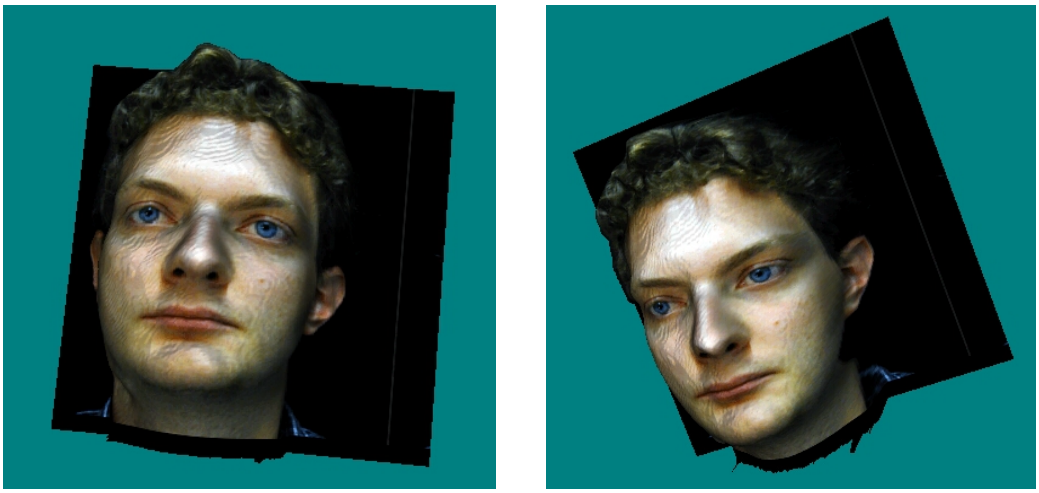

Figure A.6: Photo-realistic facial model obtained by combination of a holographically recorded relief and a photographic image

List of Figures

List of Tables

Bibliography

[Agf02] Agfa-Gevaert AG. Technisches Datenblatt F-PF-D2 (Agfa Professional Filmsortiment). Technical report, Agfa-Gevaert, www.agfa.com, 2002. http://www.agfa.com/photo/products/de/pdf/F-PF-D2_de.pdf.

[AK84] A. H. Andersen and A. C. Kak. Simultaneous algebraic reconstruction technique (SART): A superior implementation of the ART algorithm. *Ultrasonic Imaging*, 6:pp. 81 – 94, 1984.

[Ans70] D. A. Ansley. Techniques for pulsed laser holography of people. *Applied Optics*, 9:815, 1970.

[ASCE02] N. Aspert, D. Santa-Cruz, and T. Ebrahimi. MESH: Measureing errors between surfaces using the hausdorff distance. In *Proc. of the IEEE International Conference in Multimedia and Expo*, pages 705–708, 2002.

[BA00] C. Beumier and M. Archeroy. Automated 3d face authentication. *Image and vision computing*, 18:315–321, 2000.

[BDW+00] Kemper B, Dirksen D, Avenhaus W, Merker A, and G. v. Bally. Endoscopic double-pulse electronic-speckle-pattern interferometer for technical and medical intracavity inspection. *Appl. Opt.*, 39(22):3899–3905, 2000.

[BGH00] J. Bongartz, D. Giel, and P. Hering. Living human face measurements using pulsed holography. In *Proceedings of SPIE, Holography, Vol. 4149*, 2000.

[Bje92] H. I. Bjelkhagen. Holographic portraits made by pulse lasers. *Leonardo*, 25(5):443–448, 1992.

[Bje95] H.I. Bjelkhagen. *Silver-Halide Recording Materials*. Springer, 1995.

[BJV96] H.I. Bjelkhagen, T.H. Jeong, and D. Vukicevic. Color reflection holograms recorded in a panchromatic ultrahigh-resolution single-layer silver halide emulsion. *Journal of Imaging Science and Technology*, 40(2):134–146, 1996.

[BM92] P. Besel and N. McKay. A method for registration of 3d shapes. *IEEE Transaction on Pattern Analysis and Machine Intelligence*, 14(2):239–256, 1992.

[Bon02] J. Bongartz. *Hochauflösende Dreidimensionale Gesichtsprofilvermessung mit Kurzgepulster Holographie*. PhD thesis, Mathematisch-Naturwissenschaftliche Fakultät der Heinrich-Heine-Universität Düsseldorf, 2002.

[BS91] I.N. Bronstein and K.A. Semendjajew. *Taschenbuch der Mathematik*. B.G. Teubner Verlagsgesellschaft, 25th edition, 1991.

[BSK01] S. Baker, T. Sim, and T. Kanade. A characterization of inherent stereo ambiguities. In *Proceedings of the IEEE 8th International Conference on Computer Vision*, pages 428–437, Vancouver, Canada, 2001. IEEE.

[Bun86] Deutscher Bundestag. Passgesetz (PassG). BGBl I 1986, 537, April 1986. revised version from the 21.August 2002.

[BW01] M. Born and E. Wolf. *Principles of Optics*. Press syndicate of the university of Cambridge, 7th edition, 2001.

[CAP+02] P.K. Christou, A.E. Athanasiou, P. Boettcher P, H.F. Zeilhofer, R. Sader, and M.A. Papadopulos. Three-dimensional craniofacial reconstruction imaging. *Oral surgery oral medicin oral pathology oral radiology and endodontics*, 93(4):382–393, 2002.

[Cha66] E.B. Champagne. Nonparaxial imaging magnification and aberration properties in holography. *J. Opt. Soc. Am.*, 56(10):1448, 1966.

[Con95] J. A. Conchello. Superresolution and convergence properties of the expectation-maximization algorithm for maximum-likelihood deconvolution of incoherent images. *J. Opt. Soc. Am. A*, 15(10):2609–2619, 1995.

[De02] D. Dirksen and G. v. Bally *et al*. Optical 3d acquisition of facial surface structures for computer aided design and rapid prototyping of facial protheses. In *International Symposium on Photonics in Measurement*. VDI, Verein deutscher Ingenieure, 2002.

[DEG+] T.Q. Duong, E.Yacoub, G.Adriani, X. Hu, K. Ugurbil, J.T. Vaughan Andn H. Merkle, and S.G. Kim. High-resolution, spin-echo BOLD and CBF fMRI at 4 and 7 tesla.

[Dür] A. Dürer. *Vier Bücher Von Menschlicher Proportion*. E. Stocker, Dietikon-Zürich 1969, facsimile of the 1528 original edition.

[Dür00] A. Dürer. *Unterweisung der Messung mit Dem Zirkel und Richtscheit in Linien, Ebenen und Ganzen Corporen*. A. Uhl Verlag, Nördlingen, A. Uhl, 3rd edition, 2000. Facsimile reprint of the edition published in Nürnberg (1525).

[Dv97] F. Dreesen and G. v. Bally. *New Technologies in the Humanities*, volume OWLS IV of *Optics Within Life Sciences*, chapter Color Holography in a Single Layer for Documentation and Analysis of Cultural Heritage, pages 79–82. Springer Verlag, 1997.

[EA93] J. Eichler and G. Ackermann. *Holographie*. Springer, 1993. chapter 2 pp. 12.

[(Ed02] C. Holden (Ed.). A face for german bog man. *Science*, 297:1271, August 2002. ('Random sample' news section).

[EKL+01] B. Erdmann, C. Kober, J. Lang, P. Deuflhard, H.-F. Zeilhofer, and R. Sader:. Efficient and reliable finite element methods for simulation of the human mandible. In *Proceedings 9th Workshop on the Finite Element Method in Biomedical Engineering, Biomechanics and Related Fields, Ulm*, page 82, 2001.

[FH98] X. Fang and P.R. Hobson. Effect of spherical aberration on real-image fidelity from replayed in-line holograms of underwater objects. *Applied Optics*, 37(15):3206–3214, 1998.

[FLM92] O.D. Faugeras, Q.-T. Luong, and S.J. Maybank. Camera self-calibration: Theory and experiments. In G. Sandini, editor, *Lecture Notes in Computer Science Vol 588*, pages 321–334. Springer-Verlag, 1992.

[Fom98] N.A. Fomin. *Speckle Photography for Fluid Mechanics Measurement*. Experimental Fluid Mechanics. Springer, 1998.

[Fri03] C.U. Fritzemeier. Die optische gesichtsreliefvermessung mit hilfe der gepulsten holographie, möglichkeiten der diagnostik, der qualitätskontrolle und der daraus resultierenden therapieansätze. In *7. Kongress der Österreichischen Gesellschaft Für Mund-, Kiefer- und Gesichtschirurgie*, February 1st 2003.

[Gab48] D. Gabor. A new microscopic principle. *Nature*, 161:777–778, 1948.

[GB02] A. Del Guerra and N. Belcari. Advances in animal PET scanners. *Quaterly journal on nuclear medicine*, 46:35–47, 2002.

[GBH01] D. Giel, J. Bongartz, and P. Hering. Hologramm und Knochensäge - Lasereinsatz in der Gesichtschirurgie. In *Physik und Leben*. DPG, BMBF, Deutsches Museum, 2001. Science exhibition 'Jahr der Lebenswissenschaften'.

[GBH02] D. Giel, J. Bongartz, and P. Hering. Ultrafast holographic topometry for medical applications. In *VDI-Berichte 1694*, June 2002.

[GHNW00] D. Giel, G. Hinz, D. Nettels, and A. R. Weis. Diffusion of Cs Atoms in Ne Buffer Gas Measured by Optical Magnetic Resonance Tomography. *Opt. Express*, 6:251–256, 2000. http://www.opticsexpress.org/abstract.cfm?URI=OPEX-6-13-251.

[GL80] G. Gasusmann and W. Lauterborn. Determination of size and position of fast moving gas bubbles in liquids by digital 3-d image processing of hologram reconstructions. *Applied Optics*, pages 3529–3535, 1980.

[Goo75] J. W. Goodmann. *Statistical Properties of Laser Speckle Patterns*, chapter 2, pages 9–75. Springer, 1975.

[GS99] T.N. Garlie and S.R. Saunders. Midline facial tissue thicknesses of subadults from a longitudinal radiographic study. *Journal of forensic sciences*, 44(1):61–67, 1999.

[GW93] R.C. Gonzalez and R.E. Woods. *Digital Image Pocessing*. Addison-Wesley, 1993.

[Har97] G. G. Harigel. Measurement of bubbles in a superheated liquid. *Nuclear instruments and Methods in Physics Research A*, 421:12–22, 1997.

[Har02a] S. Harper. 3d scanner survey. Technical report, Raindrop Geomagic, Inc., www.geomagic.com, 2002.

[Har02b] J. E. Harvey. *Non-Paraxial Scalar Diffraction Theory*. SPIE Press, 2002.

[HK99] G. T. Herman and A. Kuba. *Discrete Tomography*. Birkhäuser, 1999.

[HL01] E. Hjelmas and B.K. Low. Face detection: A survey. *Computer vision and image understanding*, 83:236–274, 2001.

[Ing71] E. Ingelstam. Presentation speech for the nobel prize in physics. http://www.nobel.se/physics/laureates/1971/press.html, 1971.

[J.01] Cosmas J. 3d measurement and virtual reconstruction of ancient lost worlds of europe. http://www.cultivate-int.org/issue5/3d/, October 2001.

[JB94] T.R. Judge and P.J. Bryanstoncross. A review of phase unwrapping techniques in fringe analysis. *Optics in lasers in engineering*, 21(4):199–239, 1994.

[JC65] J.W. Tukey J.W. Cooley. An algorithm for the machine computation of the complex fourier series. *Mathematics of Computation*, 19:297–301, 1965.

[JM70] A. D. Jacobson and F. J. McClung. Holograms produced with pulsed laser illumination. *Applied Optics*, 9:103, 1970.

[JS94] W. Jüptner and U. Schnars. Direct recording of holograms by a CCD target and numerical reconstruction. *Applied Optics*, 33(2):179–181, 1994.

[KHJS02] K.S. Kim, J.S. Hwang, J.S. Jeong, and T.K. Song. An efficient motion estimation and compensation method for ultrasound synthetic aperture imaging. *Ultrasonic imaging*, 24(2):81–99, 2002.

[KK01] V. P. Kandidov and A.V. Kondrat'ev. Talbot effect in gaussian optical systems. *Quantum electronics*, 31(11):1032–1034, 2001.

[KO96] S. A. Kochengin and V.I. Oliker. Determination of reflector surfaces from near-field scattering data. *Numer. Math.*, 79:553–568, 1996.

[Kre00] T. Kreis. Digital holography for metrologic applications. In P. Jacquot and J.-M. Fournier, editors, *Interferometry in Speckle Light, Theroy and Applications, Proceedings of the International Conference*, pages 205–212. Springer-Verlag, July 2000.

[Kro96] Z. Krol. Surface-similarity vs. voxel-similarity based registration of multimodality medical images using simulated annealing. *Bildverarbeitung für die Medizin, Algorithmen-Systeme- Anwendungen.*, pages 167–172, 1996.

[KS88] A.C. Kak and M. Slaney. *Priniples of Computerized Tomographic Imaging*. IEEE press, 1988.

[KWH+96] E.P. Krantz, J. Watson, P.R. Hobson, R.S. Lampitt, and A. Rogerson. Off-axis transmission holographic system for recording aquatic particles. In T. Braet, editor, *Design and Engineering of Optical Systems*, pages 189–198. Proceedings of the SPIE, vol. 2774, 1996.

[Lat71] J. N. Latta. Computer-based analysis of holography using ray tracing. *Applied Optics*, 10(12):2698–2796, 1971.

[LC82] G. Ligthard and C.A.Groen. A comparison of different autofocus algorithms. In *Proc. Of IEEE Int. Conf. On Pattern Recognition*, pages 597–600, 1982.

[Lin02] N. Linnenbrügger. Plug-in for fast fourier transform. http://rsb.info.nih.gov/ij/plugins/fftj.html, 2002.

[Lip93] H. Lippert. *Lehrbuch der Anatomie*. Urban und Schwarzenberg Verlag, 1993. chapter 1, pp 83-90.

[LKB+00] B. F. Lane, M. J. Kuchner, A. F. Boden, M. Creech-Eakman, and S. R. Kulkarni. Direct detection of pulsations of the cepheid star ζ gem and an independent calibration of the period-luminosity relation. *Nature*, 407:485–487, 2000.

[LNS03] M. Larsson, H. Nilsson, and T. Strömberg. In vivo determination of local skin optical properties and photon path length by use of a spatially resolved diffuse reflectance with applications in laser doppler flowmetry. *Applied Optics*, 42(1):124–134, 2003.

[LU63] E. Leith and J. Upatnieks. Wavefront reconstruction with continuous-tone objects. *J. Opt. Soc. Am.*, 53:1377, 1963.

[Mah01] V. Mahajan. *Optical Imaging and Aberrations*. SPIE -The international society of photo engineers, 2001.

[May97] F. Mayinger. Tropfenspektrum, Tropfenbewegung und Wärmeübergang bei verdampfenden Einspritzstrahlen aus lamellenbildenden Düsen. DFG-Forschungsvorhaben Abschlussbericht, TU München, Dt. Forschungsgemeinschaft, 1992, 1997. Aktenzeichen MA / 501 31 - 1 + 2, 01.10.92-31.01.97.

[Mes99] D. Meschede. *Optik, Licht und Laser*. Teubner, 1999.

[MR90] B. Martensson and H. Ryden. Holodent system, a new technique for measurement and storage of dental casts. In Stephen N. Joffe, editor, *Proc. Of the SPIE Vol. 1200*, volume 1200, pages 387–391, 1990.

[NR02] F. Natterer and E.L. Ritman. Ast and future directions in x-ray computed tomography (CT). *International journal of imaging systems and technology*, 12(4):175–187, 2002.

[Nüc02] Andreas Nüchter. Autonome Exploration und Modellierung von 3D-Umgebungen. Master's thesis, Universität Bonn, Institut für Informatik III, 2002.

[Nyq28] H. Nyquist. Certain topics in telegraph transmission theory. *Trans. AIEE*, pages 617–644, 1928.

[oNIRP00] International Commission on Non-Ionizing Radiation Protection. Revision of guidelines on limits of exposure to laser radiation of wavelengths between 400 nm and 1.4m. *Health Physics*, 79:431–440, 2000.

[Ost89] J. I. Ostrowski. *Holographie - Grundlagen, Experimente und Anwendungen*. Harri Deutsch, 1989.

[Ost02] J. Osterholz. *Frequency-Domain-Spektroskopie und dynamische Streulicht-Spektroskopie an biologischen Geweben*. PhD thesis, Mathematisch-Naturwissenschaftliche Fakultät der Heinrich-Heine-Universität Düsseldorf, 2002.

[Pau99] H. Paul. *Lexikon der Optik*. Spektrum akademischer Verlag, 1999.

[PM00] Y. Pu and H. Meng. An advanced off-axis holographic particle imaging velocimetry (HPIV) system. *Experiments in fluids*, 29:184–197, 2000.

[Pre92] William H. Press. *Numerical Recipes in C : The Art of Scientific Computing*. Press Syndicate of the University of Cambridge, 1992.

[Pri97] J. Prittinen. Orthodontic management of long face syndrome. *General Dentistry*, 45(6):568–572, 1997.

[Ras02] Wayne Rasband. ImageJ. http://rsb.info.nih.gov/ij/, 2002. Public domain Java image processing program.

[Rog97] A. Roggan. *Dosimetrie Thermischer Laseranwendungen in der Medizin- Untersuchungen der Optischen Gewebeeigenschaften und Physikalisch-Mathematische Modellentwicklung*, volume 16. ecomed Verlag, 1997.

[RTG98] R. Shahidi R, R. Tombropoulos, and R.P. Grzeszczuk. Clinical applications of three-dimensional rendering of medical data sets. *Proceedings of the IEEE on*, 86(3):555–568, 1998.

[SAAF97] A. Salmi, J. Alstela, S. Askoseljavaara, and J.W. Futrell. True lies- photographic misinterpretation in plastic surgery. *European journal of plastic surgery*, 20(6):292–296, 1997.

[Saf98] J. E. Safra. *The New Encyclopaedia Britannica*, volume 16, chapter Coins and Coinage, pages 529–555. Encyclopaedia Britannica, 15th edition edition, 1998.

[SGTS99] S. Schedin, G. Pedrini G, H.J. Tiziani, and F.M. Santoyo. All-fibre pulsed digital holography. *Optics communications*, 165(4-6):183–188, 1999.

[SH01] C.N. Stephan and M. Henneberg. Building faces from dry skulls: Are they recognized above chance rates? *Journal of forensic science*, 46(3):432–447, 2001.

[Sie68] L.D. Siebert. Large scene front-lighted hologram of a human subject. *Proc. of the IEEE*, 58:1242–1243, 1968.

[Sie86] A. E. Siegmann. *Lasers*. University Press, Oxford, 1986.

[Sko01] Oystein Skotheim. HoloVision - a software package for reconstruction and analysis of digitally sampled holograms. Master's thesis, Norwegian Universtiy of Science and Technology, 2001.

[Sus95] L. Susskind. The world is a hologram. *Journal of mathematical physics*, 36(11):6377–6396, 1995.

[T'H93] G. T'Hooft. Dimensional reduction in quantum gravity. *Utrecht Preprint THU*, 1993. http://arxiv.org/abs/gr-qc/9310026.

[TT98] B. Tillmann and G. Töndury. *Rauber/Kopsch: Anatomie des Menschen, Lehrbuch und Atlas*. Georg Thieme Verlag, Stuttgart, 2nd edition, 1998. p. 687.

[Vei03] C. Veillet. The world's biggest digital imager ready to explore the universe on the canada-france-hawaii telescope. http://www.cfht.hawaii.edu/News/MegaPrime/, April 2003.

[VG95] M. Varela and J.E. Garciacamba. Impact of orthodontics on the psychologic profile of adult patients- a prospective study. *American Journal of orthodontics and dentofacial orthipedics*, 108(2):142–148, 1995.

[WA00] B. Wang and E. Abdalla. Holography and the generalized second law of thermodynamics in (2+1)-dimensional cosmology. *Phys. Lett. B*, 471(4):346–351, 2000.

[Wat93] J. Watson. High-precision measurement by hologrammetry. *British journal of non-destructive testing*, 33(11):628–633, 1993.

[WMB98] L. Westling, B. Mohlin, and A. Bresin. Craniofacial manifestations in the marfan syndrome: Palatal dimensions and a comparative cephalometric analysis. *Journal of craniofacial genetics and developmental biology*, 18(4):211–218, 1998.

[YdV00] Saad Y and H.A. Van der Vorst. Iterative solution of linear systems in the 20th century. *Journal of computational and applied mathematics*, 123(1-2):1–33, Sp. Iss. November 2000.

[ZRRV01] S. Zacharovas, A.M. Rodin, D.B. Ratcliffe, and F.R. Vergnes. Holographic materials available from geola. In *Proc. SPIE Vol. 4296 (Practical Holography XV and Holographic Materials VI)*, pages 206–212, 2001.

Acknowledgements

A number of people have contributed to the success of the holographic topometry project. In the first place, I wish to thank my advisor Prof. P. Hering for his encouraging support. He gave me academic guidance, supported the research in many ways and offered helpful suggestions to this work which would have never been completed without him. I am also grateful to Prof. G. Pretzler for his commitment and his comments which have led to essential parts of this thesis.
I wish to acknowledge the support of the research foundation `caesar` and its director Prof. K. H. Hoffmann. They provided the opportunity to do research in an unique, interdisciplinary and international environment. In this context, the help of my collegues from the project groups Lasertechnology and Holography was invaluable. Namely Dr. J. Bongartz, who pioneered on hologram tomography in his PhD thesis, and S. Frey who enthusiastically volunteered for many routine jobs while I was writing on my thesis are to mention, as well as A. Thelen, M. Ivanenkov, S. Afilal and M. Werner who were always willing to participate in fruitful discussions.
The project group on Rapid Prototyping of the research center caesar under the leadership of Dr. C. Tille and Dr. H. Seitz takes the credit for the facial models which strongly underlined our claim that hologram tomography actually works. They also provided the visualization of the bog body which was brought to Bonn owing to the commitment of Prof. Fansa from the Landesmuseum für Natur und Mensch in Oldenburg. Z. Krol from the Computer Aided Surgery group of the research centre caesar dedicated numerous hours of his time on automated registration of CT and hologram tomography data sets. Dr. J. Hertzberg and A. Nüchter from the Fraunhofer Institute on Autonomous Intelligent Systems are to mention for their help on the surface matching problem.
The clinical studies were conducted in cooperation with three institutions which provided important information on the application of hologram tomography in medicine: Prof. F. Zeilhofer and Dr. R. Sader from the Klinikum rechts der Isar (now at the Kantonsspital Basel) actively took part in the development of the holographic camera in many practical aspects. They also made possible the reenforcement of our team by Dr. K. Schwenzer who helped us with her experience on laser scanning systems. Prof. U. Fritzemeier from the Klinik für Kiefer- und Plastische Gesichtschirurgie of the University of Düsseldorf arranged the clinical evaluation of holography with a real patient and donated a dentist's chair for our set-up. He and, from the Poliklinik für für Mund-, Kiefer- und Gesichtschirurgie of the University of Cologne, Prof. J. E. Zöller and Dr. R. A. Mischkowski also acquired further volunteers for the testing of the holographic camera. It is to those volunteers who spent a lot of time and effort to travel to our laboratory that I wish to express my deepest gratitude.
Prof. B. Kessler from the FH Remagen has provided me with a teaching position during the course of this study and also arranged the visualization of CT/hologram tomography data. For that and for the experience gained in the classroom I thank her.
I would be remiss if I did not express my gratitude to my family and friends for their support during the time that I was engaged in this study. A special thank goes to P. Melin, who read this dissertation in draft form in its entirety and suggested many helpful revisions, and D. Conrad who carefully monitored the progress of the work. Last not least, I wish to thank my parents for their encouragement over many years.